Reviewed Preprint
v1 • July 21, 2025
Not revised

Reviewed Preprint
v2 • June 30, 2026
Revised by authors

Single neurons detect spatiotemporal activity transitions through STP and EI imbalance

Aditya Asopa, Upinder Singh Bhalla
National Centre for Biological Sciences, Tata Institute of Fundamental Research, Bangalore, India

For correspondence:
bhalla@ncbs.res.in

Competing interests: No competing interests declared

Funding: See page 45

Reviewing editor: Laura L Colgin, University of Texas at Austin, United States

eLife Assessment

This **useful** study examines excitation/inhibition (E/I) balance in the CA3-CA1 circuit of the hippocampus. Experimental and computational modeling results are presented. The computational modeling results were viewed as a novel advance supported by **solid** evidence, but **incomplete** evidence was provided to support the paper's main experimental claims due to deficiencies in the experimental methodology and concerns about the neurobiological relevance of the experimental observations.

https://doi.org/10.7554/eLife.107708.2.sa3

Abstract

Sensory input and internal context converge onto the hippocampus as spatio-temporal activity patterns. Transitions in these input patterns are frequently salient. We demonstrate that short-term potentiation (STP) mediates escape from EI balance to implement mismatch detection in spatiotemporally patterned activity sequences. We characterized STP in the mouse hippocampus CA3-CA1 network using optogenetic patterned stimuli in CA3 while recording from CA1 pyramidal neurons. STP modulates EI summation across patterns, first amplifying, then reducing responses. We parameterized a multiscale model of network projections onto hundreds of E and I boutons on a CA1 neuron, each including stochastic signaling to mediate STP. The model detected mismatches in trains of input patterns, which we experimentally confirmed. Mismatch selectivity depends on stimulus overlap, network weights, and connectivity. It is robust over a wide range of model parameters and assumptions about input spike timing jitter, postsynaptic spiking and stochasticity. Finally, we predict that optimal mismatch selectivity can be tuned over low to high gamma frequencies by modulating network parameters, and show that there is strong mismatch detection for gamma-frequency bursts between theta cycles, consistent with theta-tuned snapshots of novel input.

Introduction

The balance between excitatory and inhibitory drives (EI balance) in neural networks has a wide range of computational functions. These include increased storage capacity (Kanamaru et al. 2023), optimal coding (Denève and Machens 2016), fast temporal encoding and gating (Kremkow et al. 2010; van Vreeswijk and Sompolinsky 1996; Tim P Vogels and Abbott 2009), and higher dynamic range (Bhatia et al. 2019; Wehr and Zador 2003). EI balance applies over tight time scales and even combinations of inputs at a single neuron level, termed precise balance (Bhatia et al. 2019).

Homeostasis plays a crucial role in maintaining EI balance over time-scales ranging from minutes to days (Wen and Turrigiano 2024). Multiple forms of plasticity converge to achieve this balance, including Hebbian plasticity, disinhibition, and homeostatic plasticity (Nelson and Turrigiano 2008). At still shorter time-scales short-term plasticity (STP) mechanisms come into play. These

mediate a dual role: they contribute to rapid firing probability changes as part of ongoing computations (Anwar et al. 2017), but they must also maintain network stability even as they transmit bursts of activity.

There is an extensive body of work on fast EI dynamics. Pouille and Scanziani (F. Pouille and Scanziani 2001) used minimal stimuli to show that spikes could be elicited in the narrow interval between arrival of E and I inputs in the CA3->CA1 feedforward circuit. Feedforward inhibition expands dynamic range both in cortex (Frédéric Pouille et al. 2009) and in hippocampus (Bhatia et al. 2019). Tight EI balance has also been shown to track input signals and alter the amplitude of successive gamma cycles even in the absence of plasticity processes (Atallah and Scanziani 2009).

Active synapses undergo STP, during which neurotransmitter release varies upon receiving successive action potentials at the boutons (Fortune and Rose 2001; Regehr 2012; Tsodyks and Markram 1997; Zucker and Regehr 2002). STP emerges from the interaction and competition between pre-synaptic processes of vesicle depletion, calcium influx, calcium build-up, and neurotransmitter reuptake. Together, these processes create a temporal filter between activity in presynaptic and postsynaptic neurons and networks (Fortune and Rose 2001; Klyachko and Stevens 2006a; Galarreta and Hestrin 1998).

With the incorporation of STP, EI balance becomes even more dynamic. In cortical slices, E synapses depress more strongly than I during sustained stimulus trains, thus bounding postsynaptic activity (Galarreta and Hestrin 1998). In contrast, burst stimuli on Schaffer collaterals in rat hippocampal slices have been reported to lead to STD on inhibitory inputs and STP on excitatory ones, leading to a switch-like sharp increase in excitation during bursts (Klyachko and Stevens 2006a).

While these studies have focussed on the time-domain, network computation engages many neurons in patterned activity. Pattern memories are predicted to coexist with network-scale homeostasis through EI balance that combines plasticity with spatial patterns of activity (T. P. Vogels et al. 2011). Activity in the CA3 converges onto ensembles of cells representing distinct stimuli and contexts (Howard Eichenbaum et al. 1999; Yuste et al. 2024). In abstract terms, these ensembles form instantaneous patterns, or vectors of activity, which are decoded in a heteroassociative manner by the CA1 (Rolls and Kesner 2006).

A static view of such pattern decoding implies differential responses by individual CA1 neurons to different patterns, in other words, each pattern would result in a distinct firing rate. Given that activity is not static, it is more salient for neurons to detect transitions between input patterns. A classical expression of this computation is mismatch negativity (Butler 1968). While the mechanisms for this remain debated, at least one of them involves short-term synaptic adaptation (Garrido et al. 2009).

The current study integrates several research themes of EI balance, short-term plasticity, and network computation to systematically characterize and model the properties of a network with feedforward inhibition. We complete the experiment-model-prediction-testing loop and show that differential changes on E and I synapses may provide a mechanism for single neurons to extract salient features of spatiotemporal inputs through STP (Asopa and Bhalla 2023), while keeping mean activity steady.

We used in vitro whole cell patch clamp recordings and patterned optical stimulation of the CA3-CA1 in the mouse hippocampus, to probe how EI balance evolves over spatiotemporal input trains at CA3. We incorporated this STP data into mass-action stochastic models of presynaptic release for E and I synapses, and embedded a CA1 neuron receiving hundreds of such synapses into an abstract model of the hippocampal FFEI network. This model predicted that the postsynaptic CA1 neuron could detect pattern changes (mismatches), which we confirmed experimentally. We showed that mismatch detection works for pattern transitions and oddball patterns in spiking neurons and in the presence of gamma-frequency modulation of theta bursts. Finally, we show that this computation is robust and can be modulated over a wide range of network parameters.

Results

Optogenetic patterned stimulation in the CA3-CA1 network

We obtained whole-cell patch-clamp recordings from mouse CA1 pyramidal cells (PCs) in 350-micron mouse hippocampal slices, while stimulating channelrhodopsin (ChR2) expressing CA3 pyramidal cells using optical patterns generated by a digital micromirror device (Figure 1A-B, see Methods). Our bath solution had physiological levels of free ions including calcium (methods), and recordings were performed at 32-33 ℃ which has been shown in rats to yield similar short-term plasticity properties as at physiological temperatures (Klyachko and Stevens 2006b). A pattern consisted of either 1, 5, or 15 spots (spot size 13 x 7 µm, power 14.5 µW/spot) of blue light (470 nm). We illuminated the CA3 layer in a series of eight pulses at a fixed frequency of 20, 30, 40, and 50 Hz (Figure 1D). A probe pulse preceded this train by 300 ms to provide a reference baseline response. We measured the dynamics of E-I balance in a three-dimensional stimulus space consisting of CA3 activation size (number of spots), activation frequency (stimulation frequency), and short-term plasticity dependence (pulse number) in the train (Figure 1C).

To monitor the strength and consistency of the total resultant optogenetic activation of the CA3 layer, we used an extracellular field electrode in the CA3 stratum radiatum (Figure 1A, methods). The field response correlated well with optically-driven CA1 PC depolarization (Figure 1E-G), and scaled with the size of the pattern (Figure 1F). This was also consistent with the observation of a wide field of excitability around individual CA3 neurons (Bhatia et al. 2019) (Figure 1-figure supplement 1). From this we expect that there is some overlap in the sets of CA3 neurons activated by different patterns, and this overlap increases with more stimulus squares. Notably, the distribution of field amplitudes was very tight (Figure 1E), more so than the corresponding EPSPs (Figure 1H). Together with previous work using a similar optical stimulus system (Bhatia et al. 2019) we interpret this to say that the spiking responses from CA3 neurons to optical stimuli were consistent from trial to trial. The field response showed a slight decrease over the course of the pulse train of approximately 2% per pulse (regression fit slope=0.02, r^2=0.05). We attribute this to ChR2 desensitization. We observed a small amount of 'ringing' of the field response which we interpret as either CA3 spiking in a burst, or recurrent activation of the CA3 neurons (Figure 1-figure supplement 2). The ringing was down to ~5% by the third peak which occurred within 8 ms, supporting our treatment of the optical input as a single brief event, and setting a low bound to any contribution to patterns by recurrence.

As expected, patterns with more spots elicited larger responses in CA1 in current clamp (Figure 1 H-I) and voltage clamp (Figure 1 K-L). We separated E and I components by holding the cell at –70 mV (GABAR1 reversal potential) and 0 mV (gluR reversal potential) respectively. As reported previously (Bhatia et al. 2019), different activation patterns in CA3 produced proportional E and I post-synaptic currents in the recorded neuron (Figure 1K). However, over the pulse train, E and I underwent distinct STP profiles (Figure 1 M).

Thus our patterned optical stimulation provided multiple input combinations to probe the dynamics of monosynaptic excitation and disynaptic inhibition arriving at CA1 pyramidal cells.

EI balance evolves over the pulse train

We next asked how precise EI balance at the level of CA1 PCs dynamically evolves due to short-term plasticity processes across a range of frequencies and input strengths (Figure 2A). All the PSPs of an 8-pulse train were normalised to the probe pulse. The PSP varied significantly on all the tested three axes of parameters: pattern size ($p<0.001$), stimulus frequency ($p<0.001$), and pulse index ($p<0.001$) (ANOVA). Notably, the PSP of the first four pulses was significantly larger than that in the last four. We tested this by comparing the pulse responses divided between the two halves of the train against a shuffled pulse order ($p<0.001$, Wilcoxon rank test).

While PSPs are a measure of subthreshold EI balance dynamics, neuronal firing is the network readout of escape from EI balance. Spiking was rare for the stimulus strengths in our experiments. We observed spiking in only 7% of trials (n=154/2201). We measured the likelihood of escape from

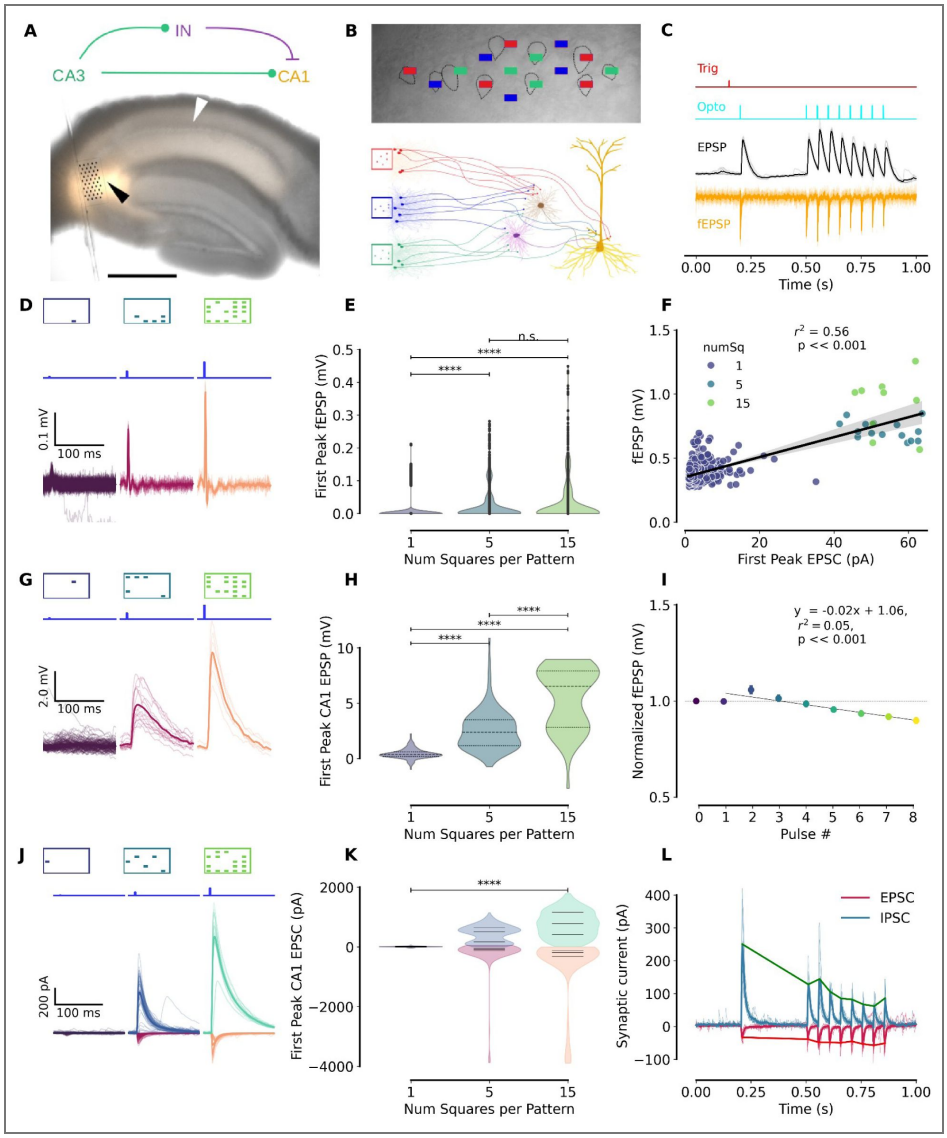

Figure 1. Experiment design and basic response properties.

A. (Top) Network schematic of hippocampal CA3-IN-CA1 network. (Bottom) A transverse hippocampal section showing channelrhodopsin expression in orange (tdTomato), with the stimulation grid drawn to scale overlaid on the CA3 network. An extracellular (field) electrode was used to record the total optogenetic excitation of the CA3 layer (black arrowhead), and CA1 recordings were made from individual pyramidal cells with a whole-cell patch clamp electrode (white arrowhead). (scale bar = 500µm) **B.** (Top) A DIC image of the CA3 cell layer with a few spots of a stimulation grid overlaid, drawn to scale. (Black dotted lines mark the outlines of a few CA3 cells). (Bottom) A schematic of the CA3-IN-CA1 layer showing the recruitment of CA3 pyramidal cells with three different patterns. The downstream CA1 pyramidal cell receives direct monosynaptic excitation from the activated population and disynaptic inhibition via a heterogeneous, shared population of CA1 interneurons. **C.** Burst recording protocol. Top (red): Trigger to start sequence. Cyan: Optical stimulus. Black: Postsynaptic potential of a patched CA1 cell (black). Orange: Simultaneously recorded field potential (orange). **D.** Extracellular recording of CA3 layer activation for 1,5,15 square patterns. **E.** CA3 field response to first pulse increases with number of squares per pattern (Kruskal-Wallis test). **F.** Correlation of optically stimulated current recorded from patched CA3 cells with the corresponding field response from CA3. **G.** Post synaptic potentials for first pulse (hence, no STP) recorded in a CA1 pyramidal cell for different pattern sizes. **H.** Distribution of PSPs across all recorded CA1 cells differs for number of squares (n=16, $p < 0.001$, Kruskal-Wallis test). **I.** Channelrhodopsin desensitization during burst is under 10% (linear regression fit with slope 2%, r^2=0.05, bars indicate 95% CI). **J.** Postsynaptic currents (PSC) recorded for first pulse from CA1 cells in voltage clamp show the proportional relationship between excitatory and inhibitory PSCs for each pattern size. **K.** Distribution of PSC amplitude differs between 1 and 15 square stimuli. **L.** A sample recording of excitatory (pink) and inhibitory (teal) currents recorded from a CA1 cell in the burst protocol described in panel C, for a 15 square pattern.

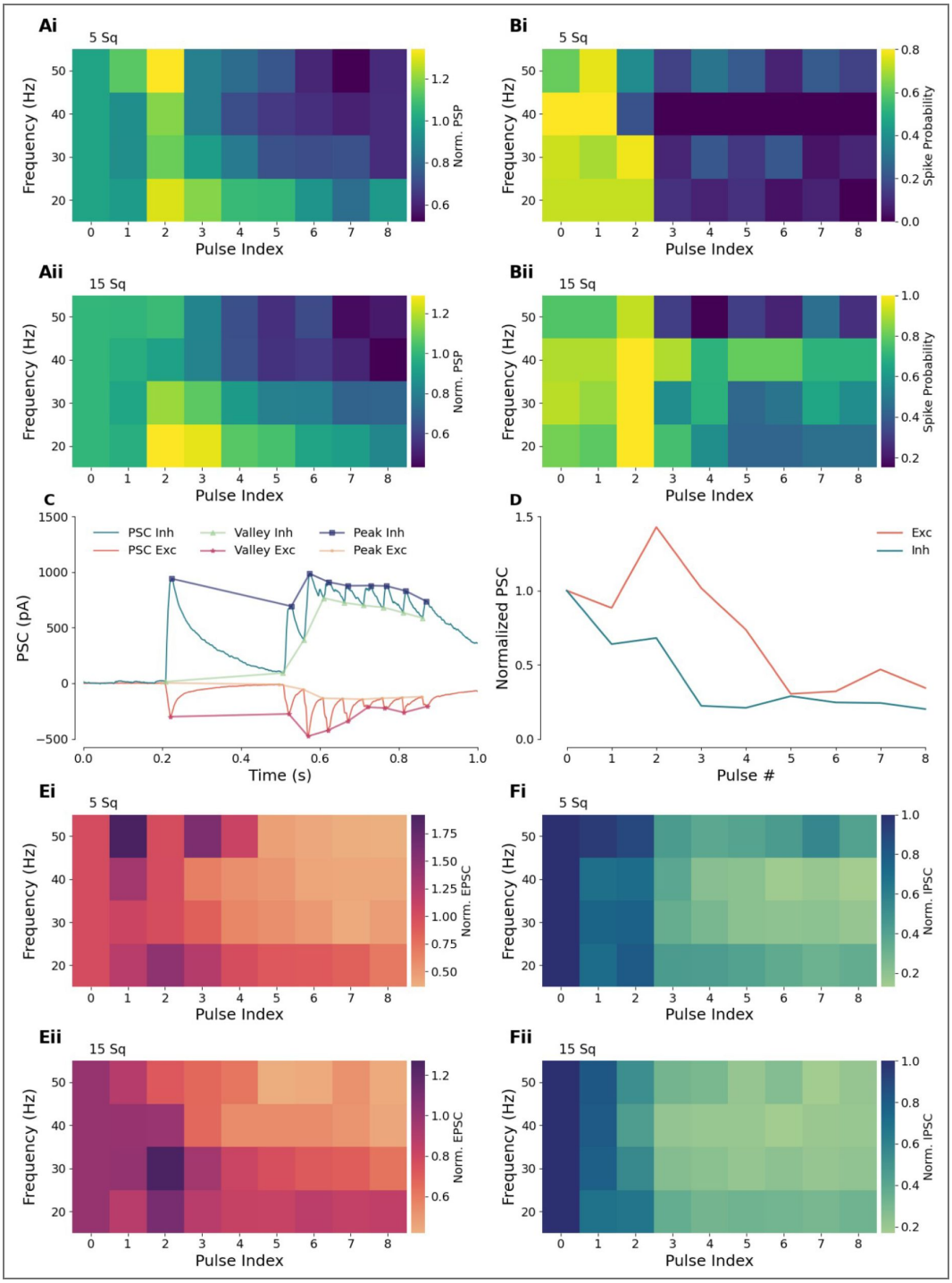

Figure 2. PSP, spiking, EPSC and IPSC dependence on stimulus frequency over a train of pulses.

(A) Trial-normalised excitatory postsynaptic potentials across stimulation frequency and pulse index in the train for 5 square (Ai) and 15 square (Aii) patterns across all recorded cells (n=16). B. Spike probability as a function of the stimulus frequency, pulse index and number of squares in the current clamp cells showing higher likelihood in the first half of the train for five squares (top) and 15 square patterns (bottom). C. Schematic for derivation of Post-synaptic responses. Kernel fits were obtained to valley to peak height for each response for both postsynaptic currents (voltage clamp, EPSC and IPSCs) and postsynaptic voltage (current clamp, not shown). D. Normalised EPSC and IPSC responses obtained for an example cell for a sample pattern showing consistent depression in inhibition and biphasic response in excitation. E, F. Both excitatory (Ei-Eii) and inhibitory (Fi-Fii) PSCs show short-term depression along the pulse train. Traces were normalised to a reference pulse 0, delivered 300ms before the burst.

EI balance by counting the fraction of total spiking trials that elicited for each combination of parameters (Figure 2B). Similar to the PSP response amplitudes, spike likelihood was higher in the first half of the pulse train ($p < 0.001$, ANOVA) Similarly, the spike likelihood depended significantly on both the pulse train frequency ($p<0.001$, ANOVA) and on the number of squares in the stimulus ($p << 0.001$, ANOVA).

We next measured E and I currents under voltage clamp across pattern size, pulse frequency, and pulse number. The EPSCs showed a trend of early potentiation followed by depression (Figure 2D, 2E), while the IPSCs underwent depression from the start (Figure 2 D, F). For the EPSCs, the 15-square trials had a higher reference pulse and higher stimulus overlap (discussed below), hence their normalised peak values were smaller (Figure 2E).

Thus EI balance over a burst briefly tilts in favour of E, after which both E and I undergo depression. This may result in a brief opportunity of escape from EI balance two or three pulses into a burst.

Multi-synapse summation and divisive normalization evolve over a pulse train

How might a neuron sum distinct input ensembles if they have distinct histories? We used the pattern-size axis of our stimulus protocol to probe history dependence of summation and subthreshold divisive normalization. We have previously shown that summed PSPs are not direct outcomes of EI ratios, because the delay between E and I onset is also a function of stimulus strength (Bhatia et al. 2019). We therefore measured each of these terms: postsynaptic potentials, postsynaptic excitatory and inhibitory currents, and their onset and peak delays (Figure 3 A-D) over the pulse series, and obtained gamma (γ) as a measure of linearity (Bhatia et al. 2019) (Figure 3 E-G). Gamma (γ) relates the observed response of a CA1 cell to the expected response obtained by summing the inputs linearly in the following manner:

$$\gamma = \frac{\text{expected} * \text{observed}}{\text{expected} - \text{observed}}$$

The smaller the gamma, the larger the deviation from the linear combination of inputs due to the divisive effects of inhibition.

By comparing observed vs. expected responses, we replicated earlier observations (Bhatia et al. 2019; Wehr and Zador 2003) showing sublinear summation, and obtained a median gamma of 7.16 (95% CI = 4.76 – 10.2) (Figure 3G). For comparison, we also performed a linear regression and obtained a median slope of 0.57 (95% CI = 0.45 – 0.72). We found that both gamma and slope values show a rise and then a fall in a history-dependent manner (Figure 3G). Thus the differential STP profiles for E and I synapses yield a history-dependence of pattern-specific summation, with greater linearity around pulse two or three in a train.

Presynaptic release models are bounded by observations from pulse-train sequences

Having characterised the dynamics of plasticity of excitatory and inhibitory synaptic currents over trains of pulses, we next used this data to develop models of presynaptic signalling. Datasets with similar pulse trains have been used to obtain phenomenological models (e.g.,(Barros-Zulaica et al. 2019)). Instead, we chose to build a chemical kinetics-based multi-step neurotransmitter vesicle release model similar to previously published models (Neher 2015; Schneggenburger et al. 1999) (Figure 4A). This incorporated both calcium buffering, which contributes to short-term potentiation, and depletion of docked vesicles, which underlies short-term depression. We implemented a ball-and-stick cellular model having AMPA and GABA synapses on the dendrite, with current or voltage-clamp recordings from the soma to compare to experiments. This chemical-electrical model was implemented in MOOSE (Ray and Bhalla 2008), and parameters were fit using a multi-objective optimization pipeline to match waveforms and dynamics over all frequencies and the entire pulse train. We independently fit presynaptic signaling models for E

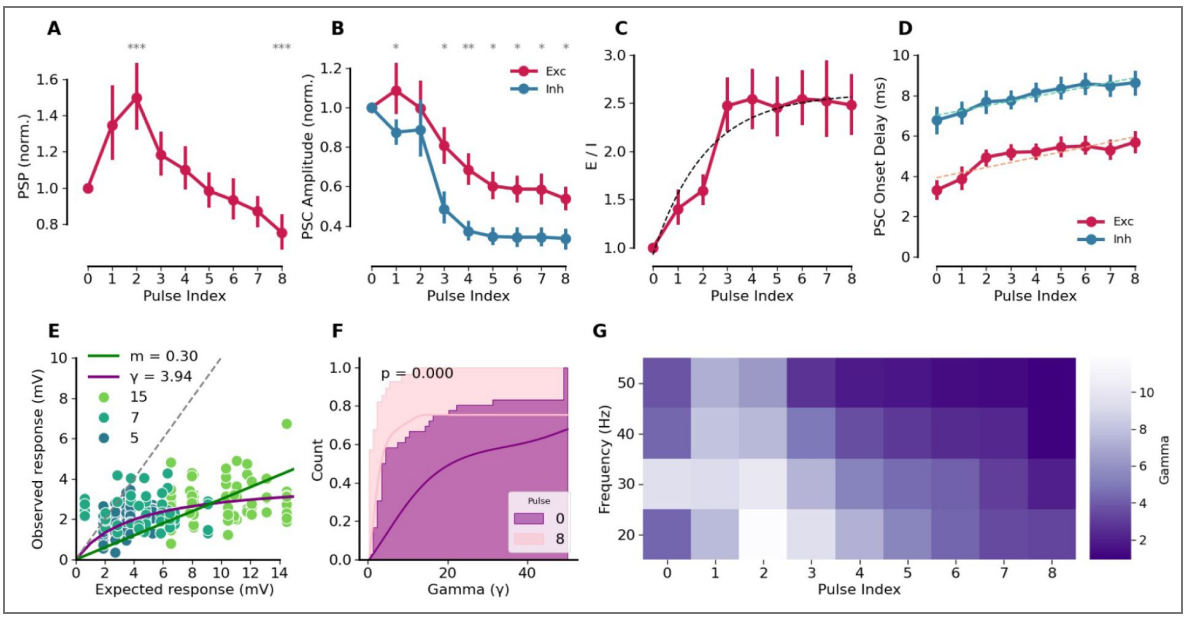

Figure 3. Excitatory-inhibitory balance evolves over the pulse sequence.

A. Postsynaptic potentials have a biphasic profile: they first rise, then fall in a pulse train. Pulse 2 > 1.0 at p=0.0003, Pulse 8 < 1.0 at p = 0.0003, Wilcoxon signed rank test. Stimulus was 20 Hz and response is normalized to pulse 0, for all patterns of size 5 and 15. B. Same stimulus as A, for voltage clamp. Postsynaptic excitatory (red) currents first rise slightly, then fall. Inhibitory (teal) currents fall throughout the train. All points except pulse 2 differ at $p < 0.05$, Holm-Bonferroni corrected Wilcoxon test. C. E-I ratio rises along the pulse train. Dashed line: saturating exponential fit, τ=2.115±1.0 pulses. D. The onset delay for both excitation and inhibition rises steadily over the pulse train. Dashed lines are linear regression fit with slope = 0.253ms/pulse for E and 0.232ms/pulse for I, slope difference not significant at p=0.123). E. Scaling of observed responses in CA1 for patterns of different sizes (5, 7, 15 spots) as compared to the expected responses obtained by the sum of constituent single-spot responses, shown for cell 3402, to illustrate the response normalisation. Solid purple curve is a fit to the equation with gamma = 3.94 = expected*observed/(expected – observed). Solid green line is best fit linear slope, m = 0.30. F. Gamma shows a leftward shift along the pulse train, here shown by comparing cumulative distribution of gamma for probe pulse vs pulse 8 of the train. (p<1e-3, Mann-Whitney test) G. Gamma depends both on pulse index and frequency. Gamma during the first four pulses is larger than in the later four (p<0.001, ANOVA).

and I to their respective voltage-clamp waveforms (Methods, Figure 4-figure supplement 1-3) (Nisha Ann Viswan et al. 2024). Each cell had somewhat distinct STP characteristics (Figure 4-figure supplement 4).

While the E fit applied directly to the CA3->CA1 pyramidal neuron glutamatergic synapse, the I fit was a composite of CA3->Interneuron and Interneuron->CA1 projections (Figure 4B, C). Based on the peak and onset times, we made the further simplifying assumption that only one interneuron class was involved, most likely PV interneurons. An example of CA3-triggered presynaptic signalling and postsynaptic currents is presented in Figure 4-figure supplement 5. Note that the synaptic chemistry was modelled using the Gillespie Stochastic Systems Algorithm (Gillespie 1977), hence the responses are noisy and synaptic release is probabilistic.

We used parameters for Cell 7492 for subsequent model-building (Figure 4-figure supplement 1).

Burst EPSP responses constrain single-cell parameters

We next embedded our presynaptic signalling models as synaptic boutons in a conductance-based electrophysiology model of a neuron, and used burst-EPSP responses to constrain its properties. 100 glu synapses were placed on dendritic spines, and 200 GABA synapses on the dendrite (Figure 4B). In the CA1 the E:I synapse ratio is between 12:1 to 25:1 (Bezaire and Soltesz 2013), but we implemented a subset of E synapses targeted by the CA3 pattern-responsive neurons in the interests of computational efficiency, as most of the E inputs would be silent.

We implemented an abstract hippocampal network to drive activity on the synapses. CA3 was implemented as a 16×16 array of integrate-and-fire neurons. Optical patterned input was mapped onto this array (Figure 4-figure supplement 6) and included charge buildup from successive light pulses as well as ChR2 desensitisation (methods, Figure 4-figure supplement 7). The interneuron layer was a 16×16 array of binary neurons. The CA3 array projected sparsely to the 100 glutamatergic synapses on the CA1 model and to the 256 interneurons. The interneuron array projected onto the 200 GABAergic synapses (Figure 4C). We used this full model, with optical stimulus, CA3, Interneurons, CA1 neuron, probabilistic connectivity, and presynaptic signaling chemistry, for all subsequent calculations in this study.

As a first-pass test of our model and comparison with experimental data, we modelled pulse train experiments performed using current clamp. We ran the simulations deterministically to correspond to the averaged experimental traces (Figure 5 A-D). There was no significant difference between experiment and simulation distributions for any of the frequencies (Figure 5 E, Table 1), nor for the slope over frequencies (Table 1). Since simulations permit access to internal state variables not available to the experiments, we also looked at how E and I currents and conductances balanced out during the pulse train (Figure 5F-O). Notably, the simulations predict that the E current builds up, especially on the second pulse of the train. This corresponds well with the observations in Figure 5 A-D and in Figures 2 and 3.

Overall, the synapse and single neuron components of our model worked well together to replicate burst inputs in current clamp.

Poisson train stimuli constrain network parameters

Following the synapse and cell-level analysis of signal summation and short-term plasticity in the CA3-CA1 system, we next tuned our model to network-level readouts. Here we explicitly included an analysis of scatter in the experimental data. We modeled the origin of this scatter as stochastic synaptic chemical kinetics and transmitter release (methods). To simulate recording noise we overlaid Gaussian noise with an amplitude of 0.5 mV and upper cutoff of 200Hz on the simulated EPSP traces. We delivered a 'frozen' Poisson-train sequence to experiment and model, to test the capacity of the model to replicate data and to further constrain network-level parameters using a panel of statistics of the responses (Table 1). Figure 6 A and B show example EPSP traces for a single trial of an experiment and simulation, respectively. We used simple parameter sweep runs to tune the model network parameters.

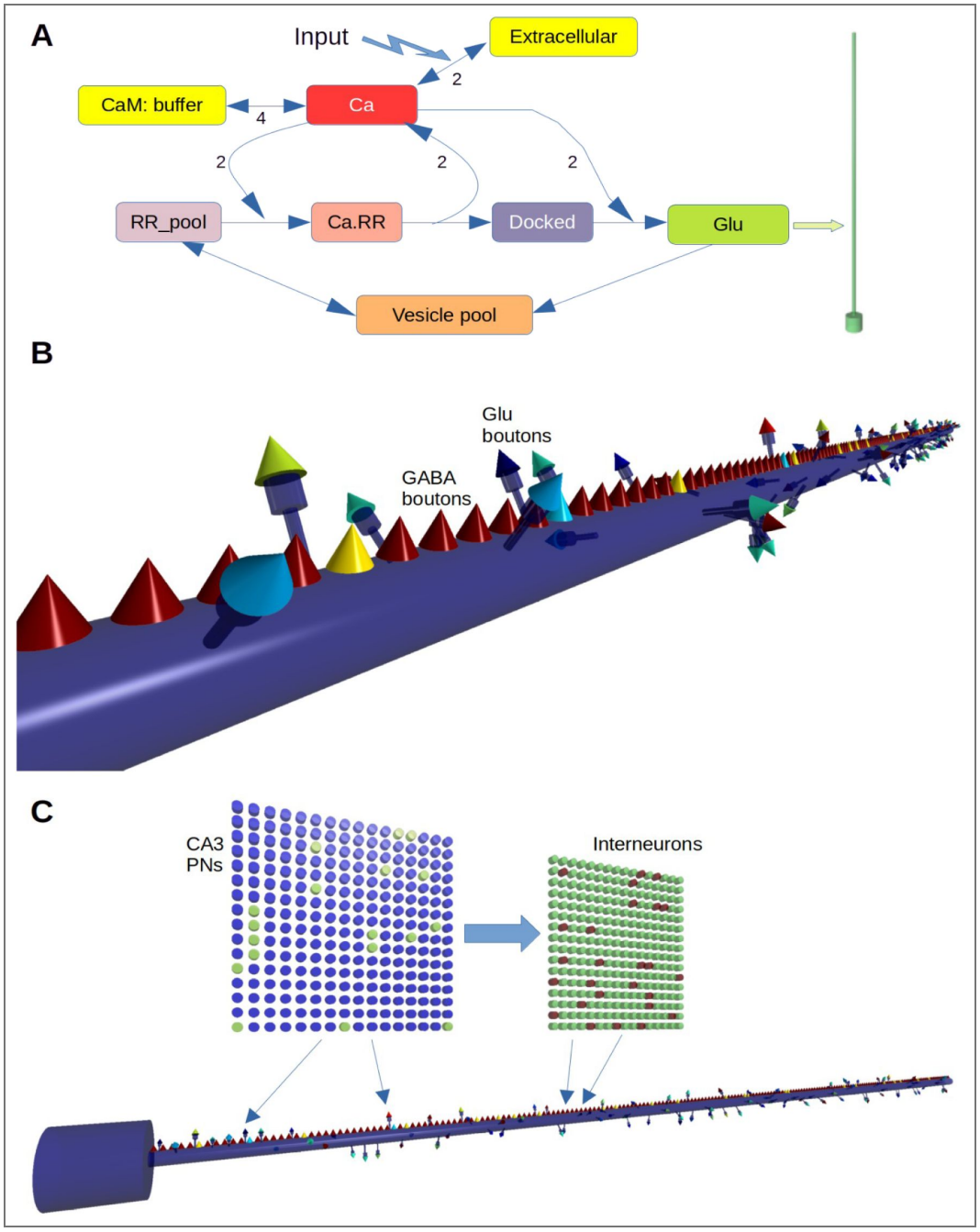

Figure 4. **Multiscale model.**

A: Model of reaction system in each bouton. Synaptic input triggers entry of extracellular Ca2+ into the bouton, and a pump removes the Ca. CaM buffers the Ca2+. Ca binds/unbinds from successive stages of the readily releasable (RR) pool of vesicles till they are docked, at which point the final Ca-binding step causes synaptic release. The released neurotransmitter (Glu for excitatory synapses, GABA for inhibitory) opens a ligand-gated receptor channel on the postsynaptic CA1 neuron, which is held voltage-clamped.(green arrow). The reaction scheme was identical for Glutamatergic and GABAergic synapses, but the rates were different to fit the respective voltage-clamp recordings. B: Close-up of dendrite of CA1 pyramidal neuron model. The cell has a compartment for soma, a 200-micron compartment for the dendrite, and 100 spines. Each spine is modelled as a head compartment, a neck compartment, and a presynaptic glutamatergic bouton. There are 200 GABAergic presynaptic boutons positioned directly on the dendrite. C: Network model. The CA3 has 16×16 neurons, projecting randomly to 16×16 interneurons. CA3 also projects directly to the Glu synapses on the spines. The interneurons project to GABA synapses.

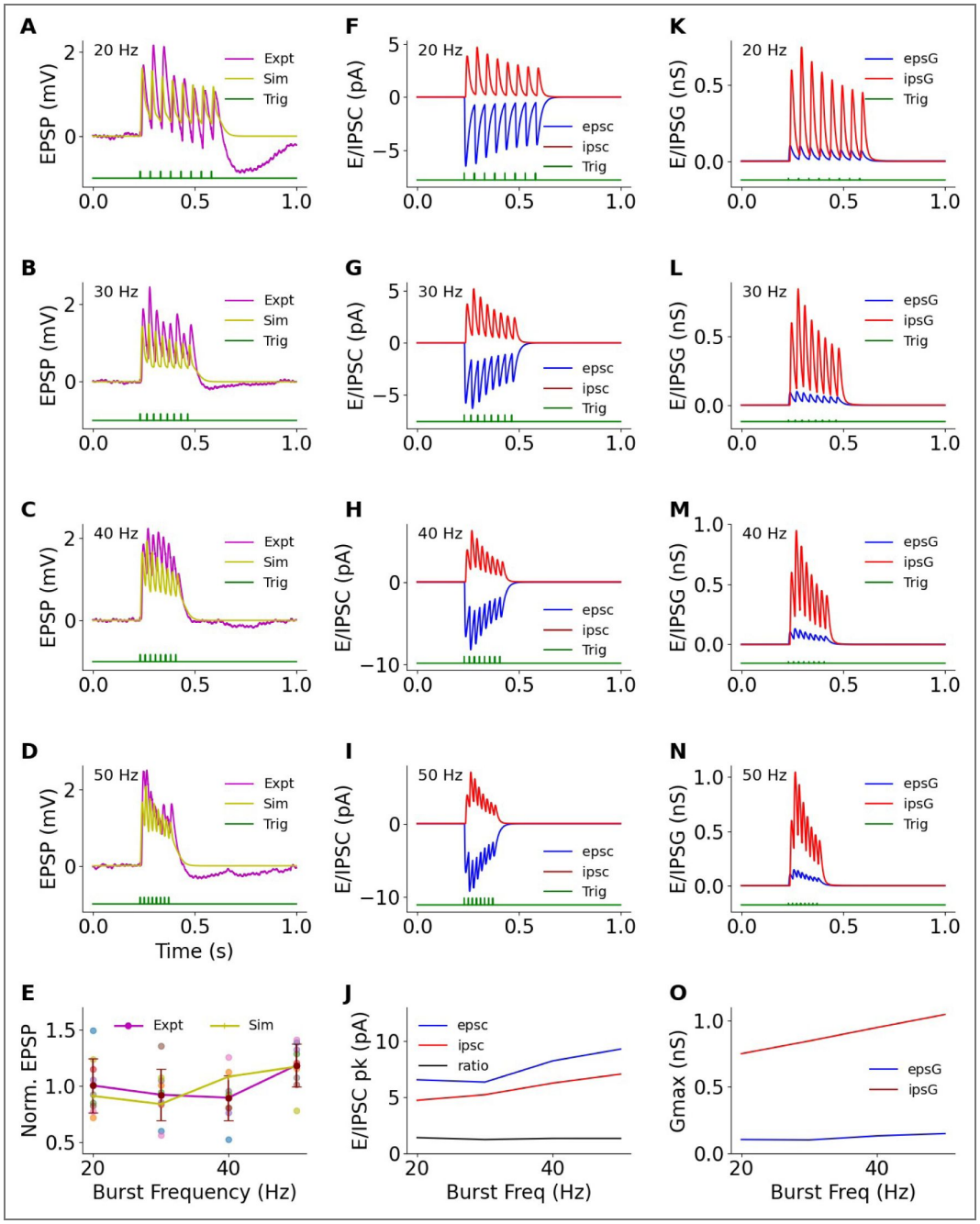

Figure 5. Temporal summation and EI balance in burst stimuli.

A-D: EPSP measured at soma for representative cell 3402 (maroon) and simulation (yellow) for each frequency. E: Distribution and mean of EPSP over all recorded cells for each frequency for the experiment (maroon) and for a simulated neuron (yellow). There is no significant dependence of EPSP on frequency for the recordings (Linear regression, slope=0.005, p=0.168) or for simulations (Linear regression, slope = 0.01, p=0.134). Simulated slope lies within the 95% range of the confidence interval [-0.002, 0.0126] of the slope for experimental data (Bootstrap, 10000 resamples, Table 1). The simulated peak EPSPs lie within the range of experimental cells at each of the four frequencies (Table 1) F-I: Simulated excitatory and inhibitory currents for each frequency. Note that the currents are measured close to resting potential, so the driving force (E_{GABA} − Vm) is small compared to the voltage-clamp experiments in Figure 1K, where Vm was held at 0 mV. J: EI balance (ratio, black line) is maintained for simulated excitatory and inhibitory current peaks for all frequencies. K-N: Simulated excitatory and inhibitory conductances for each frequency. O: Simulated excitatory and inhibitory conductance peaks. Note that simulated synaptic conductances are reduced by ~50x from typical cellular values to match the much smaller cell geometry and higher input impedance.

	Figure	Data description	Test	statistic	Comparison	Notes
1	5E	Experiment: 9 cells, 4 frequencies. Simulation: 1 run, 4 frequencies	Wilcoxon signed-rank	20Hz: W=13 30Hz: W=18 40Hz: W=6 50Hz: W=14	p-value 0.301 0.652 0.055 0.359	No difference at 95%
2	5E	Same	Is simulation in range of experiment [Experiment min, experiment max, **simulation**]	20 Hz 30 Hz 40 Hz 50 Hz	[0.716, 1.492, **0.884**] [0.563, 1.355, **0.962**] [0.520, 1.253, **1.043**] [0.782, 1.413, **1.111**]	Sim within range at all frequencies
3	5E	Same	Regression fit for slope. Bootstrap for slope at 95% confidence interval to compare simulated vs. experimental	Confidence Interval CI: [-0.002, 0.0126] Sim slope = 0.0076	95% confidence interval	Sim is within CI.
4	6C	Power spectral density of EPSP due to Poisson train of optical stimuli	Cosine distance between experiment mean and sample: Is simulation within experimental range.	[min, max, **sim**] 5 Sq trace: 15 Sq trace	[0.933, 0.980, **0.962**] [0.926, 0.990, **0.957**]	Sim within range.
5	6D	Probability of spiking following stimulus after initial settling time of 2s	Probability in %	[min, max, **sim**] 5 Sq trace 15 Sq trace	[28.9, 64.5, **58.7**] [61.9, 90.2, **86.9**]	Sim within range Sim within range
6	6E	EPSP vs time: Slope of initial decline for t < 1.8s	Linear regression fit slope range for cells, compared with simulation	[min, max, **sim**] 5 Sq trace 15 Sq trace	[-1.78, 0.564 **-0.033**] -3.07, 0.329, **-0.124**]	Sim within range Sim within range
7	6E	Mean amplitude	Mean amplitude range for cells,	[min, max,**Sim**] 5 Sq trace	[0.395,	Sim within

Table 1. Summary of statistical comparisons between simulation and experiment for figures 5 and 6.

For Figure 5 panel E, the simulation EPSP peaks do not differ significantly from experiment either for the means for each individual frequency, nor does the slope across frequencies differ from experiment. For Figure 6 we obtained the specified statistics for each panel, and asked if the simulation was within the range of values seen for individual cells. In all cases it was within the range, except for panel 6F for the 5 Square stimulus.

			compared with simulation	15 Sq trace	1.15, **0.814**] [0.994, 2.88, **1.91**]	range Sim within range
8	6F	Decay time-course of EPSP vs ISI	Time constant tau computed by fitting to data points	[min, max,**sim**] 5 Sq trace 15 Sq trace	[0.34, 17.6, **34.6**] [8, 933, **49.9**]	Sim **NOT** within range Sim within range
9	6G	Fit EPSP amplitude distribution to lognormal	Lognormal mu (log-mean)	[min, max, **sim**] 5 Sq trace 15 Sq trace	[-1.09, -0.0038, **-0.536**] [-0.139, 0.847, **0.392**]	Sim within range Sim within range
10	6G	Fit EPSP amplitude distribution to lognormal	Lognormal sigma (log-std-dev)	[min, max, **sim**] 5 Sq trace 15 Sq trace	[1.18, 1.39, **1.23**] [0.881, 1.18, **0.99**]	Sim within range Sim within range

Table 1. (continued)

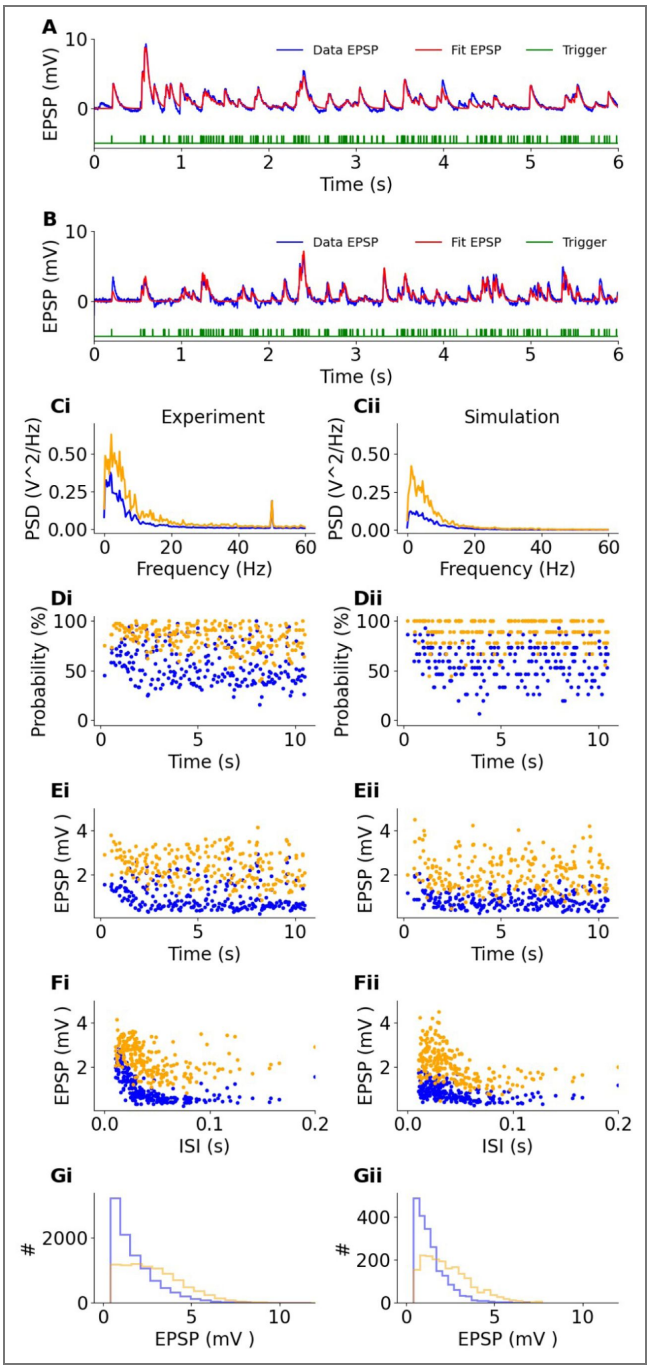

Figure 6. Experimental and simulated responses to Poisson spike train input, all patterns.

A: Sample experimental EPSP train aligned with light trigger pulses (green). Blue trace is recorded data; red trace is the fit used to compute peaks and subsequent statistics. B: Same for simulated data. C-G: Comparisons for readouts of experiment (left column) and simulated (right column) data. Blue traces/markers: 5-square stimulation, orange traces/markers: 15-square stimulation. Outcomes are detailed in Table 1. In all cases except panel F-5Sq, the simulated response lies within the range of individual cell responses. C: Power spectral density of EPSP response over the entire dataset. Note 50Hz peak due to line noise in experimental dataset, despite this the cosine distance between experimental mean and simulated response was within the range of individual cell cosine distances to mean. D: probability of trigger to generate a peak in the EPSP trace. E: Scatter plot of EPSP peaks as a function of time over the Poisson train. Note the initial decline due to STP and ChR2 desensitisation. Comparisons were made both for this initial decline (up to 1.8 s) and for the subsequent steady-state EPSP peak distribution. F: Scatter plot of EPSP peaks vs. Inter-spike-interval. The experimental data show an elevation of EPSP at short ISI. We fit this using a simple exponential decay function y=y0.exp(-t/tau)+y1. G: Distribution of EPSP peak amplitudes.

We first estimated the power spectral density of the EPSP waveforms (Figure 6 C, Table 1). We obtained the experimental mean spectral density as a reference, and compared individual cells and simulation to this mean using the cosine distance. The simulation fell within the experimental range of cell cosine distances.

Then we compared the probability that each optical stimulus would elicit an EPSP (Figure 6 D). As expected, 15-square patterns (yellow dots) frequently gave an EPSP (77.5±11.7%), while 5-square patterns failed about half the time (51.4±16%). The simulated runs matched this (Table 1). The probability of failure reduced with increasing volume of the simulated presynaptic boutons, because larger volumes experienced smaller chemical noise (stochasticity) in synaptic release (Figure 6-figure supplement 1). We note that for the purposes of eliciting a postsynaptic response, any unreliability in optical stimulus-triggered firing of the CA3 neuron folds into the probability term for stochastic synaptic release. By matching this metric to experiment, we fine-tuned the scaling term for the presynaptic boutons to 0.2, which after the randomization of synaptic volumes during setup gave a volume of 0.0205±0.0008 femtolitres.

In Figure 6 E we compare scatter plots of EPSP amplitudes over time. Note that the initial high EPSP responses declined over the first two seconds. Hence we made two comparisons between model and experiment: First, the slope of the initial decline (t<1.8s) and then the steady-state distribution (t>2s). The simulations were within the range of experimental cells for both these metrics (Table 1). We asked if ChR2 desensitisation of the stimulus might account for the initial decline. We found that the field response does indeed show a decline over multiple pulses (Figure 6-figure supplement 2). We also checked for short-term depression as a mechanism for this decline by comparing the reference and the no-STP model (Figure 6-figure supplement 3A). Without STP there was no decline, but the absolute EPSPs were considerably elevated.

We then plotted each EPSP against the inter-stimulus interval (ISI) preceding it (Figure 6 F). We observed that the EPSP was high for very short intervals and then declined to a lower steady value, both in experiments and simulations. We initially assumed this was due to increased STF for closely succeeding input pulses. Unexpectedly, the no-STP model also showed the same profile of high EPSP at short ISIs (Figure 6-figure supplement 2B iii). Removal of NMDA receptors in the model also did not change the EPSP-vs-ISI profile (Figure 6-figure supplement 3B iv). Thus, we conclude that the high EPSP was simply due to charge accumulation during rapid synaptic input. For this comparison the simulation was within the experimental range for 15-square stimuli, but not for 5-square stimuli (Table 1).

We finally compared the distributions of EPSP amplitudes (Figure 6 G). We used a log-normal distribution, and thus obtained the log-mean and log-standard deviation terms for each histogram, for each of 5– and 15-square stimuli. In all four comparisons the simulation was within the experimental range (Table 1).

Overall, we were able to quantitatively replicate almost all features of the experimental dataset in our multiscale model incorporating presynaptic signalling, postsynaptic electrophysiology, and abstracted network connectivity and responses. Between the datasets in Figure 4-figure supplements 1 to 3, Figure 5, and Figure 6, we were able to substantially constrain the parameters in our model, from chemical to cellular physiology to network. Network connectivity parameters are presented in Table 2. All subsequent simulations used this ‘tuned’ model except for spiking models, which had 2x greater synaptic weights.

STP and sparse coding yield pattern mismatch detection

We next used our model to ask how an important neural computation, that of mismatch detection between successive pulses of network activity, could emerge from single-cell computation involving EI balance and STP. The existing heuristic argument based on synaptic adaptation(May and Tiitinen 2010) is as follows: Consider two patterns of activity, A and B, comprising different ensembles of CA3 pyramidal cells. Let these overlap to a small extent, say A∩B < 20%. Since the CA3 projects directly to CA1 spines, the overlap onto excitatory synapses will also be around A∩B. Now, we consider STP. Repeated inputs of pattern A result in the initial strengthening of excitatory

Parameter	Description	Default value
wtGlu	Mean conductance (nS) of population of 100 AMPA synapses. Defined in model as relative value with reference = 5. Open conductance scales this by the release amount of Glu transmitter.	0.474 ± 0.013 nS
wtGABA	Weight (conductance) of each of 200 GABAergic synapses. Relative reference value in model = 10. Open conductance scales this by the release amount of GABA transmitter.	12.57 nS
pCA3_CA1	CA3 to CA1 connection probability, i.e., probability that a given CA3 neuron synapses onto a CA1 neuron	0.02
pCA3_Inter	CA3 to Interneuron connection probability	0.01
pInter_CA1	Interneuron to CA1 connection probability	0.01
zeroIndices	Number of silent CA3 neurons, 'masking' optical input.	192
ChR2_ampl	Scaling factor for optical stimulus to depolarize CA3 neuron. (Not varied)	0.1

Table 2. **Network parameters and their definitions.**

inputs, then depression. At the transition from pattern A to B, most of the excitatory inputs have not been stimulated before, so the fresh synapses are stronger. This gives a larger excitatory drive. From this heuristic argument, we predict two things: First, at transitions between patterns (mismatches), we expect a transient elevated response in the postsynaptic cell. Second, the size of the transient should be larger if the input patterns are sparse in E, because this lessens the overlap between them. We note that our model also includes plasticity in inhibitory synapses, which has implications for transient changes in EI balance as analyzed below.

To test the prediction of mismatch detection in the model, we simulated a sequence of patterns of the form "AAAAAAAABBBBBBBBCCCCCCCCDDDDDDDD", that is, eight repeats of each of four spatial patterns shaped like the letters A to D (Figure 4-figure supplement 6). As expected from the above argument, EPSCs experienced an elevated response just after the pattern change (mismatch detection), and this was dependent on the repeat frequency of the patterns (Figure 7A). IPSCs, on the other hand, started with a large response and then underwent a nearly smooth decline over the repeated pulses, with very little alteration at the pattern changes (Figure 7A). This smooth decline arises from two factors: The observed short-term depression of the inhibitory inputs (Figure 3B), and the high degree of overlap on inhibitory inputs because of the two-stage inhibitory feedforward connections (Figure 7-figure supplement 1). Put together, these E and I components give both strong mismatch detection (due to sparse E) and delayed EI balance due to compensation for the slow STD of E synapses by corresponding STD of I synapses. In current-clamp mode, this gives us consistent mismatch detection (Figure 7B). When all synaptic and channel kinetics were scaled to physiological temperature (37°C) the mismatch transients were similar to the reference simulations (Figure 7C).

Based on these predictions, we asked if we could experimentally detect pattern transitions in our slice preparation. Rather than projecting letter-shaped pixel patterns in the optical array (which would have required high pixel coverage), we generated randomized non-overlapping sets of 5 distinct patterns of 5 squares, and 3 of 15 squares (Figure 1, Methods). We delivered the same eight repeats each of four of these patterns at repeat rates of 8, 20 and 50 Hz to span a range from theta to gamma frequencies (Figure 7 D). We used the Wilcoxon test to compare experimental EPSPs for 3 pulses immediately before and after pattern transitions. We observed that mismatch detection did indeed occur, but it was selective. In the example cell we observe a single significant mismatch response in Figure 7D at 50 Hz for the transition from pattern 3 to pattern 4. Over the population of cells we found that mismatch detection was dependent on a) frequency, b) specific pattern transitions, and c) number of illuminated squares. Mismatch detection occurred most often for 15 square patterns at 50 Hz (Figure 7Ei).

We then asked if our model with full stochastic synaptic kinetics could replicate these results. We ran our model over a population of 6 simulated cells in which the specific connectivity differed due to different random number seeds, and furthermore the stochastic chemistry also used different seeds (Methods). There was considerable variability between simulations, but overall we obtained a higher likelihood of mismatch responses than experiment for 5 squares, and lower for 15 squares. (Figure 7Eii). The percentage of significant mismatch responses both for 5 and 15 squares became closer to experiment when we incorporated 6ms jitter in the timings of spikes from the CA3 layer, and added 500Hz bandpass filtered 2mV Gaussian noise (Figure 7Eiii). As discussed later, further network details such as cell-to-cell heterogeneity and different classes of inhibitory interneurons may be needed to account for the remaining differences between model and experiment.

Thus, at this stage we had predicted STP-dependent single-neuron detection of mismatches in sequences of inputs, confirmed it experimentally, and then shown that our model performed mismatch detection in the presence of stochastic synapses, stimulus timing jitter, and recording noise.

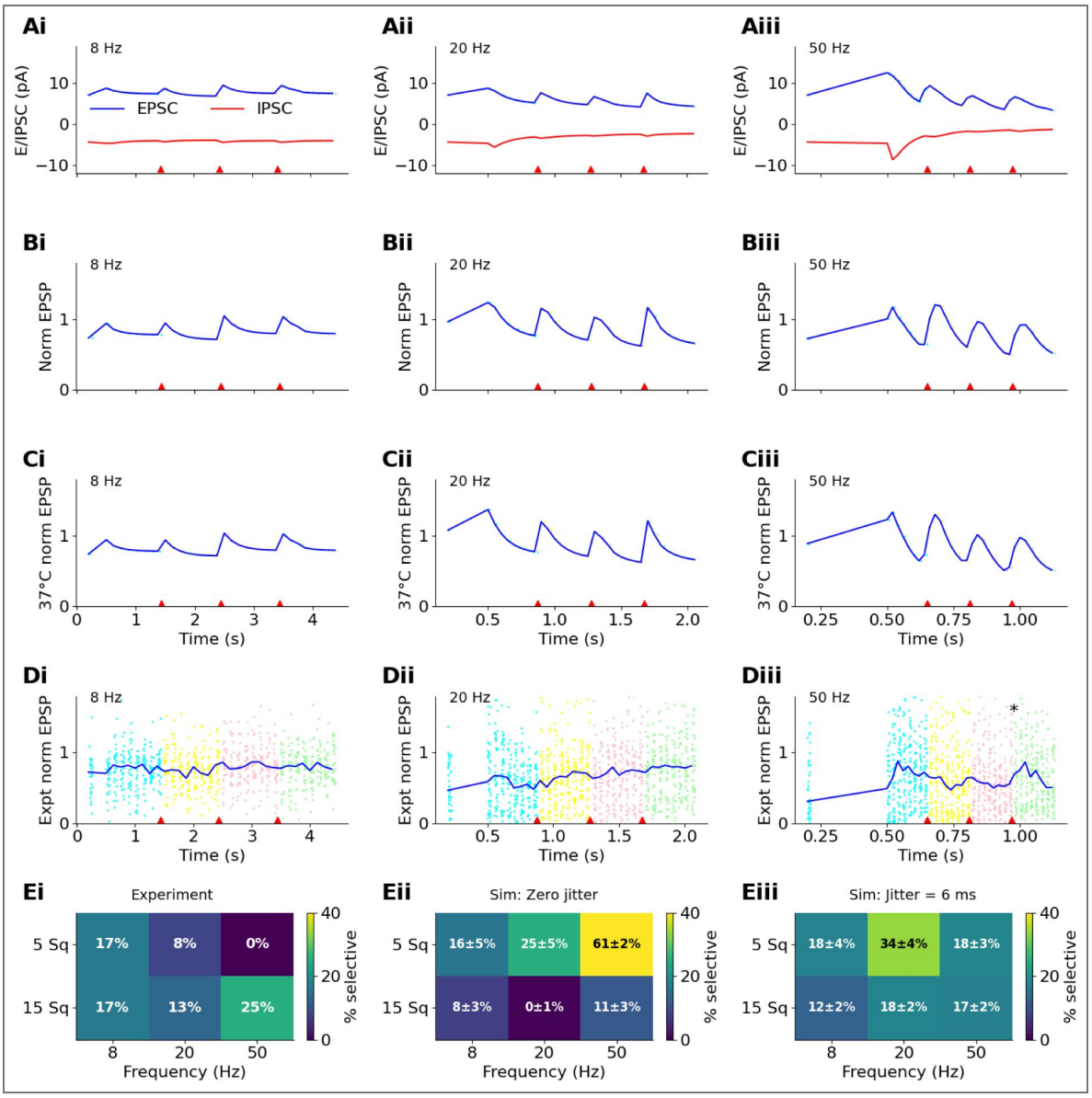

Figure 7. Mismatch detection in simulations and experiment.

In all cases, the stimulus was 8 repeats each of 4 patterns, at the specified frequency. In panels B,C,D the red triangles indicate time of pattern change. A: Deterministic simulations. Excitatory and inhibitory currents contribute different terms to the mismatch signal. Excitatory currents detect the transition, whereas inhibitory currents undergo synaptic depression to balance depression in excitatory currents. B: Same simulations. At each mismatch there is an elevation of EPSP, shown normalized around the mean signal. C: Same as B except using the model configured for 37° C. D: Experimental data. Colored scatter points indicate individual trials, the different colors represent different patterns. The solid blue line is the mean. A significant (p=0.013, Wilcoxon signed-rank left-tailed test) mismatch signal is seen for the third transition on Diii. E: Summary heatmaps showing percent of significant transitions ($p < 0.05$, Wilcoxon signed-rank left-tailed test) for experiments (Ei) and simulations (Eii and Eiii). In the simulations we assume 2mV of 500Hz lowpass filtered noise. Eii: no jitter in stimulus timing. Eiii: 6ms half-Gaussian distributed jitter. The introduction of jitter substantially changes the probability of selective transitions, however the simulated probabilities remain somewhat different from experiment.

Mismatch detection is effective in spiking neurons

Our previous analysis of mismatch detection was in the sub-threshold regime. We next introduced spiking, as a closer approach to relevant network responses. To do this we increased the conductance of voltage-dependent sodium and potassium delayed rectifier channels in the soma of the CA1 neuronal model from placeholder values to firing values (125 nS and 141 nS) and doubled the synaptic weights of AMPAR and GABAR inputs to 10 and 20 respectively. No other changes were made to the model. We obtained spiking responses for 50 stochastic runs with patterned input at 50 Hz (Figure 8 A,B), and averaged the resulting firing rates with a 10ms window, as a proxy for population activity (Figure 8 C-K). As expected, the resultant spiking was locked to the period of the simulated patterned input series.

The reference spiking model replicated both mismatch detection and pattern selectivity, with significant elevation of spiking at each of the transitions (red triangles Figure 8C, p = 0.0036, 0.0040, and 2.1e-5 for the respective transitions, Binomial test). The spiking model supported the heuristic prediction that networks with high overlap of excitatory inputs to CA1 would be less sensitive to mismatches (Figure 8D, E). None of the transitions in Figure 8D (dense stimuli, 34% overlap) were significant, but two transitions in Figure 8E were significant (sparse stimuli with 2.5% overlap, p = 1.53e-5 and 6.1e-5). We next explored a range of stimulus conditions for functional implications. First, we considered the frequently used behavioural paradigm of 'oddball' detection, which produces a rapid ~100-250ms evoked potential in several modalities (Butler 1968; Garrido et al. 2009). We delivered a constant, repeating pattern interspersed every 8 stimuli with the oddball (deviant) stimulus. We obtained a selective response to the third oddball presentation (Figure 8 F). The repeated stimuli resulted in a strong depression of firing rates, hence for this and the next stimulus, we doubled the number of trials to 100 in order to increase the statistical strength of the binomial test.

Gap stimuli, where the deviant stimulus is an absence of stimulus, are also known to be strong behavioural triggers for oddball responses (Garrido et al. 2009). We implemented this as above, simply replacing the oddball stimuli with an absent stimulus. In our model the gap stimuli did not give any significant responses (Figure 8 G). In the discussion we consider how gap and other complex deviant stimuli may be detected without high-level network mechanisms.

We then asked how STP in E and I contribute to mismatch detection. Selectivity was completely lost when we removed STP from glutamatergic synapses (Figure 8 H). In the absence of GABAR STD, there was a steep decline of spiking activity over the time course of the trial (Kendall's tau=-0.456, p=0.0003, Figure 8 I), consistent with the requirement for EI balance over multiple pulses in order to retain excitability. Selectivity, albeit with very few spikes, was still present for the second transition (Binomial test, p=0.004, Figure 8 I).

We next ran two controls to confirm the role of transitions in eliciting mismatch responses. In the first control we delivered the same spatial pattern for all 32 pulses (Figure 8J). As expected, this led to a rapid decline in spiking (Kendall's tau=-0.53, p=3.6e-5). Next, we randomly selected one pattern among our set of five for each pulse (Figure 8 K). Surprisingly, this also gave a decline in spiking, though it was not as steep as the uniform pattern (Kendall's tau=-0.314, p=0.008). Upon further analysis, it turned out that random sequences had sufficient overlap to trigger a subset of the same synapses (Figure 7-figure supplement 1). The net effect was that excitatory synapses were stimulated at ~21 Hz for random patterns, as compared to the 50 Hz for uniform patterns. This led to slower synaptic depression.

We next asked if there was a frequency-dependence of mismatch detection in the spiking model (Methods). Briefly, we ran a frequency sweep from 8 to 150 Hz, with 10 simulated cells with distinct random seeds for connectivity. We found that there was a broad peak of selectivity in the mid-gamma range from 50 to 100 Hz (Figure 8 L).

To place the gamma-frequency tuning in a more physiological stimulus context, we considered the well-known phenomenon of gamma bursts modulated by a theta background(Lisman and Jensen 2013). We modeled theta-modulated gamma bursts, where each theta cycle had five pulses of input at 100 Hz, with the start of each burst separated by 130 ms to give a 7.69 Hz theta rhythm

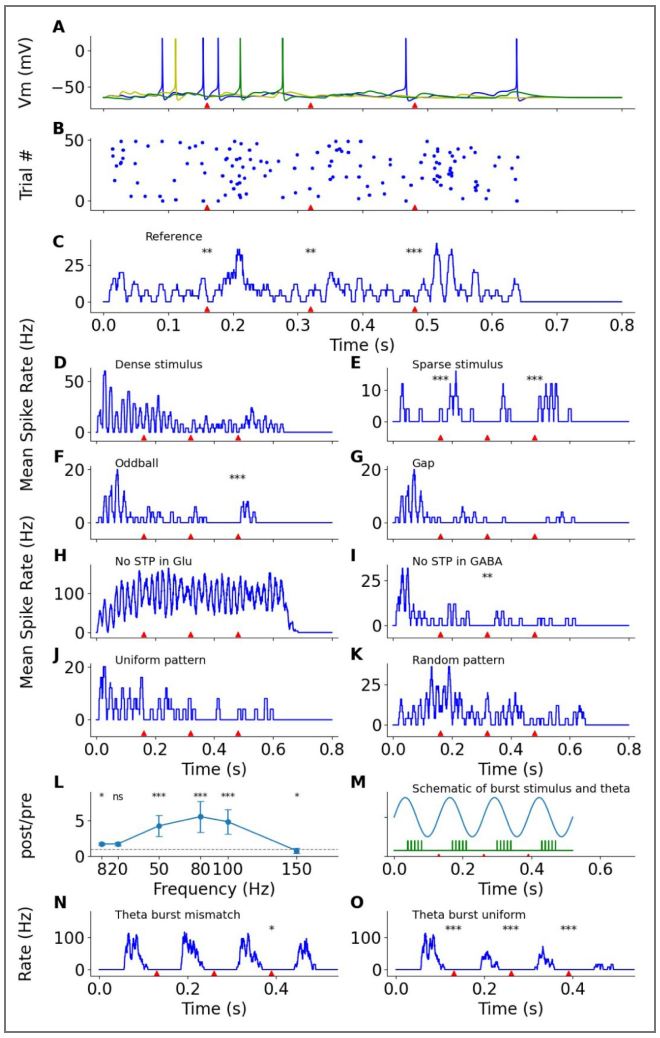

Figure 8. Spiking responses are selective for mismatch in patterned sequences.

All runs were performed using a spiking neuron model with stochastic synaptic chemical kinetics and each run consisted of 50 trials. Red triangles indicate transition times between patterns. Asterisks over the red triangles indicate significance of transitions. For panels A to E and H to K, the stimulus consists of eight repeats of each four patterns as in AAAAAAAABBBBBBBBCCCCCCCCDDDDDDDD. Traces C-K and N-O are spike rates with a moving window of 10 ms and 5 ms respectively. In C-K, Mismatch statistics use the binomial test to compare the counts of the three pulses immediately before vs. the three immediately after a transition. A: Spiking responses on three illustrative trials. B. Raster plot of spiking for reference stimulus. C: Reference model exhibits mismatch responses for the first two pattern transitions (p=0.002, 0.032, 0.434). D: Dense stimuli (12.5% spots nulled) do not give any mismatch signals. E: Sparse patterns (94% of spots nulled) elicit a mismatch response in two transitions (p=1.5e-5, 6.1e-5). F: Oddball response. There was a strong and pattern selective mismatch response (p=9.5e-7) to the third oddball (deviant) stimulus. Oddballs were presented every 8th pulse, against a uniform background pattern: AAAAAAAABAAAAAAACAAAAAAADAAAAAAA. G: Gap stimulus. Similar to oddballs, gaps were presented every 8th pulse, but instead of a deviant stimulus, no stimulus pattern was delivered. There was no significant response, and activity declines over the course of the trial. H. Lack of STP in Glu removes mismatch detection, and spike rates are high. I. Lack of STP in GABA results in sustained strong inhibition and sparse firing, but some mismatch selectivity remains for the second transition (p=0.004). J: Control with uniform pattern (A repeated 32 times). The spiking response rapidly drops to close to zero. K. Control with randomized pattern (one of pattern A to pattern E) on each pulse. There is a slow decay over the 32 pulses. L: Mismatch response is tuned to frequency of pattern repeats. The strongest responses are in the gamma range between 50 and 100 Hz. Response compares three post-transition vs three pre-transition pulses. Y axis is ratio, p-values are Binomial test for spike counts comparing post vs pre.). O: Schematic of gamma burst stimulus (green) repeated at theta frequency of 7.69 Hz (blue). Each burst consisted of a pattern repeated 5 times at 100 Hz. Panels N and O use the Binomial test to compare spike counts in the first theta cycle with those in the next three cycles. N: Theta modulated gamma burst responses showed strong spiking responses when each burst had a different pattern. O: Spiking in second, third and fourth theta cycles was lower than the first when each burst had the same pattern (p=1.9e-07, 3.1e-07, 6.68e-21).

(Schematic in Figure 8 M). When each burst was a different pattern, their amplitude was nearly consistent (Figure 8N), but the final burst was smaller than the first (p=0.0424, Binomial test). However, when the same pattern was repeated over successive bursts there was a steep decline in burst amplitude (Figure 8O, p=1.9e-7, 3.1e-7, 6.7e-21, Binomial test compared to first burst). Thus mismatch detection also works when the ensemble of neurons comprising a gamma burst changes between theta cycles.

In summary, our final set of model predictions showed that mismatch detection remains sharp in spiking neurons. The mismatch response also occurs for oddball (deviant) patterns, but not gaps. We confirmed that STP on both E and I synapses are required, and showed that mismatch detection also works for 100 Hz gamma-frequency bursts riding on the theta rhythm. Together, these support possible functional relevance of these mechanisms for spatio-temporal pattern selectivity in in-vivo-like network conditions.

Parameter sensitivity analysis

To conclude the characterization of our model, we asked: How robust is mismatch detection, and how do different network parameters affect it? We varied the five key network parameters: weights for Glutamate and GABA receptors, and the connection probabilities from CA3 to CA1, CA3 to interneurons, and interneurons to CA1 (Figure 9A). We also varied the stimulus pattern density, expressed as the percentage overlap of activity converging onto Glu synapses on CA1 due to any given pattern (Figure 9A, Figure 7-figure supplement 1, Figure 9-figure supplement 1).

We first conducted a simple parameter sweep, measuring mismatch selectivity as a function of different values of the six parameters (Figure 9B). To estimate selectivity, we repeated the design from Figure 6 panel D in which we simulated 6 distinct instances of the network and obtained the probability of mismatch detection for any given transition. The general outcome was that different pattern repetition frequencies exhibited distinct profiles of parameter dependence, with the 50Hz pattern having the greatest selectivity for most of the range.

We observed that sparse patterns (with low overlap) had stronger mismatch responses, particularly at 20 and 50 Hz (Figure 9Bi). There was little dependence on the weight of the Glutamate receptor. Mismatch was small for low values of wtGABA, supporting the role of inhibition in mismatch detection (Figure 9Biii). Greater values of excitatory synaptic projection probability, pCA3_CA1 led to lower selectivity (Figure 9Biv). This is complementary to the trend for pattern overlap (Figure 9Bi), which is expected since they similarly affect the number of activated synapses for each stimulus pattern. Both the inhibitory projection terms pCA3_Inter and pInter_CA1 showed a modest increase in selectivity with increasing connectivity (Figure 9Bv, 9Bvi). We interpret this as due to increasing overlap between input patterns, so that depression of inhibitory inputs carries over between patterns.

Since these runs showed considerable difference between the three reference pattern repetition frequencies, we performed a systematic analysis to find the frequency at which selectivity peaked. We plotted peak frequency as a function of the same set of six network parameters (Figure 9C). There was a small increase in peak frequency for intermediate levels of pattern overlap (Figure 9Ci). In general, peak selectivity was seen in the gamma frequency range. but at low values of GABA input the peak went down to 20 Hz (Figure 9 Ciii, Cv, and Cvi). High connectivity between CA3 and CA1 also resulted in a low (8Hz) peak frequency (Figure 9 Civ). Conversely, the highest tuning frequency was obtained for very low values of GluR weights (Figure 9Cii).

We finally tested four qualitative manipulations to the network (Figure 9D). In all cases we asked how selectivity changed compared to values obtained for a deterministic, subthreshold reference model. Reassuringly, stochasticity caused only a small decrement in selectivity. This supports the use of deterministic models as efficient proxies for the full stochastic version. Lack of STP, not surprisingly, completely abolished selectivity. Running the model at higher, more physiological temperatures gave increased selectivity. The introduction of spiking led to a considerable increase in variability between runs and simulated cells, but there was no significant change in overall selectivity.

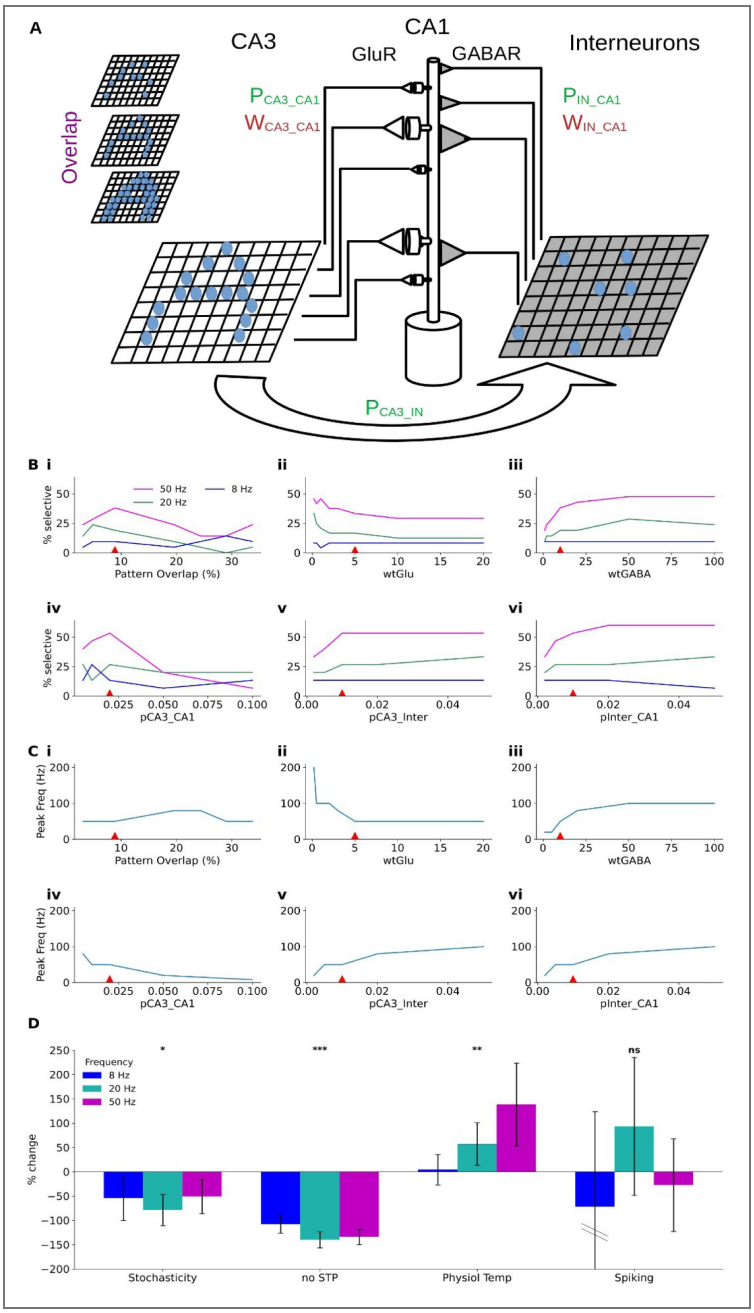

Figure 9. Parameter sensitivity of network model.

A: Schematic of model, indicating the six network parameters. Overlap specifies the fraction of postsynaptic axons which are activated by more than one optical spot as pattern density increases. W_{Glu} and W_{GABA} specify synaptic weights for gluR and GABAR synapses, measured as 1/ohm.m^2. P_{CA3_CA1} is the probability that a given CA3 neuron connects to the CA1 neuron. Similarly for P_{CA3_inter} and P_{Inter_CA1}. B: Pattern selectivity as a function of the six parameters. Red triangles indicate parameter values used for the reference model. Note the distinct selectivity profile for 8, 20 and 50 Hz, where 50Hz is almost always more selective over the entire range of parameters. C: Frequency of greatest mismatch detection as a function of the network parameters. The highest mismatch detection frequency can be tuned over a wide range by network parameters. D: Effect of global network changes on mismatch detection, compared to baseline deterministic model. Stochasticity significantly lowers mismatch detection (T=-2.33 p=0.022), but lack of STP completely eliminates it (T=-6.87, p=1.6e-9). Raising the temperature of the network to 37 degrees improves mismatch detection (T=2.88, p=0.0048). Introduction of spiking greatly increases trial-to-trial variability but there is no difference of the mean compared to the reference (T=0.007, p>0.99). For each of the runs and each frequency, the ratio (post-pre)/(post+pre) was taken for the 3 pulses before (pre) and after (post) the transition. % change = 100*(run_mean – baseline_mean)/baseline_mean. The three frequency terms were merged and Welch's T-Test was used to compare each run against the baseline run.

In summary, mismatch detection in our model is robustly present and can be tuned over a wide range of network parameters and model assumptions, with the notable exception that it is absolutely dependent on the presence of STP.

Discussion

We probed CA3-CA1 input-output properties for functional outcomes of pattern-specific short-term plasticity using spatially and temporally patterned optical stimuli. EI balance and summation properties tilted briefly to excitation on the second or third pulse of a burst due to differential STP profiles for excitation and inhibition. We parameterized a molecule-to-network multiscale model of CA3-CA1 network and plasticity using a series of burst, summation, and Poisson train inputs of optically defined input patterns. The model predicted that STP dynamics of E and I inputs provide a mechanism for single cells to detect transitions in input pattern sequences, which we then confirmed experimentally. We used the model to explore network configurations which could detect such transitions, and showed that spiking is strongly mismatch-tuned in continuous as well as theta-modulated gamma bursts. Overall, EI+STP based mismatch detection is robust over a wide range of network conditions.

Relevance to in-vivo computation

Slice physiology is, by definition, a reductionist way of investigating in-vivo circuit function. Here we have taken several steps to support our claims of relevance to brain computation. 1. We use optical patterned stimuli to stimulate a cross-section of CA3 neurons with a variety of distributed patterns, theta, and other frequency rhythms. These stimuli are sparser and more dispersed than Schaffer collateral electrical stimuli which tend to stimulate adjacent fibres and in most cases are very strong. 2. Our slice media match physiological media, and prior work in rat slices has shown that short-term plasticity properties are consistent in the 33-38 ℃ range (Klyachko and Stevens 2006b). Further, we show that the small 3.5 degree temperature increase to physiological levels strengthens, not weakens, our main finding of pattern mismatch detection. 3. Our model is a network + cell + synaptic signaling model, thus spanning multiple scales of function relevant to physiology. We factor in CA3 to CA1 connectivity distributions in addition to cell physiology and presynaptic signalling dynamics. We have, of course, simplified the network, most notably in the use of only one inhibitory interneuron class which maps to parvalbumin-positive fast-spiking interneurons with perisomatic connectivity. This level of detail was chosen as it was able to quantitatively fit a large number of observations with minimal circuit complexity. However, the experimental mismatch selectivity probability differed from the model (Figure 7E). We speculate that more accurate estimates of mismatch selectivity will require additional network detail. 4. We have extensively matched experiment to simulation at each of the specified levels: synaptic (Figure 4), cell (Figure 5, Table 1), and network (Figure 6, Table 1), in which we explicitly used Poisson input patterns and synaptic stochasticity to stress-test the model across scales. In almost all cases the simulation values fall within the range of measured cellular properties. 5. The prediction of mismatch detection is highly robust to network parameters (Figure 9), stimulus frequency (Figure 9), and stimulus timing jitter (Figure 7), and we confirmed it in slice experiments (Figure 7). This strengthens the case for it working in vivo.

A resource to model the CA3-CA1 feedforward circuit

A major outcome of our study is the development and parameterisation of a multiscale, chemical+electrical+circuit level model of the CA3-CA1 feedforward circuit, which runs rapidly even on laptop hardware (~20x slower than real time on an AMD 6800HS). Feature-wise, several studies combine signalling (typically postsynaptic spine and dendrite signalling) with electrical signalling (Bhalla 2017; Dainauskas et al. 2023; Dorman and Blackwell 2022; Mattioni and Le Novère 2013; Somashekar and Bhalla 2024; Bhalla 2011). Some of these combine compartmentalized signalling with standard branched neuronal electrophysiology calculations, as we do. Others include detailed 3-dimensional reaction-diffusion kinetics on spines(W. Chen et al. 2022) or boutons(Nadkarni et al. 2012, 2010) and these run much more slowly. Our current

model is distinct in that it is truly multiscale, closely constrained by experiment, yet runs on modest hardware. It incorporates the network, a conductance based model of a CA1 pyramidal neuron, and chemical kinetic models of a population of stochastic synapses on its dendrite.

Our network model is much reduced compared to models with exhaustive cellular and network-level detail(Markram et al. 2015). Its simplicity enables extensive exploration of the network parameters and comparison with recorded activity under a series of well-controlled stimulus patterns (Figures 4-9). For almost all tests, including molecular, single-cell, and network, the model was within the range of experimental readouts, but as discussed above, it may be necessary to extend the model with more interneuron subclasses to match experiment with respect to mismatch detection probability. (Figure 7 E).

Our model is modular. One can swap out different cellular geometries, provide distinct synaptic signaling models using SBML or compatible standards, and alter the detail of the network components. In the current study, we employed four different spine kinetic models, with different combinations of STP in E and I, simply by loading in different kinetic definitions. Thus the model is consistent with the 'Interoperable' and 'Reusable' aspects of FAIR principles (Eriksson et al. 2022).

EI balance is dynamically tuned through differential STP of E and I inputs

EI balance is a ubiquitous mechanism for controlling neural excitability. Numerous processes, including inhibitory plasticity, homeostatic plasticity, and developmental co-tuning have been proposed to underlie the origin and maintenance of EI balance (Agnes et al. 2020; Agnes and Vogels 2024; L. Chen et al. 2022; Jia et al. 2022; Lagzi and Fairhall 2024; Mackwood et al. 2021; Miehl and Gjorgjieva 2022; Trapp et al. 2018; Wu et al. 2022). EI balance is dynamic, due in part to differential effects of STP on excitatory and inhibitory inputs to the postsynaptic neuron (Bartley and Dobrunz 2015; Sun et al. 2018; Bartley et al. 2015; Wu and Zenke 2021; Klyachko and Stevens 2006a). However, the mode of delivery of these stimuli may lead to narrow timing and spatial patterning of activation of the inputs to CA1. For example, studies using field electrode stimulation of the Shaffer collaterals report a sustained shift to excitation during burst input (Klyachko and Stevens 2006a). In contrast, our sparse optical patterned stimuli results in a small window of escape from EI balance around pulse 2 or 3 in a burst (Figure 3), following which both E and I undergo depression to restore balance (Figure 3, 8). Thus, spatial patterning intersects with short-term plasticity to add another layer of timing control through gating of E-I balance (Rotman et al. 2011).

STP leads to single-neuron mismatch detection in pattern sequences

Where can temporally precise gating be useful? At the single-synapse level, synaptic depression performs the operation of decorrelation, leading to more efficient coding (Goldman et al. 1999; Rotman et al. 2011). Our observations can be framed as decorrelation of the spatial pattern (alternatively, activity vector) of multi-synaptic input converging onto a neuron(Kremkow et al. 2010). A putative example of this is place field formation in novel environments. Dombeck and co-workers (M. E. Sheffield and Dombeck 2019; M. E. J. Sheffield et al. 2017), found that dendritic inhibition is reduced when a mouse traverses a new environment. Consistent with this, our simulations predict elevated spiking when novel patterns occur, in part due to presynaptic depression of inhibition (Figure 7,8).

Mismatch detection has been extensively studied at the whole-organism level, particularly in the context of a large EEG transient following an unexpected stimulus in a regular stream of events. This is known as mismatch negativity. There is a vigorous debate on the mechanisms of auditory mismatch negativity (e.g., (Garrido et al. 2009; May and Tiitinen 2010; Näätänen et al. 2005)) of which the fresh-afferent model maps to part of our proposed mechanism (Figure 10A). Leaving aside the obvious differences between auditory cortex and hippocampus, we frame our model as a transient differential tilt in EI balance (Figure 3, Figure 8A,B, Figure 10B), in distinction to the fresh-afferent model. This makes our model robust over a wide range of stimulus and network conditions (Figure 9), and has the functional implication that transient responses remain at about the same amplitude over a prolonged stimulus sequence (Figure 8B, Figure

10B), rather than declining. We examined only three of several possible stimulus changes for mismatch detection: Change in pattern, a single oddball stimulus, and a gap. Of these, our model detected the first two. We speculate that two circuit elaborations may extend the applicability of our model to more categories of mismatch. First, feedback inhibition in CA1 through other interneuron classes might introduce a time-delay element capable of resolving gap stimuli. Second, upstream areas may encode higher order stimulus features such as gaps, duration, intensity, localization, and frequency steps into distinct input patterns. Our proposed EI-balance shift mechanism could be a common end-point for all of these. This would transform quite complex mismatch detection tasks into a uniform computation of pattern change, generalizing the mechanism to stimuli which were previously considered to require a more complex network-level implementation (Garrido et al. 2009; May and Tiitinen 2010; Näätänen et al. 2005).

We note that the time-scale of our mismatch response (~125 ms) is similar to the 100 to 200 ms of the classic auditory mismatch negativity (Butler 1968). A similar computation of stimulus-specific adaptation in the auditory cortex has been modeled using a recurrent network with short-term depression(Yarden and Nelken 2017). Our findings of pattern mismatch detection may also provide a mechanistic interpretation of published results showing behavioural and physiological selective responses to changes in visually delivered patterns(M. E. Sheffield and Dombeck 2019). The authors found that a rate model with short-term depression was able to replicate the experiments. In a recent study, signatures of prediction error (implemented by absence of conditioned response) were observed in recurrent cortical networks in organotypic preparation(Liu and Buonomano 2024). These prediction errors were visible after a 24-hour long training period that achieved the associative conditioning. Thus the study showed the role of inhibition stabilized attractor networks of cortical circuits to produce prediction-error like responses in single neurons. Our model achieves equivalent computations with simple feedforward connectivity at a single-neuron level, without training, and with direct linkages to the underlying physiological mechanisms.

Both our experiments and models show selectivity for specific transitions. This suggests a further computation of sequence disambiguation. Consider sequence S1 AAAABBBBCCCC and sequence S2 FFFFBBBBGGGG, overlapping in ensemble B. We stipulate the presence of neuron $S1_{AB}$ which detects the A->B transition, and so on. Then S1 is uniquely identified by the activity of $S1_{AB}$,$S1_{BC}$, and S2 by $S2_{FB}$,$S2_{BG}$. This is a rapid and parsimonious mechanism for distinguishing two intersecting sequences such as time-cell sequences (Modi et al. 2014), on sub-second time-scales.

Mismatch detection is pronounced in the gamma band

Gamma oscillations have been implicated in memory formation and communication between brain regions (Van Vugt et al. 2010; Misselhorn et al. 2019). Gamma bursts are typically modulated by the theta rhythm (Lisman and Jensen 2013), which is itself closely coupled to sensory intake such as sniffing (H Eichenbaum et al. 1987; Tsanov et al. 2014) and whisking(Grion et al. 2016), and also to movement (Joshi et al. 2023). Our proposed mechanism for mismatch detection is enhanced precisely in the gamma range (Figure 9). Further, we find that theta-modulated gamma bursts perform mismatch detection between theta cycles (Figure 8 N,O). We propose that sensory snapshots obtained through sniffs or whisks provide the CA1 with theta-modulated gamma bursts of stimulus-specific activity vectors. When inputs change from one theta cycle to the next, individual cells in CA1 light up to detect specific changes between stimuli, such as odor 1 changing to odor 2, or texture 1 to texture 2 (Figure 7, 8). This implements a dimensionality reduction of a sequence of sensory inputs into a trajectory through a space of stimulus transitions.

Methods

Animals

Experiments were conducted on a mouse line with the expression of cre-recombinase specific to hippocampal CA3 (Grik4Cre) obtained from Jackson laboratory (ID: 006474). The animals were housed in a cage with up to 6 cage mates and under a 14/10 light/dark cycle. Food and water were

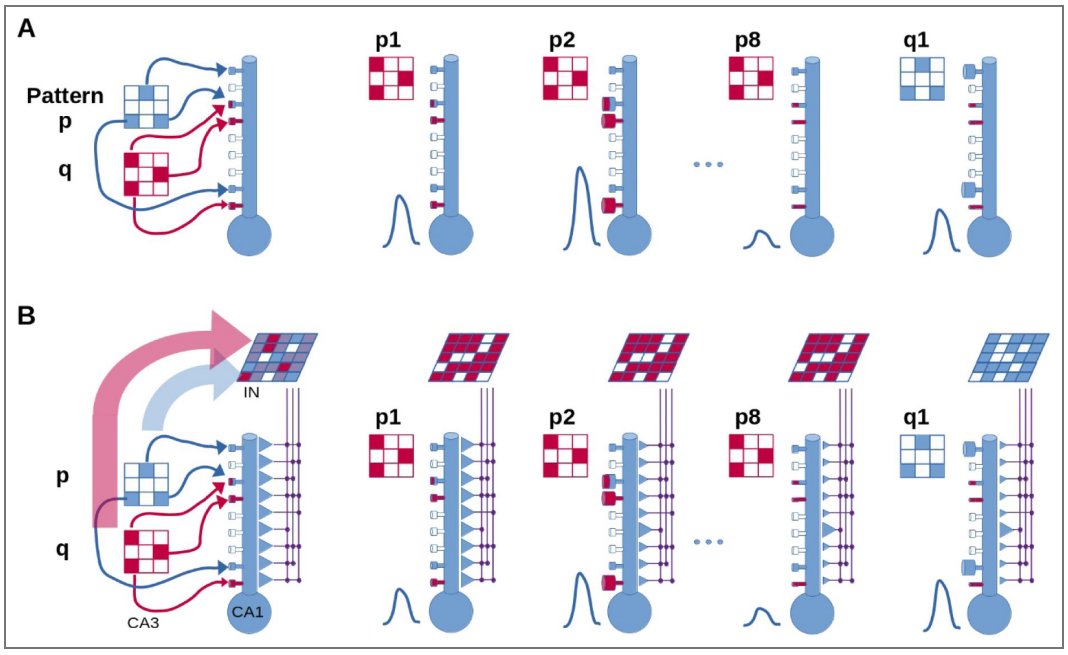

Figure 10. Proposed mechanisms for mismatch detection.

A: Fresh-afferent model. Left: Circuit involving only excitatory synapses from CA3 to CA1. The two input patterns p and q (in the CA3) have only a little overlap. Right: on successive stimulus p repeats, the STP in the synapses (indicated by spine size) leads first to an elevated response, and then to depression. When the stimulus changes to pattern q, most of the afferents are fresh so we get an elevated response. B: EI-balance shift model. The excitatory component of the circuit is as in A, but in addition there is an intermediate interneuron layer receiving input from the CA3. During a train of pulses of pattern p, E transiently exceeds I, then both undergo STD. When a different pattern q arrives, there is again a transient advantage for the E input because the two-stage connectivity leads to substantially overlapping input on the I inputs, so most of them are still depressed. Overall, the transient response at p2 and q1 are closer in amplitude, or equivalently, the pattern selectivity is less dependent on the averaged activity history.

provided ad libitum. The housing and health were managed as per the National Centre for Biological Sciences Institflexutional Animal Ethics Committee (IAEC) guidelines (Project: NCBS-IAE-2022/8 (R2ME). Only transgenic F1 mice, identified with genotyping, of both sexes were used for experiments.

Virus Injection

Transgenic mice between the ages 27-35 days were selected for virus injections. These animals were transferred to a separate holding facility where they were kept till the terminal experiment.

Virus: We used an adeno-associated virus AAV-FLEX-rev-ChR2-tdtomato (Addgene 18917) to express channelrhodopsin2 in CA3 pyramidal cells in a cre-lox-dependent manner. The virus was diluted using sterilised PBS to a titre of 1-5 x 10^{12} GC/ml and stored at –80°C in aliquots. The animals were injected with a dose of 300-500 nl of virus suspension in 10-20ms long pulses of pressurised nitrogen using a Picospritzer (Parker-Hannifin, USA). The animals were then allowed to recover under supervision and veterinary care. Terminal experiments were performed after an incubation period of 35 days or more, resulting in cre-lox-dependent expression of channelrhodopsin2 (ChR2) specific to the CA3 region of the hippocampus on the injected side. The virus AAV-FLEX-rev-ChR2-tdtomato was a gift from Scott Sternson (Addgene plasmid #18917; *http://n2t.net/addgene:18917*; *RRID:Addgene_18917*)(Atasoy et al. 2008).

Electrophysiology

Slice preparation: Animals aged between 56-120 days and at least 28 days after the virus injection were used for in vitro experiments. The animals were humanely euthanised using isoflurane (Forane) and brain was harvested into ice-cold slush of cutting solution (87mM NaCl, 2.5mM KCl, 7mM $MgCl_2.6H_2O$, 0.5mM $CaCl_2.2H_2O$, 25mM $NaHCO_3$, 1.25mM NaH_2PO_4, 75mM Sucrose) maintained over ice and aerated with carbogen (95% O_2 + 5% CO_2). After a rest period of 2 minutes, the hippocampus from the injected side was dissected out, and 350 µm thick sections were made using a vibrating microtome (Leica VT1200) submerged in the above-mentioned solution. The hippocampal sections were collected in a beaker filled with the recording solution (124mM NaCl, 2.7mM KCl, 1.3mM MgCl2.6H2O, 2mM CaCl2.2H2O, 26mM NaHCO3, 1.25mM NaH2PO4, 10mM D-(+)-glucose, pH 7.3-7.4 and osmolarity of 305-315 mOsm) at room temperature and allowed to recover for one hour in the dark before starting the experiments.

Recording Setup: Electrophysiological recording and optical stimulation was done on an upright DIC Olympus 53WI microscope. A slice hold-down (Warner Instruments WI 64-0246) was used to keep the slice from moving. The recording bath was perfused with the recording solution at a rate of 2 ml/min with a peristaltic pump. The recording solution was kept aerated with carbogen and the influx of the solution into the recording chamber was heated using an inline heater (Warner Instruments TC-324B) to 32-33°C.

Electrical activity was recorded using a headstage amplifier controlled by a patch clamp amplifier (Multiclamp 700B, Axon Instruments, Molecular Devices) and a data acquisition system (Digidata 1550B, Axon Instruments, Molecular Devices) using Multiclamp commander (Molecular Devices) and custom written protocols in Clampex (Molecular Devices). The electrophysiology data was acquired at 20kHz and filtered in the 0-10kHz band.

In some experiments, another recording electrode was used to record extracellular responses in the CA3 cell layer. Whole cell patch clamp recordings from CA3 and CA1 cells were made using borosilicate glass micropipettes pulled using tungsten filament puller (P1000, Sutter Instruments) and filled with an internal solution containing 130mM K-gluconate, 5mM NaCl, 10mM HEPES, 1mM Na_4-EGTA, 2mM $MgCl_2$, 2mM Mg-ATP, 0.5mM Na-GTP and 10mM Phosphocreatine, pH ~7.3, and osmolarity ~290 mOsm. For voltage-clamp recordings, K-gluconate was replaced with Cs-Gluconate. Field response was often biphasic with multiple cycles, hence, a peak-to-peak value was used.

The cells were either recorded in the current clamp or the voltage clamp. In current clamp recordings, the cells were maintained at a membrane potential of –70 mV. Cells were rejected if the membrane potential changed by 5mV over the course of the recording, holding current either was above 100 pA or changed by more than 25 pA to maintain the mentioned membrane potential. In voltage-clamp recordings, the cells were rejected if the series resistance crossed 25 MΩ or changed by 30% of the initial value. Liquid junction potential was calculated to be 16.926 mV according to the stationary Nernst–Planck equation (Marino et al. 2014) using LJPcalc (*RRID:SCR_025044*) and was not compensated.

In optogenetic preparations, the additional stimulation that comes in due to the excitation of axons and dendrites can not be ruled out. To assess that, we patched a CA3 cell and recorded its optical depolarization caused by a single spot of light in a grid using a whole-cell voltage clamp. The CA3 cells have a large receptive field that arises due to the expression of ChR2 on their dendritic arbour. This receptive field is stronger closer to the soma but spans on both sides of the dendritic tree (Figure 1-figure supplement 1A). A patched CA3 cell fired action potential with 100% success (Figure 1-figure supplement 1B) when the cell layer was stimulated with patterns with multiple spots. A single spot, on the other hand, was only sufficient to induce action potentials when directly incident on soma (Figure 1-figure supplement 1B).

Calculation of free calcium in the recording solution

We estimate the free calcium in our solution is ~1.37 mM since the 2 mM CaCl2 is buffered by the 1.25 mM NaH2PO4 and the NaHCO3. Mg2+ will also be buffered but to a smaller degree. The calculation is as follows.

Our solution composition was 124mM NaCl, 2.7mM KCl, 1.3mM $MgCl_2$, 2mM $CaCl_2.2H_2O$, 26mM $NaHCO_3$, 1.25mM NaH_2PO_4, 10mM D-(+)-glucose, pH 7.3-7.4 and osmolarity of 305-315 mOsm.

Let pK_{a_2} = 6.8 (physiological solution range),

And our measured pH is~ 7.35:

Then $[HPO^{2-}]/[H\ PO^{-}] = 10^{(pH - pKa2)}$

Thus the ratio is 10^0.55 = 3.55. The base fraction = ratio(1+ratio) = 0.78 (Mauger 2017) Hence free $[HPO^{2-}]$ ~1.25*0.78 = 0.98 mM.

For the buffering, Ca^{2+} +HPO^{2-} ⇌ CaHPO, 1/Kd ~ 200/M (Moreno et al. 1966) Hence complexation ratio for phosphate is 200M^-1 * 0.00098M = r_{po4} = 0.2

Similar calculation for HCO_3 gives 0.38 as follows:

$pK_{a_2}(HCO_3^-/CO_3^{2-})$ ≈ 10.33 at 25 °C (weak T, I dependence).

$[CO_3^{2-}]/[HCO_3^-] = 10^{(pH–pK_{a_2})} = 10^{(7.35–10.33)} \approx 1.05\times10^{-3}$.

With 26 mM HCO_3^- → $[CO_3^{2-}]$ ≈ 0.026 mM. (Mojica Prieto and Millero 2002)

Ca–bicarbonate complex ($CaHCO_3^+$)

Formation constant (log β_1) ≈ 1.11 at 25 °C → $\beta_1 \approx 12.9\ M^{-1}$.

Complexation ratio $r_{HCO3} = \beta_1 \cdot [HCO_3^-] \approx 12.9 \times 0.026 \approx 0.335$. (Plummer and Busenberg 1982)

Ca–carbonate neutral pair ($CaCO_3^0$(aq))

Formation constant (log β) ≈ 3.22 → $\beta \approx 1.66\times10^3\ M^{-1}$.

Complexation ratio $r_{CO3} = \beta \cdot [CO_3^{2-}] \approx 1.66\times10^3 \times 2.6\times10^{-5} \approx 0.045$.

$r_{carbonate} = r_{HCO3} + r_{CO3} \approx 0.335 + 0.045 \approx 0.38$.

Combining contributions from the two buffers, Free Ca^{2+} = 2mM /(r_{po4} + $r_{carbonate}$) = (2mM / (1+0.2 + 0.38) ~ 1.27 mM.

Optical Stimulation

Pyramidal cells in the CA3 cell layer expressing channelrhodopsin were stimulated using a DMD-based patterned projector system (Polygon 400G, Mightex Systems, Canada) using a spot size of approximately 14μm x 7.8μm under a 40x water immersion objective. The spots (or squares) made a hexagonal grid with an inter-spot spacing equal to 32 μm.

The grid occupied the middle 2/3rd of the projector frame (336μm x 187.2μm), and the microscope was translated on a stage to make the grid part overlay on the CA3 cell layer under a 40x objective. In 1-square stimulation experiments, the CA3 cell layer was illuminated one spot at a time with an interstimulus time of 3 seconds to avoid desensitisation of channelrhodopsin. In other experimental protocols, 5-spot and 15-spot patterns were used at various stimulation frequencies. There were five different non-overlapping patterns of 5-spots, and three non-overlapping patterns of 15-spots. Each presentation of a pattern was for 2-5 milliseconds. The light source had a total estimated maximum intensity of 6.7 mW, and for the grid size used, each spot had an absolute power of approximately 14.47 μW and a power density of 100 mW/mm^2. For all experiments, unless mentioned, the intensity of light was kept at 100%. Optical stimulation patterns were made and loaded onto Polygon using Polyscan2 (Mightex, Canada) and triggered using time series generated from custom protocols written in Clampex (Molecular Devices) and communicated to Polygon using Digidata 1440 DAC. A phototransistor (OPT101) was placed behind the dichroic to acquire the light stimulus waveform using the DAq and recorded along with the patch-clamp time series data.

Code and Model accessibility

All scripts and models for performing simulations for figures are presented in the GitHub site *https://github.com/BhallaLab/STP_EI_paper_figs*. Simulations were run using MOOSE 4.0 compiled using gcc version 11.4.0 and Python version 3.10. Short calculations were run on Ubuntu 22.04 on an 8-core laptop, and large runs were done on a 128-core server also running Ubuntu 22.04. All software used is open-source and hosted on github. MOOSE is available at *https://moose.ncbs.res.in* and *https://github.com/BhallaLab/moose*. Optimization of presynaptic models was performed using HOSS 1.0(Nisha Ann Viswan et al. 2024) (*https://github.com/BhallaLab/HOSS*) and FindSim(Nisha A. Viswan et al. 2018) (*https://github.com/BhallaLab/FindSim*).

Presynaptic Plasticity Model

Voltage clamp data from the pulse-train experiments (Figure 3) was used to train a model of presynaptic short-term plasticity (Figure 4A, Figure 4-figure supplements 1, 2, 3) implemented in MOOSE (Ray and Bhalla 2008). The model included presynaptic signalling, activation of postsynaptic glutamate and GABA receptors, and electrophysiology of a ball-and-stick model of the postsynaptic neuron held in the voltage-clamp. The glutamate receptors were placed on dendritic spines implemented as separate electrical compartments, and the GABA receptors were on the dendritic shaft. Model fitting was performed in two stages. First, the raw voltage-clamp experimental data files in hdf5 format were analysed using a Python script and the peaks and valleys for each trial were extracted and stored in an intermediate hdf5 file. Second, the HOSS pipeline (Hierarchical Optimization of Systems Simulations) (Nisha Ann Viswan et al. 2024) was used to fit the presynaptic signalling model to this data, uniquely for each cell and separately for excitatory and inhibitory synapses. There were ten to eighteen 'experiments' run on the model to perform the fitting for each cell: Two experiments for each frequency, two to four pulse frequencies (depending on how many were feasible in each patch recording), and an additional experiment for time-course of neurotransmitter release. All this was done for 5-square and 15-square stimulation, respectively. For each frequency (typically 20, 30, 40, and 50 Hz pulse rate), we performed peak-to-valley comparisons with experiments for eight pulses in a trial and paired-pulse response experiments focusing on the first couple of pulses. The simulations for the experiments were performed using MOOSE to compute the somatic voltage-clamp response to synaptic input on the dendrite of a ball-and-stick cellular model.

The synaptic input was obtained using mass-action simulations of presynaptic signalling for the model in Figure 4A. This, too, was part of the multiscale MOOSE model. Excitatory synapses were implemented as boutons connecting to a dendritic spine with a compartment for the spine shaft and spine head, respectively. The simulated neurotransmitter release triggered the opening of ligand-gated receptor channels for AMPA and NMDA receptors placed on the spine head. Inhibitory synapses were implemented as presynaptic boutons with the same chemical topology but different kinetics (Figure 5A) and coupled now to GABA receptors placed on the dendritic shaft.

This entire process was repeated for excitatory and inhibitory synapses, respectively. All calculations for the optimisation were run deterministically since, otherwise, massive averaging would be needed for each estimate of voltage-clamp current. Equations, kinetic parameters, and concentrations for the STP and no-STP models are in Supplementary Tables 1 and 2.

Postsynaptic neuron model

The postsynaptic neuron model (Figure 4B) was a ball-and-stick model with a soma compartment of 10 μm length and 10 μm diameter and a single dendritic compartment of 200 μm length and 2 μm diameter. The dendritic compartment was ornamented with 100 evenly spaced spines, each containing a spine shaft and a spine head compartment. The spine head had a model of the AMPA receptor, the NMDA receptor, and calcium dynamics resulting from influx through the NMDA receptor. However, calcium dynamics were not utilised for any further calculations. A separate presynaptic bouton with the glutamate release kinetic model was apposed to each spine head.

The dendritic compartment also had 200 evenly spaced inhibitory synapses, likewise apposed to presynaptic boutons with the GABA release kinetic model.

Under the passive conditions of our model (RM =1.0 Ω.m^2, RA = 1.0 Ω.m) the length constant of this model was ~700 μm, which is much longer than the geometrical length. Hence space clamp problems are unlikely. Furthermore, the short electrotonic length means it does not matter if the Glu and GABA receptors are interspersed as opposed to GABA being more proximal.

The soma had voltage-gated Na and delayed rectifier K_DR channels in the Hodkin-Huxley formalism with kinetics drawn from previous models(Traub et al. 1991). For most models, the Na and K_DR conductances were held to small values (6 and 3.5 Siemens/m^2, respectively) as we

were interested in linear somatic integration, but for spiking simulations, we increased Na and K to 400 and 450 Siemens/m^2. Equations and kinetics for the voltage-gated and ligand-gated channels in the model are presented in Supplementary Table 3.

Network model

We implemented a simple two-layer network model converging onto a single CA1 neuron. As input, the network had a 16×16 array of integrate-and-fire neurons for the CA3. There was another 16×16 array of inhibitory interneurons implemented as sum-threshold units (Figure 5C). Excitatory projections from CA3 to the 100 synapses on the CA1 neuron were implemented as a 256×100 matrix. Default entries for the connections were zeros, and ones were filled in at random with a probability pCA3_CA1 as indicated in the table. Similarly, projections from CA3 to interneurons were defined as a 256×256 matrix with connection probability pCA3_Inter. Projections from the interneurons to the 200 GABA synapses on the CA1 neuron were a 256×200 matrix with default connection probability pInter_CA1. All told, there were just seven parameters in this model (Table 2), of which only six were varied.

Each optically stimulated spatial pattern of activity in CA3 was converted into a vector of ones and zeros by thresholding the CA3 membrane potential, calculated as per the next section. Activity on the vector of glutamatergic synapses was:

Glu synapse vector:

$$=$$

Synaptic activity was thresholded at 1 to drive the presynaptic signalling. Similarly, Interneuron vector:

$$((\text{CA3\_InterneuronConnections} \times \text{CA3\_vector}))_{\text{GAB}}$$

A synapse vector:

$$=$$

Stimulus model

To deliver the stimulus, we defined a set of eight input patterns. These were hand-coded as 8×8 grids of ones and zeros, set up to resemble the letters A through H. We expanded the 8×8 patterns into 16×16 patterns by replicating the pattern twice over the array (Figure 4-figure supplement 6). For the first five patterns we zeroed out a specified number of entries on the 16×16 pattern using the parameter 'zeroIndices' to adjust sparseness. This zeroing out was done irrespective of the original state of the entry. For the default level of sparseness (75%) the first five patterns (A through E) had 18 to 26 nonzero squares. The last three patterns (F through H) were dense, with 144, 152 and 152 squares.

The product term:

$$*$$

sometimes led to very different numbers of active glutamate synapses, differing by as much as 50% between patterns. Hence we carried out a preliminary calculation to fill in entries in the connection matrix to bring the final synaptic activation for all the 5-square patterns to roughly the same level (within 15%). For the default 75% sparseness this came to between 35 and 38 active glutamatergic synapses (Figure 7-figure supplement 1).

During the simulation runs we provided a time-series of patterns according to frozen Poisson timing series with a mean of 20 Hz (Figure 6) or a time-series of four patterns each repeated 8 times, at 8, 20 and 50 Hz (Figure 7). The time-series was generated with a resolution of 0.5 ms, and the stimulus duration (activation of Ca influx into the presynaptic boutons) was 2 ms. We used a fixed delay of 5 ms between the Glu and GABA synapse activation.

We implemented ChR2 desensitisation and membrane potential buildup over multiple pulses on the CA3 neurons using the following equations:

$$\frac{dG}{dt} = \frac{1-G}{\tau_R}$$
$$\frac{dV_m}{dt} = \frac{E_{\text{rest}} - V_m}{\tau_M}$$

For each light pulse, we updated G and Vm as follows:

$$G = G \cdot \exp\left(-\left(D_0 + \frac{D_1}{\Delta t}\right)\right)$$
$$V_m = V_m + \tau_O \cdot \frac{E_{\text{ChR 2}} - V_m}{\tau_C} \cdot G$$

Where

G = conductance of ChR2
V_m = CA3 pyramidal neuron membrane potential
Δt = time since last stimulus
D_0 = basal desensitization of ChR2 = 0.01
D_1 = light pulse induced desensitization of ChR2 = 0.0004
τ_R = Recovery time course of ChR2 from desensitization = 1.5 s
τ_M = Membrane time course of CA3 neuron = 10 ms
τ_C = Time course to charge CA3 neuron when ChR2 is open = 5 ms
τ_O = ChR2 channel open time = 1 ms

Example pulse trains with these parameters are illustrated in Extended Figure 6.

Simulation parallelization and Visualization

Model fitting (Figure 4) and data generation for multi-trial stochastic runs (Figures 6, 7, 8, and 9) involved parallel calculations. The stochastic runs, in particular, were embarrassingly parallel in that they required multiple repeats of the same model with different random seeds. This was orchestrated through Python scripts using the multiprocessing library. The calculations were carried out on a 128-core AMD Epyc 7763 server. Data from these runs was organised into pandas data frames and dumped into hdf5 files in the same format as the experimental data. Figures 4, 6, 7, 8 and 9 were generated from these data files using pandas, Matplotlib and Python scripts.

3-D model visualisation (Figure 4 and Supplementary movie) was performed using the built-in interface within MOOSE, to the 3-D graphics library *vpython*.

Supplementary Figures

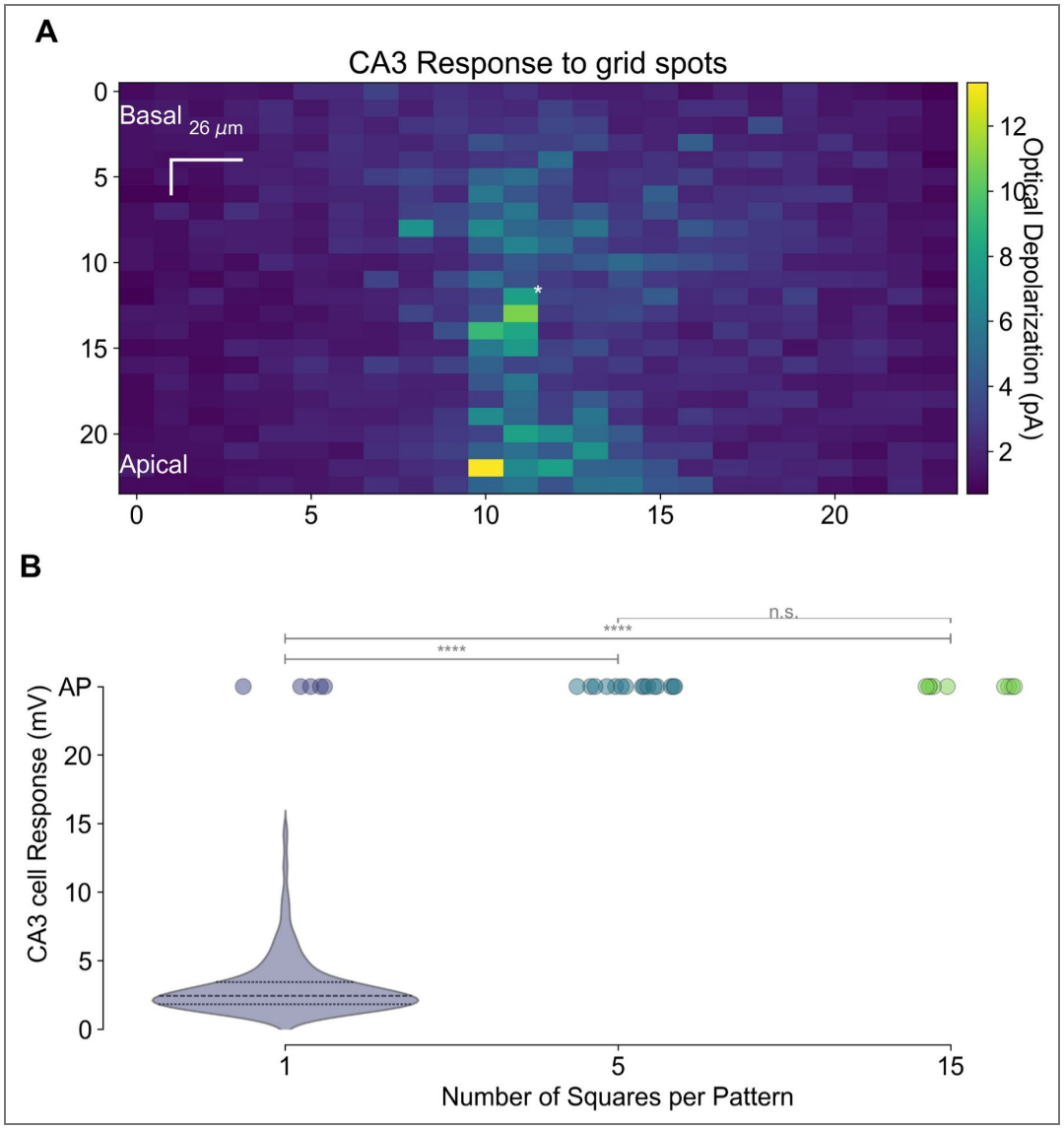

Figure 1-figure supplement 1. A) Heatmap of optogenetic depolarisation of a single CA3 pyramidal cell obtained by single spots of light in a 24×24 grid while keeping the patched PC in the centre of the frame (asterisk). B) Distribution of optical depolarization in CA3 PC against patterns of size 1 square (single spots), 5 squares, or 15 squares. Filled circles denote the instances when the patched cell fired an action potential. For patterns of size 5 and 15, all the trials resulted in spikes, hence there is no subthreshold distribution of EPSPs. For 1-square patterns, four out of 576 spots induced a spike.

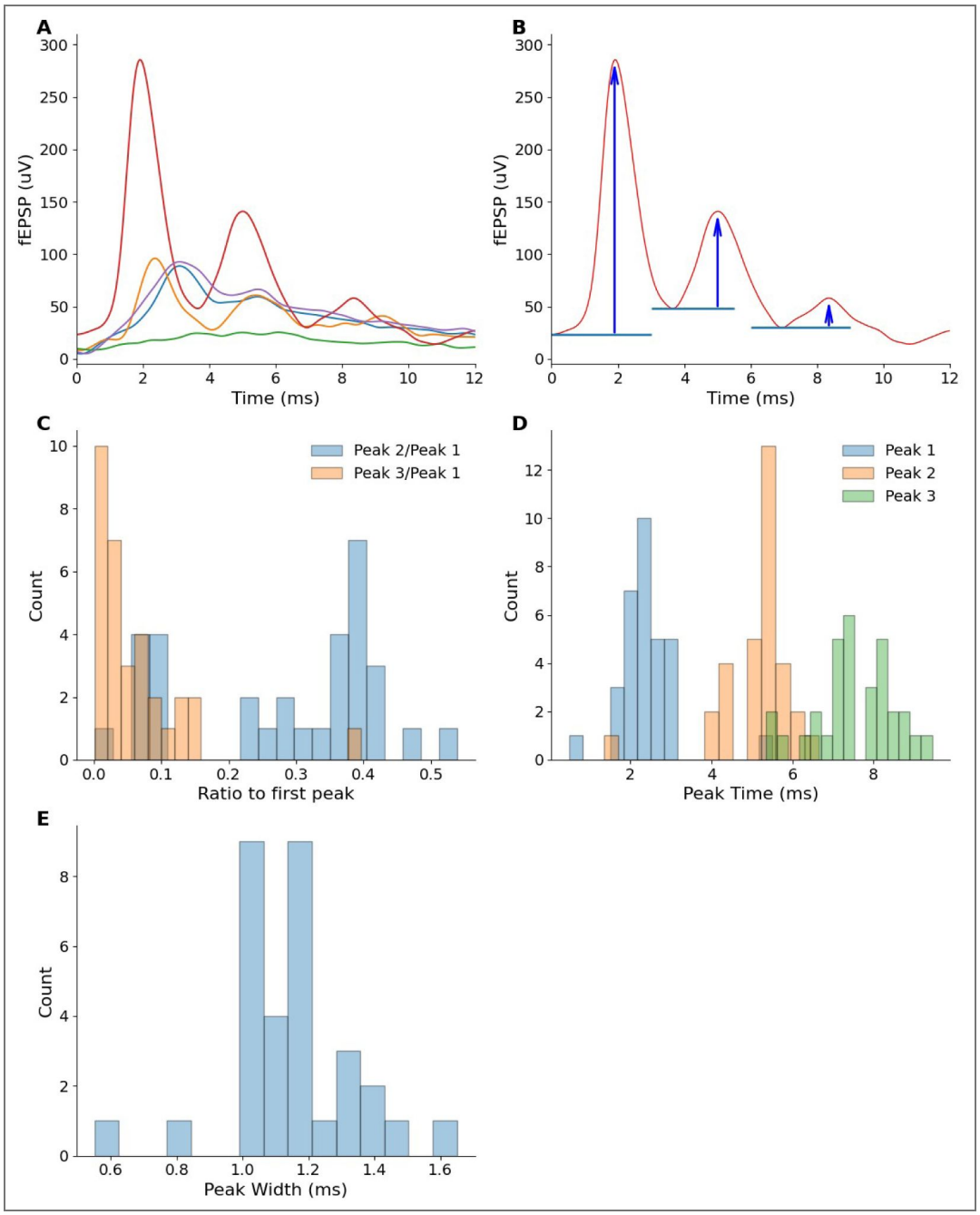

Figure 1-figure supplement 2. Optically-triggered 'ringing' response in CA3 field recordings. A: Sample traces. B. Methodology for computing peak heights. For each peak we computed the fEPSP elevation with respect to the immediately preceding valley. C. Peaks decline rapidly. The median of the second peak was ~40% of the first peak, but the third peak was < 5%. D. Peak times following optical pulse (of 2 ms). The third peak occurred within <10ms. E: fEPSP Peak Width distribution centred around 1.2 ms, but no peak was wider than 1.6 ms, suggesting tight synchrony in case multiple CA3 neurons were spiking.

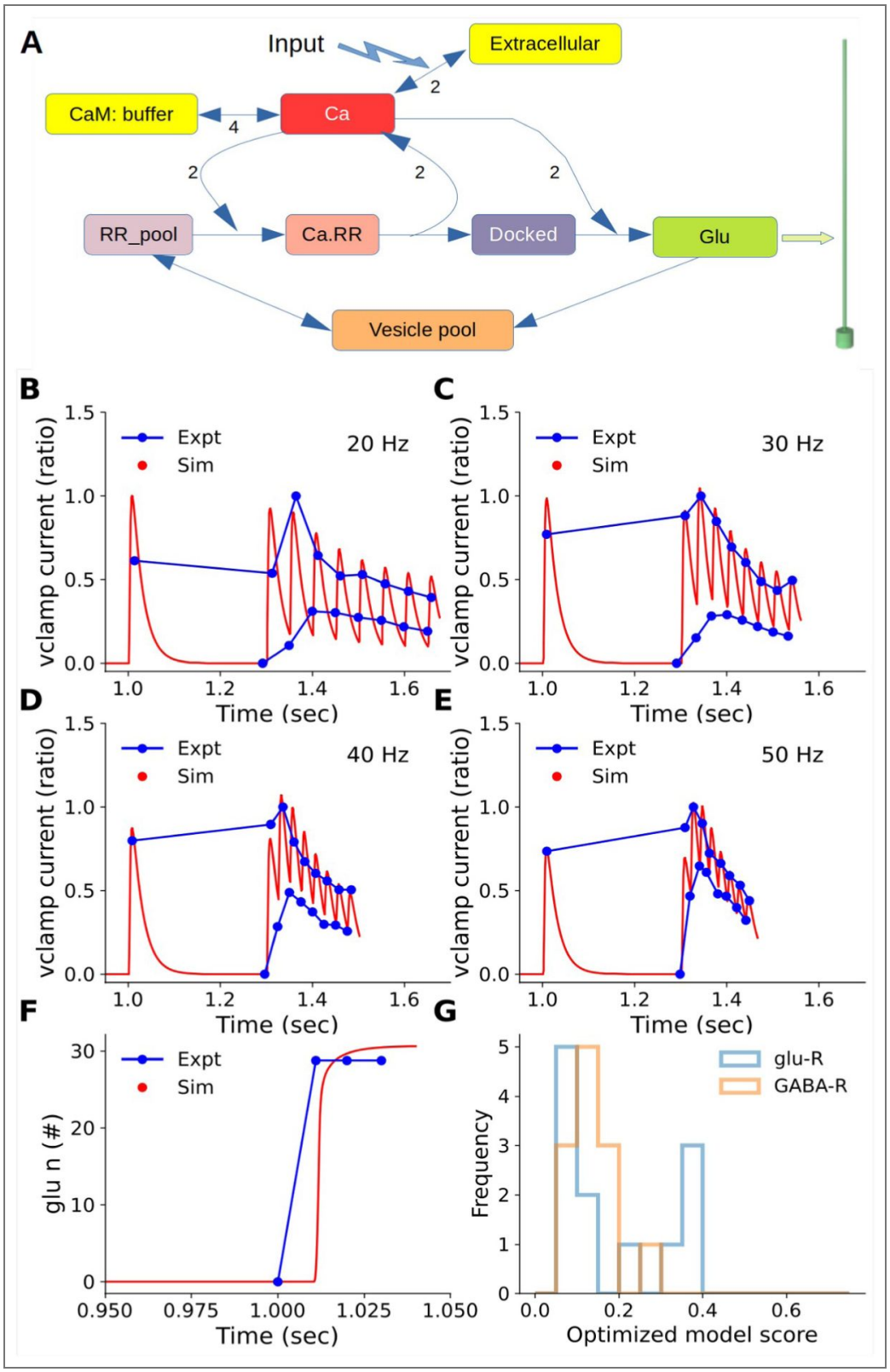

Figure 4-figure supplement 1. Fitting the presynaptic kinetic model to EPSC and IPSC data, for cell 7492. A: Model of reaction system in each bouton. Numbers next to reaction arrows indicate stoichiometry. Synaptic input triggers a reaction causing extracellular Ca2+ to enter the bouton, and a pump removes the Ca. CaM buffers the Ca2+. Ca binds/unbinds from successive stages of the readily releasable (RR) pool of vesicles till they are docked, at which point the final Ca-binding step causes synaptic release. The released neurotransmitter (Glu for excitatory synapses, GABA for inhibitory) opens a ligand-gated receptor channel on the postsynaptic CA1 neuron, which is held voltage-clamped.(green arrow). The reaction scheme was identical for Glutamatergic and GABAergic

synapses, but the rates were different to fit to the voltage-clamp recordings. B-E: EPSC fits for 20, 30, 40 and 50 Hz, respectively. Blue traces are experimental peaks and valleys averaged over all repeats and all 5-square patterns. Red traces are simulated EPSCs. F: Cumulative release curve for glutamate vesicles. Blue: expected transmitter release completion within 10 ms based on our observations of rapid postsynaptic responses from Figure 1 H,K. Red: simulated release. G: Distribution of model fitting scores for all cells and for glu and GABA receptors. Scores are normalised RMS differences between experimental and simulated points, as in panels B-F. Any score below 0.3 is a good fit.

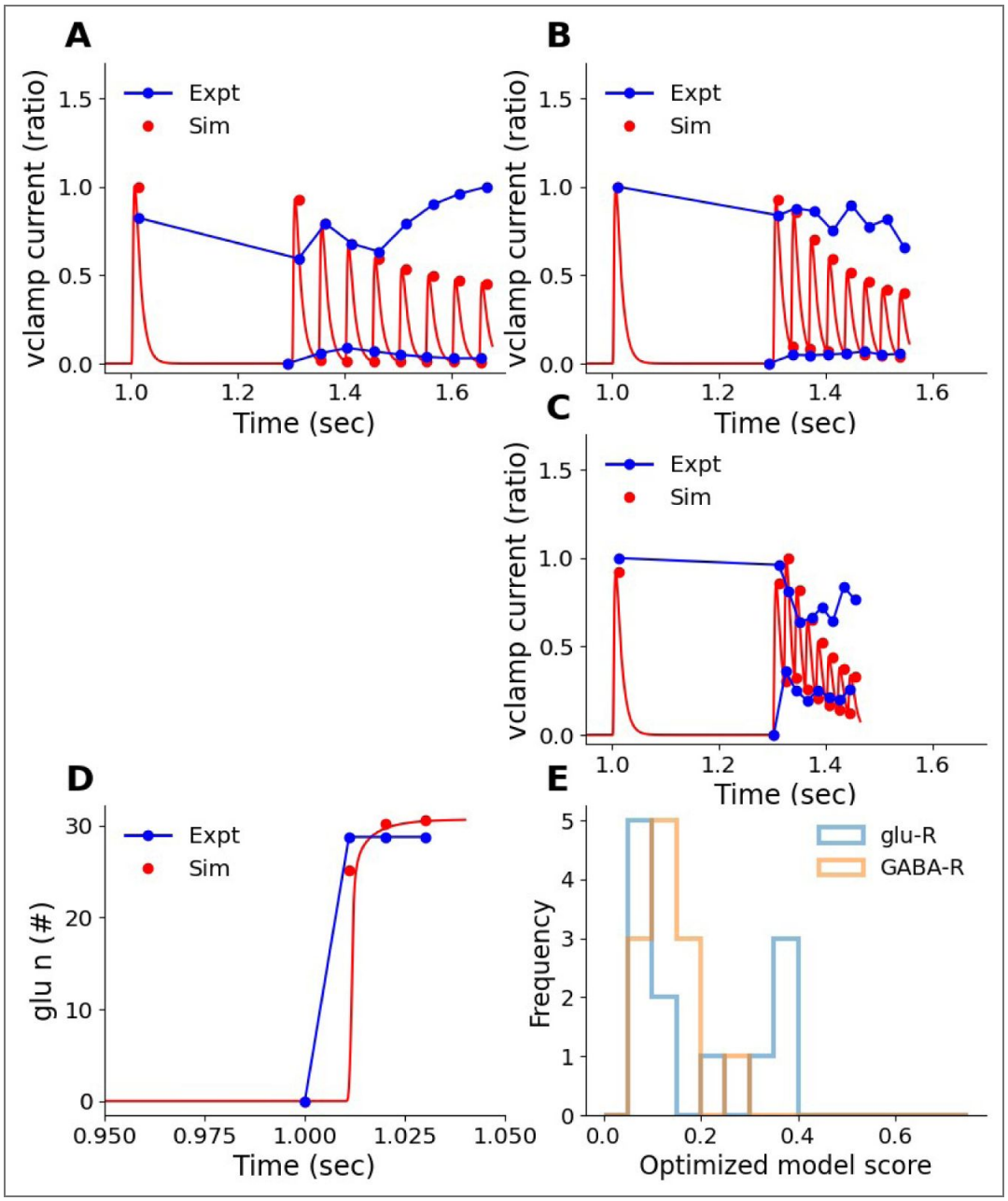

Figure 4-figure supplement 2. Example model fits for cell 6201. Here, the 40 Hz data was not recorded. A, B, C: EPSC fits for 20, 30, and 50 Hz, respectively. Blue traces are experimental peaks and valleys averaged over all repeats and all 15-square patterns for neuron 6201. Red traces are simulated rectified EPSCs. Note that the experimental traces are noisy hence the fits miss some of the peaks. D: Cumulative release curve for glutamate vesicles. Blue: target release complete within 10 ms. Red: simulated release. E: Distribution of model fitting scores for all cells and for glu and GABA receptors. Scores are normalized RMS differences between experimental and simulated points, as in panels A-D. Any score below 0.3 is a good fit.

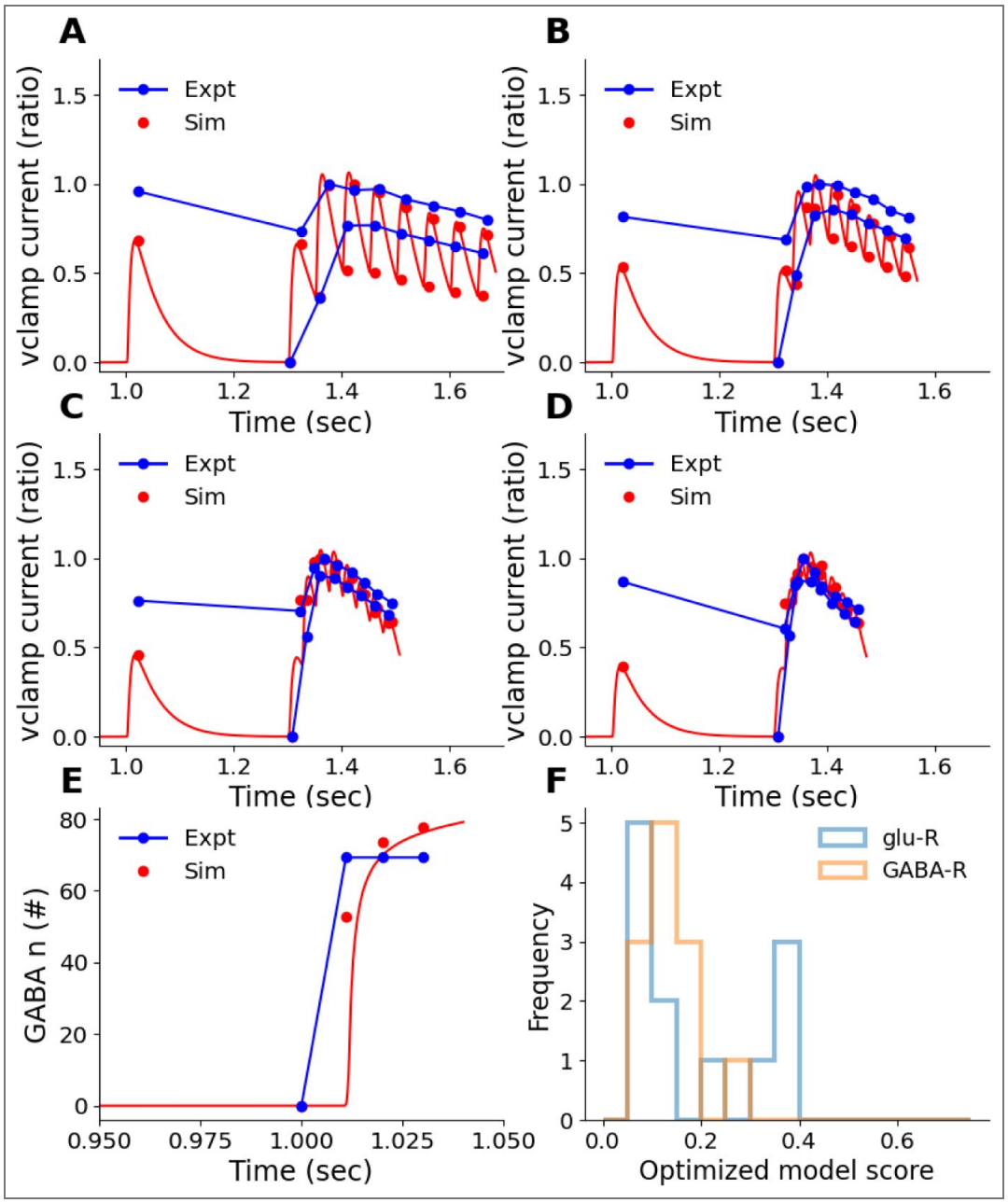

Figure 4-figure supplement 3. Example model fits for Inhibitory synapses on cell 7492. A, B, C, D: IPSC fits for 20, 30, 40, and 50 Hz, respectively. Blue traces are experimental peaks and valleys averaged over all repeats and all 15-square patterns for neuron 7492. Red traces are simulated IPSCs. Note that the experimental traces are noisy hence the fits miss some of the peaks. E: Cumulative release curve for GABA vesicles. Blue: target release complete within 10 ms. Red: simulated release. F: Distribution of model fitting scores for all cells and for glu and GABA receptors. Scores are normalized RMS differences between experimental and simulated points, as in panels A-D. Any score below 0.3 is a good fit.

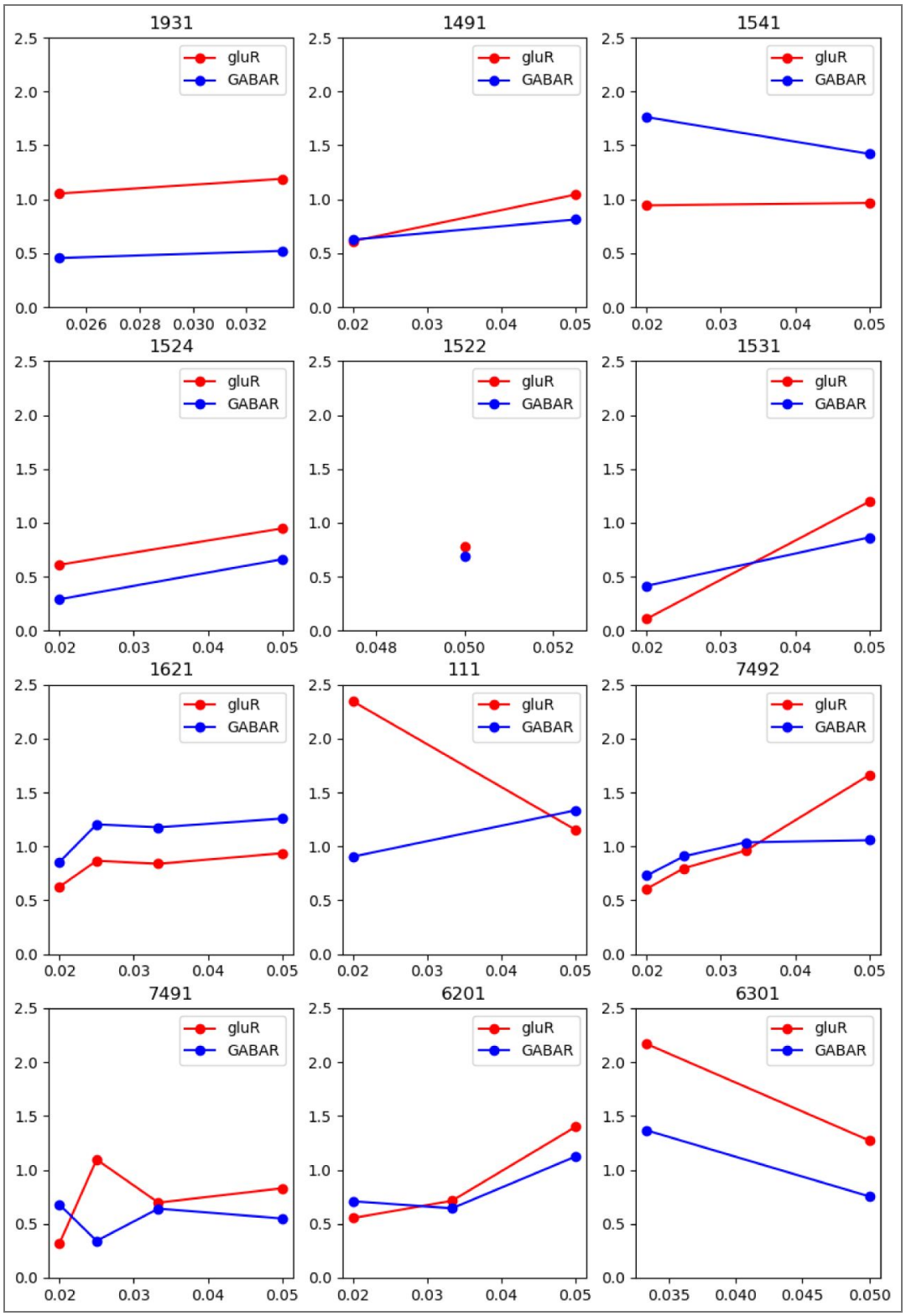

Figure 4-figure supplement 4. STP profiles for each of the 12 voltage-clamp recordings with the pulse-train stimulus. Some cells were not held long enough to complete all four frequencies.

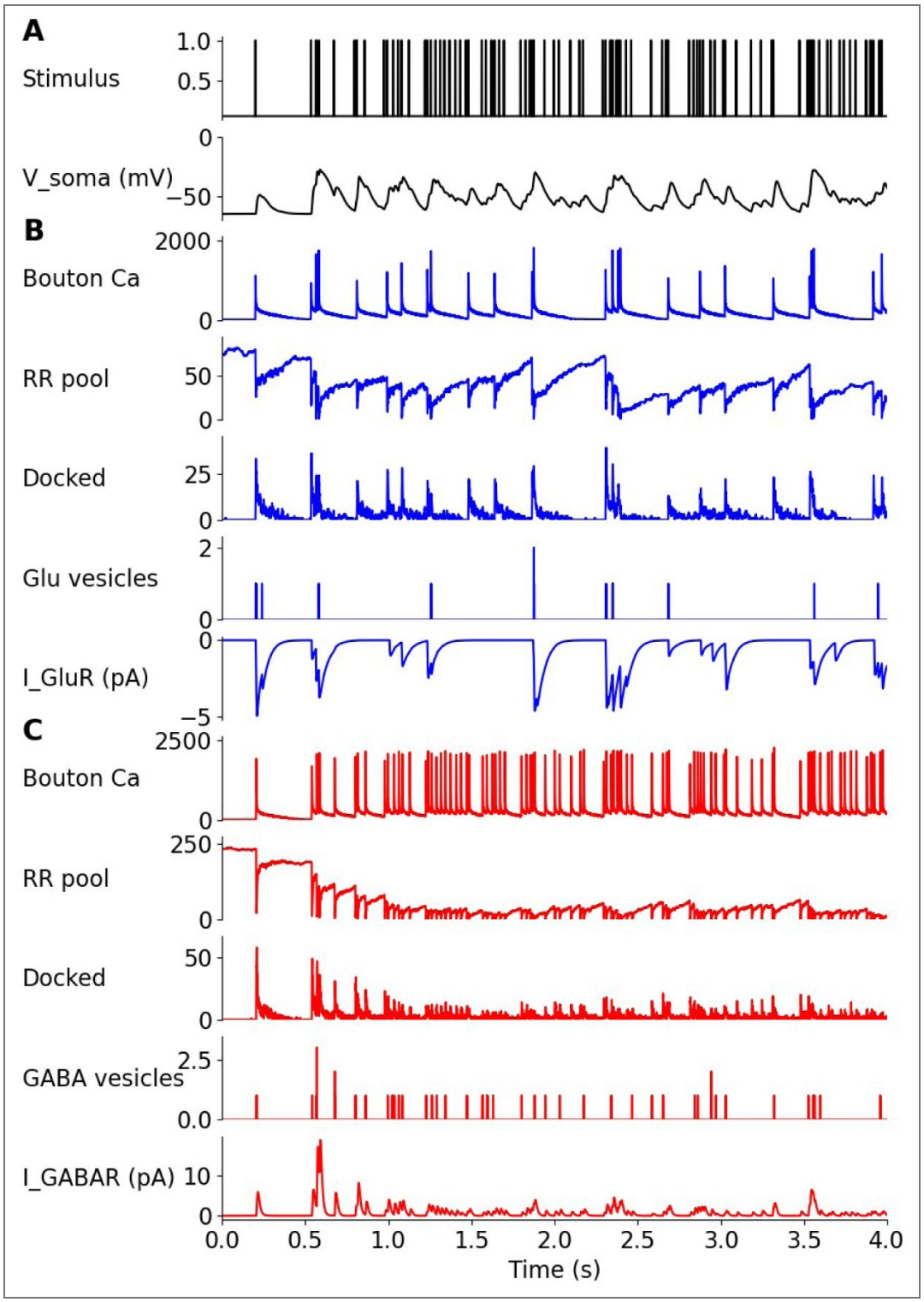

Figure 4-figure supplement 5. Presynaptic signalling model dynamics. All quantities are units of numbers of molecules per bouton unless otherwise stated. Signalling calculations are stochastic. Note that these are only two representative active synapses from among the 100 excitatory and 200 inhibitory synapses on the cell, and there are other synapses with distinct activity. Currents are reported as total currents for all synapses of the specified type. A: Optical stimulus train and corresponding somatic potential. B: Glutamaterigic bouton signalling. C. GABAergic bouton signalling.

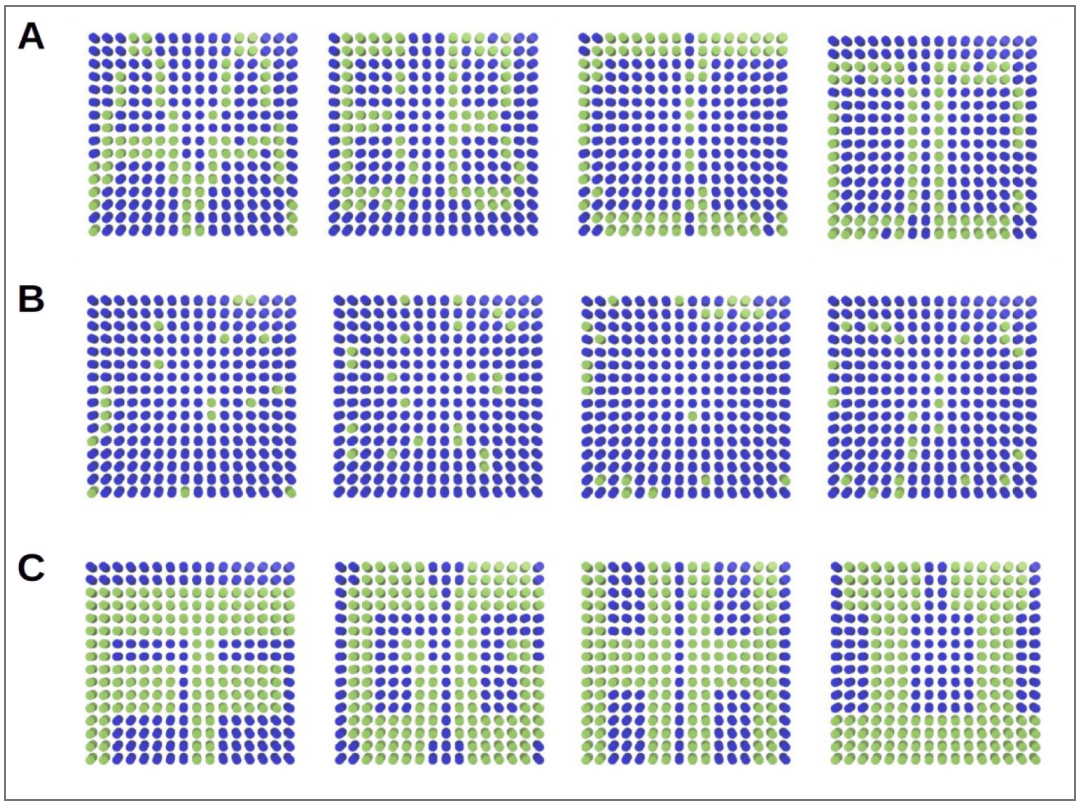

Figure 4-figure supplement 6. Stimulus patterns used in simulations to activate the CA3 layer. Green spots are on, blue are off. A: Dense patterns used as equivalents to 5-square experimental stimuli, with 12.5% of spots set to zero, resulting in 78±2 spots per pattern. Overlap between successive patterns is 31, 23, and 37 spots. B. Reference sparse patterns to map to 5 square stimuli, with 75% of spots set to zero, resulting in 21±3 spots per pattern. Overlap between successive patterns is 1,1, and 5 spots. C. Simulation implementation of 15-square patterns, with 144, 152, 152, and 160 spots per pattern. Overlap is 68, 80 and 88 spots..

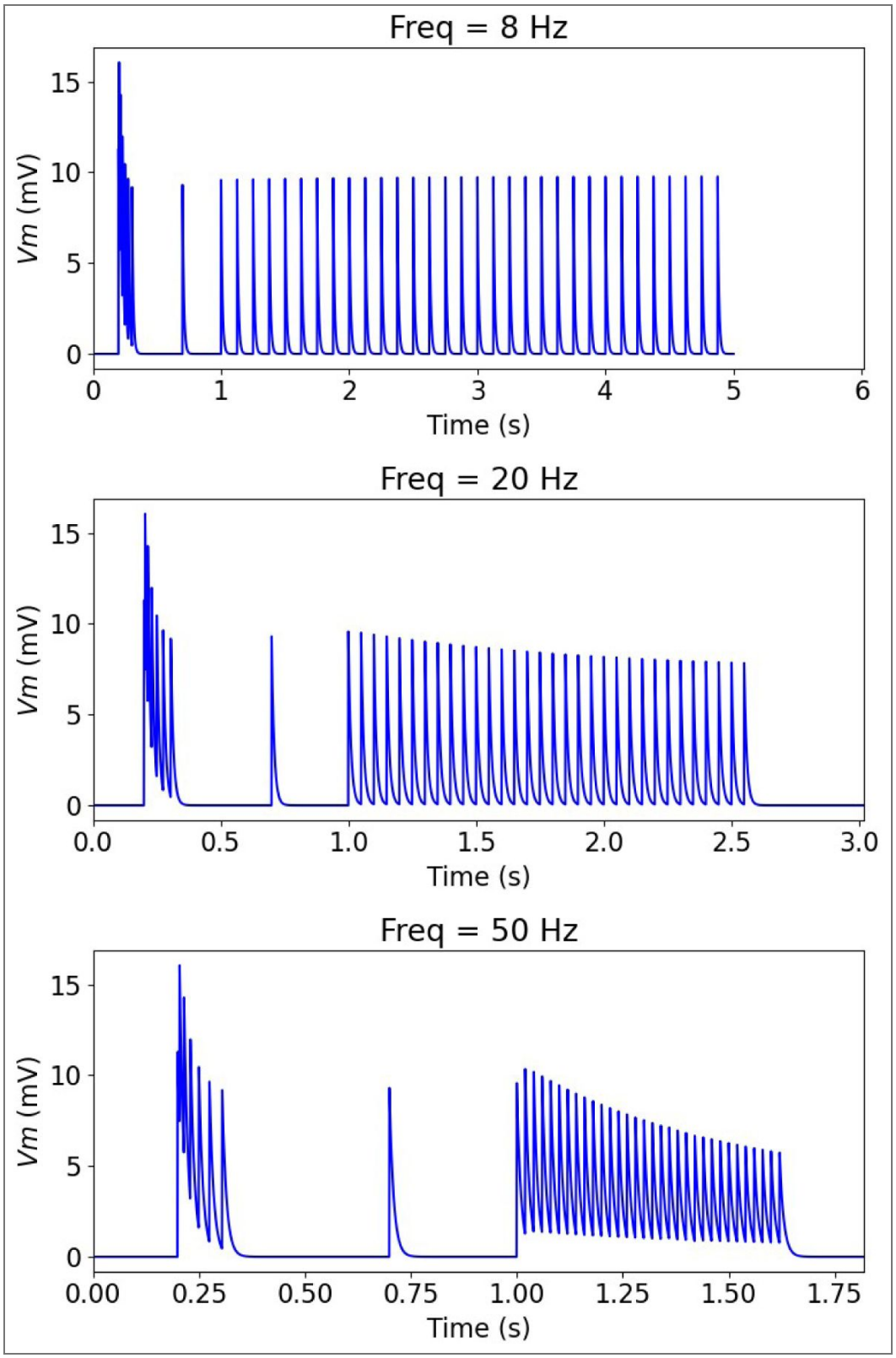

Figure 4-figure supplement 7. Time course of charging and desensitisation of optically stimulated CA3 neuron model. At 0.2 seconds we deliver a burst with inter-pulse intervals of 5, 10, 15, 20, 25, 30 ms. At t=0.7 seconds we deliver a single pulse. At t=1 seconds we deliver a train of 32 pulses at the frequencies of 8, 20 and 50 Hz as indicated above each panel.

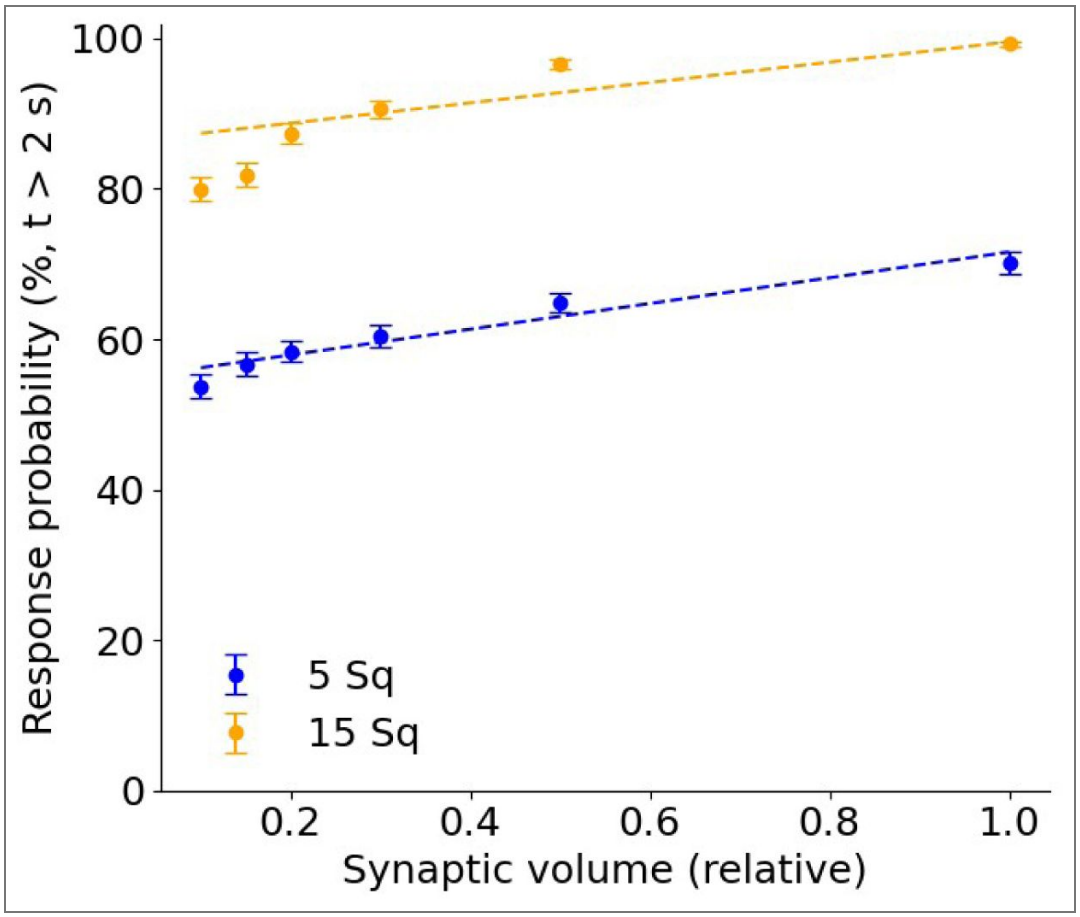

Figure 6-figure supplement 1. EPSP response probability rises with larger presynaptic volume. Reference volume used in simulations is scaled by 0.2, which corresponds to a synaptic volume of 0.0205±0.0008 femtolitres.

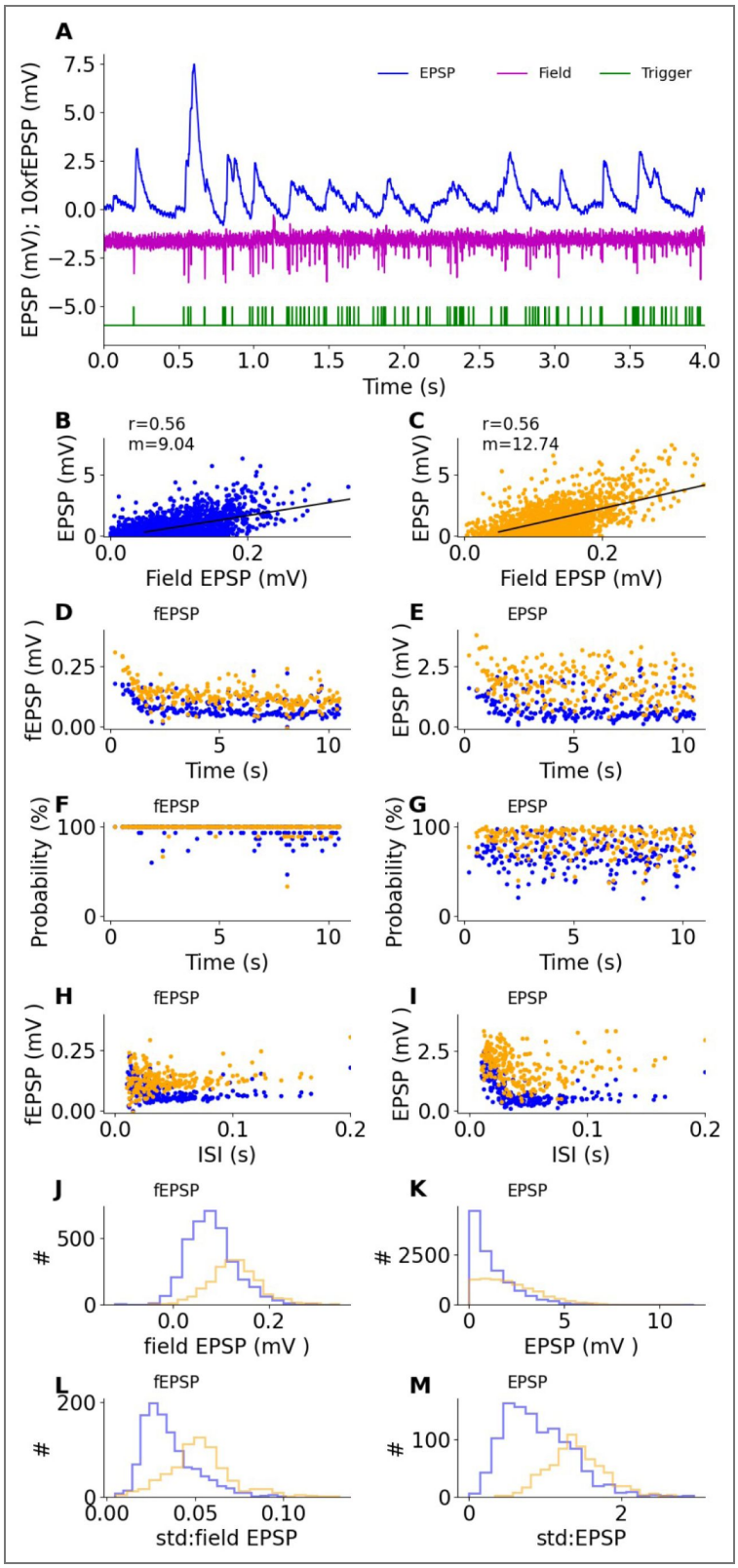

Figure 6-figure supplement 2. Response distributions for Poisson pulse train: field and EPSP data. A: Sample data. Blue: Raw EPSP data, maroon: field potentials, green: stimulus pulse trigger. B-M: 5 square pattern responses in blue, 15-square pattern responses in orange. B, C: Scatter plots of EPSP vs fEPSP for 5 and 15 square input, respectively. Linear regression fit is plotted in black. P-value < 0.001 in both cases. D: Field EPSP as a function of time. E: EPSP as a function of time. F. Probability that a pulse will elicit an fEPSP peak. This is almost 100% reliable. G. Probability that a pulse will elicit an EPSP. Note that the initial ~2 seconds of the train have fewer events of low probability. H: Field EPSP as a function of inter-stimulus interval (ISI) for the pair of stimuli

immediately preceding the fEPSP. I: EPSP as a function of ISI. Note that, unlike panel H, short ISIs elicit larger EPSPs. J: Distribution of field EPSP responses. K: Distribution of EPSP responses. This differs qualitatively from panel J, except that in both cases, the 15-square distributions are shifted over to the right. L: distribution of standard deviation in field EPSP for successive trials of each given pattern. M: Distribution of standard deviation in EPSP for successive trials for each pattern.

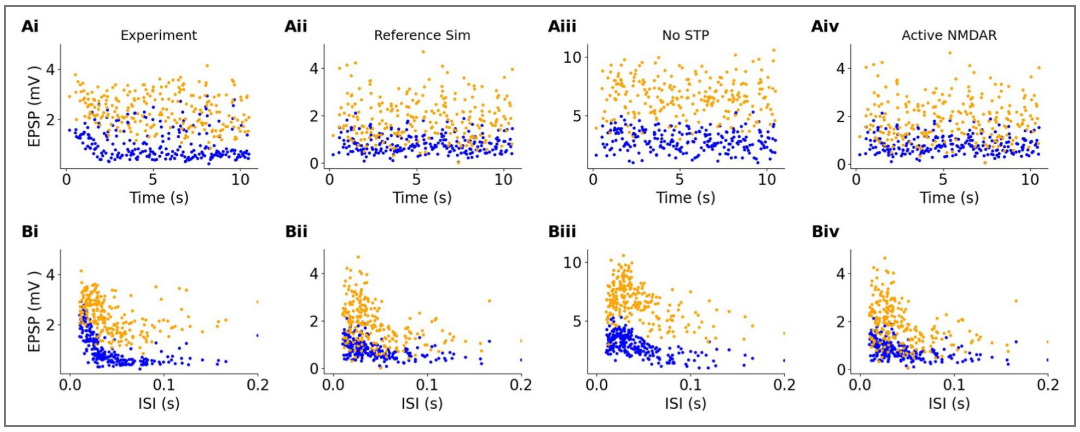

Figure 6-figure supplement 3. Contributions to EPSP decline with time and ISI. Yellow dots: 15 square stimuli, blue dots: 5 square stimuli. A: Contribution of STP to the initial dip in EPSPs. Ai: Experimental data. Note the decline in EPSP from t = 0 to t ~2 seconds. Aii. Reference simulated model has a similar dip in EPSP. Aiii. Simulated model with STP disabled. In this case the 5 square case has a dip in EPSP, but not the 15 square. Aiv: Incorporation of NMDAR activity has negligible effect because the potential is well below that for release of magnesium block. B: Contributions to the dependence of EPSP on ISI. Yellow dots: 15 square stimuli, blue dots: 5 square stimuli. Bi: Experiment. There is a sharp decline, tau_5Sq = 0.3 to 18ms, tau_15Sq=8ms to 1s. Bii: Reference model. Tau_5sq=34.3±6.94ms, Tau_15sq=49.7±12.5ms. Biii: Model without STP in either GluR or GABAR synapses. Tau_5sq=58.7±9.8ms, Tau_15sq=117±35ms. The ISI dependence remains, though the time-course is slower in the absence of STP. Note that the response amplitudes are larger in the absence of STP, suggesting that presynaptic depression reduces EPSP amplitudes in the reference but not non-STP model. Biv: Model without NMDA receptors. The response is very similar to the reference response, suggesting that most of the current is carried by the Glu receptors, and the NMDA receptor opening does not lead to amplification of EPSP at short ISIs.

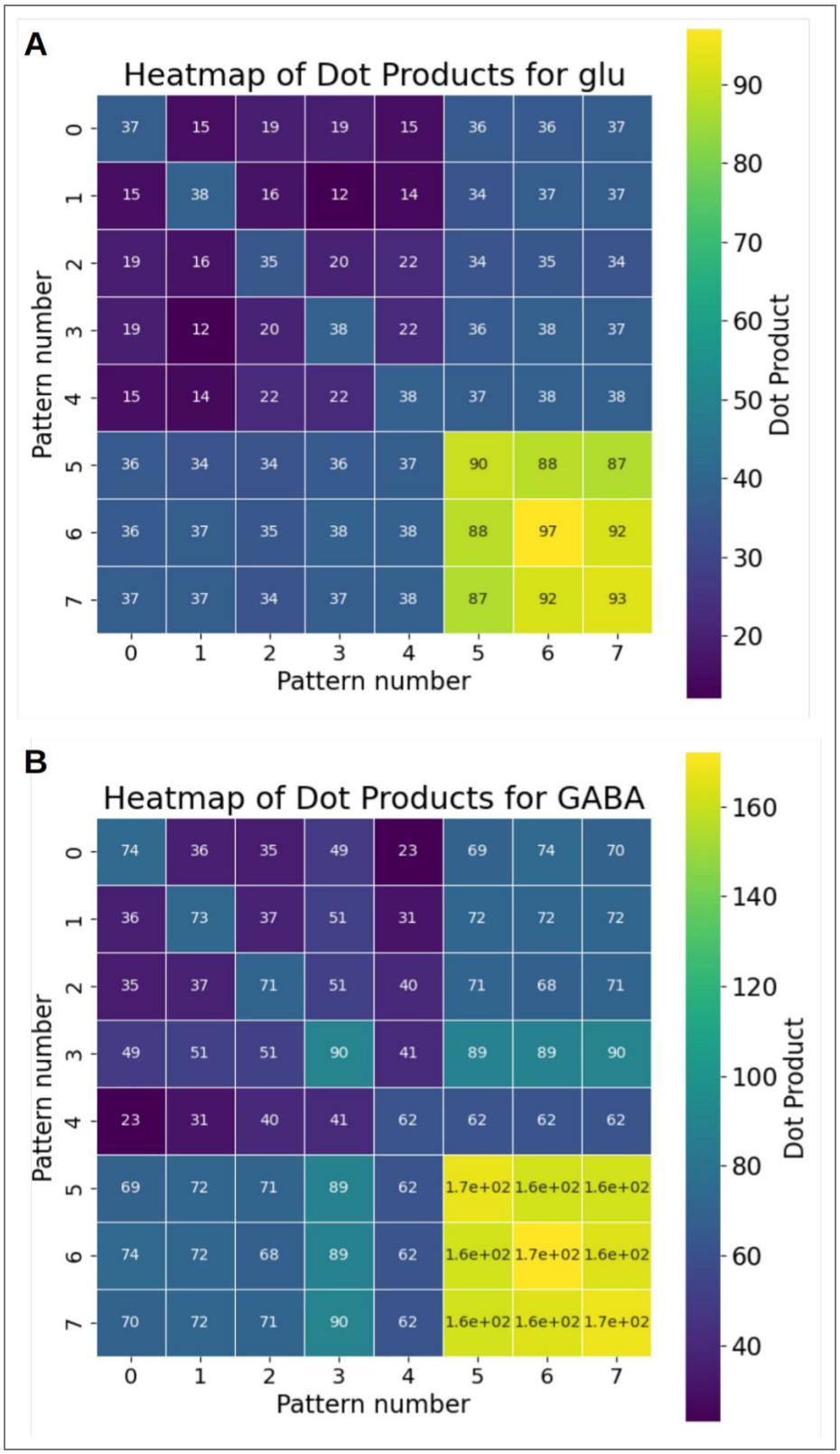

Figure 7-figure supplement 1. Overlap among synapses stimulated by each of 8 stimulus patterns. Patterns 0 through 4 are 5-square patterns, and patterns 5,6,7 are 15-square patterns. Diagonals indicate self-overlap, and are therefore the count of the number of stimulated synapses. A: Glutamatergic synapses. B: GABAergic synapses.

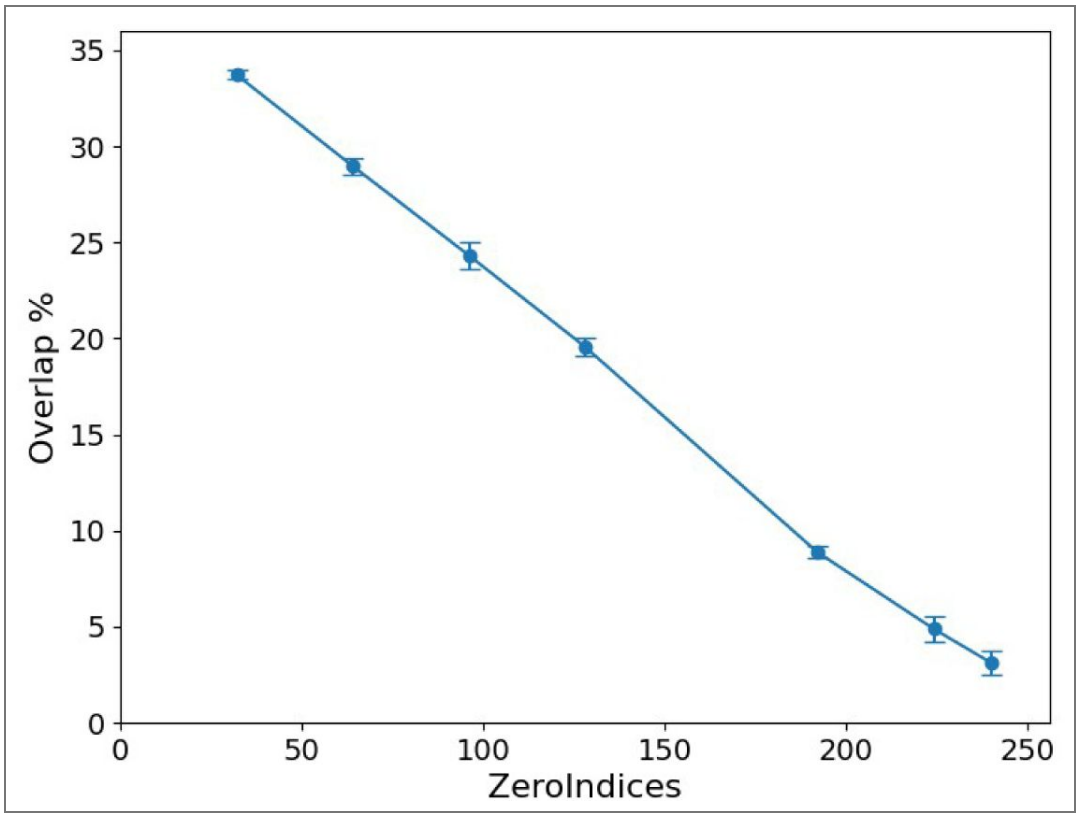

Figure 9-figure supplement 1. Overlap between CA1 synapses following 15 square pattern declines with the model construction parameter ZeroIndices. ZeroIndices is the number of CA3 inputs set to zero, out of a maximum of 256.

Data availability

Experimental data have been deposited in Zenodo at 10.5281/zenodo.20179470 Partial Simulation output data used in figures, are also in the Zenodo dataset. Simulation output generation scripts are provided on GitHub at *https://github.com/BhallaLab/STP_EI_paper_figs* Figure plotting scripts are provided on GitHub at *https://github.com/BhallaLab/STP_EI_paper_figs*

Additional information

Funding Information

AA and USB are at NCBS-TIFR which receives the support of the Department of Atomic Energy, Government of India, under Project Identification No. RTI 4006. The study received funding from SERB Grant CRG/2022/003135-G.

Author Contribution

Aditya Asopa: Conceptualization, Data curation, Analysis, Investigation, Visualization, Methodology, Writing original draft, Writing review and editing;

Upinder Singh Bhalla: Conceptualization, Resources, Simulation, Visualization, Analysis, Software, Supervision, Funding acquisition, Writing original draft and revision, Project administration, writing review and editing

Funding

Funder	Grant reference number	Author
DST | Science and Engineering Research Board (SERB)	CRG/2022/003135-G	Upinder Singh Bhalla
Department of Atomic Energy, Government of India (DAE)	RTI 4006	Upinder Singh Bhalla

Author ORCID iDs

Upinder Singh Bhalla: https://orcid.org/0000-0003-1722-5188

Additional files

Supplementary Methods: Model Parameters

References

1. **Agnes Everton J,** Luppi Andrea I, Vogels Tim P (2020) Complementary Inhibitory Weight Profiles Emerge from Plasticity and Allow Flexible Switching of Receptive Fields. *The Journal of Neuroscience* **40**:9634-49 https://doi.org/10.1523/JNEUROSCI.0276-20.2020 | PubMed
2. **Agnes Everton J,** Vogels Tim P (2024) Co-Dependent Excitatory and Inhibitory Plasticity Accounts for Quick, Stable and Long-Lasting Memories in Biological Networks. *Nature Neuroscience* **27**:964-74 https://doi.org/10.1038/s41593-024-01597-4 | PubMed
3. **Anwar Haroon,** Li Xinping, Bucher Dirk, Nadim Farzan (2017) Functional Roles of Short-Term Synaptic Plasticity with an Emphasis on Inhibition. *Current Opinion in Neurobiology* **43**:71-78 https://doi.org/10.1016/j.conb.2017.01.002 | PubMed
4. **Asopa Aditya,** Bhalla Upinder S (2023) A Computational View of Short-Term Plasticity and Its Implications for E-I Balance. *Current Opinion in Neurobiology* **81**:102729 https://doi.org/10.1016/j.conb.2023.102729 | PubMed
5. **Atallah Bassam V,** Scanziani Massimo (2009) Instantaneous Modulation of Gamma Oscillation Frequency by Balancing Excitation with Inhibition. *Neuron* **62**:566-77 https://doi.org/10.1016/j.neuron.2009.04.027 | PubMed
6. **Atasoy Deniz,** Aponte Yexica, Su Helen Hong, Sternson Scott M (2008) A FLEX Switch Targets Channelrhodopsin-2 to Multiple Cell Types for Imaging and Long-Range Circuit Mapping. *The Journal of Neuroscience* **28**:7025-30 https://doi.org/10.1523/JNEUROSCI.1954-08.2008 | PubMed
7. **Barros-Zulaica Natalí,** Rahmon John, Chindemi Giuseppe, et al. (2019) Estimating the Readily-Releasable Vesicle Pool Size at Synaptic Connections in the Neocortex. *Frontiers in Synaptic Neuroscience* **11**:29 https://doi.org/10.3389/fnsyn.2019.00029 | PubMed
8. **Bartley Aundrea F,** Dobrunz Lynn E (2015) Short-term Plasticity Regulates the Excitation/Inhibition Ratio and the Temporal Window for Spike Integration in CA 1 Pyramidal Cells. *European Journal of Neuroscience* **41**:1402-15 https://doi.org/10.1111/ejn.12898 | PubMed
9. **Bartley Aundrea F,** Lucas Elizabeth K, Brady Lillian J, et al. (2015) Interneuron Transcriptional Dysregulation Causes Frequency-Dependent Alterations in the Balance of Inhibition and Excitation in Hippocampus. *The Journal of Neuroscience, ahead of print* https://doi.org/10.1523/jneurosci.1834-15.2015 | PubMed
10. **Bezaire Marianne J,** Soltesz Ivan (2013) Quantitative Assessment of CA1 Local Circuits: Knowledge Base for Interneuron-Pyramidal Cell Connectivity: Quantitative Assessment Of Ca1 Local Circuits. *Hippocampus* **23**:751-85 https://doi.org/10.1002/hipo.22141 | PubMed
11. **Bhalla Upinder S** (2011) Multiscale Interactions between Chemical and Electric Signaling in LTP Induction, LTP Reversal and Dendritic Excitability. *Neural Networks* **24**:9 https://doi.org/10.1016/j.neunet.2011.05.001 | PubMed

12. **Bhalla Upinder S** (2017) Synaptic Input Sequence Discrimination on Behavioral Timescales Mediated by Reaction-Diffusion Chemistry in Dendrites. *eLife* **6**:April https://doi.org/10.7554/eLife.25827 | PubMed
13. **Bhatia Aanchal,** Moza Sahil, Bhalla Upinder S (2019) Precise Excitation-Inhibition Balance Controls Gain and Timing in the Hippocampus. *eLife* **8**:e43415 https://doi.org/10.7554/elife.43415 | PubMed
14. **Butler Robert A** (1968) Effect of Changes in Stimulus Frequency and Intensity on Habituation of the Human Vertex Potential. *The Journal of the Acoustical Society of America* **44**:945-50 https://doi.org/10.1121/1.1911233 | PubMed
15. **Chen Lu,** Li Xiling, Tjia Michelle, Thapliyal Shruti (2022) Homeostatic Plasticity and Excitation-Inhibition Balance: The Good, the Bad, and the Ugly. *Current Opinion in Neurobiology* **75**:102553 https://doi.org/10.1016/j.conb.2022.102553 | PubMed
16. **Chen Weiliang,** Carel Tristan, Awile Omar, et al. (2022) STEPS 4.0: Fast and Memory-Efficient Molecular Simulations of Neurons at the Nanoscale. *Frontiers in Neuroinformatics* **16**:883742 https://doi.org/10.3389/fninf.2022.883742 | PubMed
17. **Dainauskas Justinas J,** Marie Hélène, Migliore Michele, Saudargiene Ausra (2023) GluN2B-NMDAR Subunit Contribution on Synaptic Plasticity: A Phenomenological Model for CA3-CA1 Synapses. *Frontiers in Synaptic Neuroscience* **15**:1113957 https://doi.org/10.3389/fnsyn.2023.1113957 | PubMed
18. **Denève Sophie,** Machens Christian K (2016) Efficient Codes and Balanced Networks. *Nature Neuroscience* **19**:375-82 https://doi.org/10.1038/nn.4243 | PubMed
19. **Dorman Daniel B,** Blackwell Kim T (2022) Synaptic Plasticity Is Predicted by Spatiotemporal Firing Rate Patterns and Robust to In Vivo-like Variability. *Biomolecules* **12**:1402 https://doi.org/10.3390/biom12101402 | PubMed
20. **Eichenbaum H,** Kuperstein M, Fagan A, Nagode J (1987) Cue-Sampling and Goal-Approach Correlates of Hippocampal Unit Activity in Rats Performing an Odor-Discrimination Task. *The Journal of Neuroscience* **7**:716-32 https://doi.org/10.1523/JNEUROSCI.07-03-00716.1987 | PubMed
21. **Eichenbaum Howard,** Dudchenko Paul, Wood Emma, Shapiro Matthew, Tanila Heikki (1999) The Hippocampus, Memory, and Place Cells. *Neuron* **23**:209-26 https://doi.org/10.1016/S0896-6273(00)80773-4 | PubMed
22. **Eriksson Olivia,** Bhalla Upinder Singh, Blackwell Kim T, et al. (2022) Combining Hypothesis– and Data-Driven Neuroscience Modeling in FAIR Workflows. *eLife* **11**:e69013 https://doi.org/10.7554/eLife.69013 | PubMed
23. **Fortune Eric S,** Rose Gary J (2001) Short-Term Synaptic Plasticity as a Temporal Filter. *Trends in Neurosciences* **24**:381-85 https://doi.org/10.1016/S0166-2236(00)01835-X | PubMed
24. **Galarreta M,** Hestrin S (1998) Frequency-Dependent Synaptic Depression and the Balance of Excitation and Inhibition in the Neocortex. *Nature Neuroscience* **1**:587-94 https://doi.org/10.1038/2822 | PubMed
25. **Garrido Marta I,** Kilner James M, Stephan Klaas E, Friston Karl J (2009) The Mismatch Negativity: A Review of Underlying Mechanisms. *Clinical Neurophysiology* **120**:453-63 https://doi.org/10.1016/j.clinph.2008.11.029 | PubMed
26. **Gillespie Daniel T** (1977) Exact Stochastic Simulation of Coupled Chemical Reactions. *The Journal of Physical Chemistry* **81**:2340-61 https://doi.org/10.1021/j100540a008
27. **Goldman Mark S,** Nelson Sacha B, Abbott LF (1999) Decorrelation of Spike Trains by Synaptic Depression. *Neurocomputing* **26-27**:147-53 https://doi.org/10.1016/S0925-2312(99)00068-5
28. **Grion Natalia,** Akrami Athena, Zuo Yangfang, Stella Federico, Diamond Mathew E (2016) Coherence between Rat Sensorimotor System and Hippocampus Is Enhanced during Tactile Discrimination. *PLOS Biology* **14**:e1002384 https://doi.org/10.1371/journal.pbio.1002384 | PubMed
29. **Jia David W,** Vogels Tim P, Costa Rui Ponte (2022) Developmental Depression-to-Facilitation Shift Controls Excitation-Inhibition Balance. *Communications Biology* **5**:873 https://doi.org/10.1038/s42003-022-03801-2

30. **Joshi Abhilasha,** Denovellis Eric L, Mankili Abhijith, et al. (2023) Dynamic Synchronization between Hippocampal Representations and Stepping. *Nature* **617**:125-31 https://doi.org/10.1038/s41586-023-05928-6 | PubMed

31. **Kanamaru Takashi,** Hensch Takao K, Aihara Kazuyuki (2023) Maximal Memory Capacity Near the Edge of Chaos in Balanced Cortical E-I Networks. *Neural Computation* **35**:1430-62 https://doi.org/10.1162/neco_a_01596 | PubMed

32. **Klyachko Vitaly A,** Stevens Charles F (2006a) Excitatory and Feed-Forward Inhibitory Hippocampal Synapses Work Synergistically as an Adaptive Filter of Natural Spike Trains. *PLoS Biology* **4**:e207 https://doi.org/10.1371/journal.pbio.0040207 | PubMed

33. **Klyachko Vitaly A,** Stevens Charles F (2006b) Temperature-Dependent Shift of Balance among the Components of Short-Term Plasticity in Hippocampal Synapses. *The Journal of Neuroscience: The Official Journal of the Society for Neuroscience* **26**:6945-57 https://doi.org/10.1523/JNEUROSCI.1382-06.2006 | PubMed

34. **Kremkow Jens,** Aertsen Ad, Kumar Arvind (2010) Gating of Signal Propagation in Spiking Neural Networks by Balanced and Correlated Excitation and Inhibition. *The Journal of Neuroscience* **30**:15760-68 https://doi.org/10.1523/JNEUROSCI.3874-10.2010 | PubMed

35. **Lagzi Fereshteh,** Fairhall Adrienne L (2024) Emergence of Co-Tuning in Inhibitory Neurons as a Network Phenomenon Mediated by Randomness, Correlations, and Homeostatic Plasticity. *Science Advances* **10**:eadi4350 https://doi.org/10.1126/sciadv.adi4350 | PubMed

36. **Lisman John E,** Jensen Ole (2013) The Theta-Gamma Neural Code. *Neuron* **77**:1002-16 https://doi.org/10.1016/j.neuron.2013.03.007 | PubMed

37. **Liu Benjamin,** Buonomano Dean V (2024) Ex Vivo Cortical Circuits Learn to Predict and Spontaneously Replay Temporal Patterns. *bioRxiv* https://doi.org/10.1101/2024.05.30.596702

38. **Mackwood Owen,** Naumann Laura B, Sprekeler Henning (2021) Learning Excitatory-Inhibitory Neuronal Assemblies in Recurrent Networks. *eLife* **10** https://doi.org/10.7554/ELIFE.59715 | PubMed

39. **Marino Massimo,** Misuri Lorenza, Brogioli Doriano (2014) A New Open Source Software for the Calculation of the Liquid Junction Potential between Two Solutions According to the Stationary Nernst-Planck Equation. *arXiv* https://doi.org/10.48550/arXiv.1403.3640

40. **Markram Henry,** Muller Eilif, Ramaswamy Srikanth, et al. (2015) Reconstruction and Simulation of Neocortical Microcircuitry. *Cell* **163**:456-92 https://doi.org/10.1016/j.cell.2015.09.029 | PubMed

41. **Mattioni Michele,** Le Novère Nicolas (2013) Integration of Biochemical and Electrical Signaling-Multiscale Model of the Medium Spiny Neuron of the Striatum. *PLoS ONE* **8**:e66811 https://doi.org/10.1371/journal.pone.0066811 | PubMed

42. **Mauger John W** (2017) Physicochemical Properties of Buffers Used in Simulated Biological Fluids with Potential Application for In Vitro Dissolution Testing: A Mini-Review. *Dissolution Technologies* **24**:38-51 https://doi.org/10.14227/DT240317P38

43. **May Patrick JC,** Tiitinen Hannu (2010) Mismatch Negativity (MMN), the Deviance-Elicited Auditory Deflection, Explained. *Psychophysiology* **47**:66-122 https://doi.org/10.1111/j.1469-8986.2009.00856.x | PubMed

44. **Miehl Christoph,** Gjorgjieva Julijana (2022) Stability and Learning in Excitatory Synapses by Nonlinear Inhibitory Plasticity. *PLoS Computational Biology* **18** https://doi.org/10.1371/journal.pcbi.1010682 | PubMed

45. **Misselhorn Jonas,** Schwab Bettina C, Schneider Till R, Engel Andreas K (2019) Synchronization of Sensory Gamma Oscillations Promotes Multisensory Communication. *Eneuro* **6**:ENEURO.0101-19.2019 https://doi.org/10.1523/ENEURO.0101-19.2019 | PubMed

46. **Modi Mehrab N,** Dhawale Ashesh K, Bhalla Upinder S (2014) CA1 Cell Activity Sequences Emerge after Reorganization of Network Correlation Structure during Associative Learning. *eLife* **3**:e01982 https://doi.org/10.7554/eLife.01982 | PubMed

47. **Mojica Prieto Francisco Javier,** Millero Frank J (2002) The Values of pK1 + pK2 for the Dissociation of Carbonic Acid in Seawater. *Geochimica et Cosmochimica Acta* **66**:2529-40 https://doi.org/10.1016/S0016-7037(02)00855-4

48. **Moreno Edgard C,** Gregory Thomas M, Brown Walter E (1966) Solubility of CaHPO4 · 2H2O and Formation of Ion Pairs in the System Ca(OH)2-H3PO4 – H2O at 37.5 °C. *Journal of Research of the National Bureau of Standards. Section A, Physics and Chemistry* **70A**:545-52 https://doi.org/10.6028/jres.070A.047 | PubMed

49. **Näätänen Risto,** Jacobsen Thomas, Winkler István (2005) Memory-based or Afferent Processes in Mismatch Negativity (MMN): A Review of the Evidence. *Psychophysiology* **42**:25-32 https://doi.org/10.1111/j.1469-8986.2005.00256.x | PubMed

50. **Nadkarni Suhita,** Bartol Thomas M, Sejnowski Terrence J, Levine Herbert (2010) Modelling Vesicular Release at Hippocampal Synapses. *PLoS Computational Biology* **6**:e1000983 https://doi.org/10.1371/journal.pcbi.1000983 | PubMed

51. **Nadkarni Suhita,** Bartol Thomas M, Stevens Charles F, Sejnowski Terrence J, Levine Herbert (2012) Short-Term Plasticity Constrains Spatial Organization of a Hippocampal Presynaptic Terminal. *Proceedings of the National Academy of Sciences* **109**:14657-62 https://doi.org/10.1073/pnas.1211971109 | PubMed

52. **Neher Erwin** (2015) Merits and Limitations of Vesicle Pool Models in View of Heterogeneous Populations of Synaptic Vesicles. *Neuron* **87**:1131-42 https://doi.org/10.1016/j.neuron.2015.08.038 | PubMed

53. **Nelson Sacha B,** Turrigiano Gina G (2008) Strength through Diversity. *Neuron* **60**:3 https://doi.org/10.1016/j.neuron.2008.10.020 | PubMed

54. **Plummer L Niel,** Busenberg Eurybiades (1982) The Solubilities of Calcite, Aragonite and Vaterite in CO2-H2O Solutions between 0 and 90°C, and an Evaluation of the Aqueous Model for the System CaCO3-CO2-H2O. *Geochimica et Cosmochimica Acta* **46**:1011-40 https://doi.org/10.1016/0016-7037(82)90056-4

55. **Pouille F,** Scanziani M (2001) Enforcement of Temporal Fidelity in Pyramidal Cells by Somatic Feed-Forward Inhibition. *Science* **293**:1159-63 https://doi.org/10.1126/science.1060342 | PubMed

56. **Pouille Frédéric,** Marin-Burgin Antonia, Adesnik Hillel, Atallah Bassam V, Scanziani Massimo (2009) Input Normalization by Global Feedforward Inhibition Expands Cortical Dynamic Range. *Nature Neuroscience* **12**:1577-85 https://doi.org/10.1038/nn.2441 | PubMed

57. **Ray Subhasis,** Bhalla Upinder S (2008) PyMOOSE: Interoperable Scripting in Python for MOOSE. *Frontiers in Neuroinformatics* **2**:6 https://doi.org/10.3389/neuro.11.006.2008 | PubMed

58. **Regehr WG** (2012) Short-Term Presynaptic Plasticity. *Cold Spring Harbor Perspectives in Biology* **4**:a005702-a005702 https://doi.org/10.1101/cshperspect.a005702 | PubMed

59. **Rolls Edmund T,** Kesner Raymond P (2006) A Computational Theory of Hippocampal Function, and Empirical Tests of the Theory. *Progress in Neurobiology* **79**:1-48 https://doi.org/10.1016/j.pneurobio.2006.04.005 | PubMed

60. **Rotman Z,** Deng PY, Klyachko VA (2011) Short-Term Plasticity Optimizes Synaptic Information Transmission. *Journal of Neuroscience* **31**:14800-14809 https://doi.org/10.1523/JNEUROSCI.3231-11.2011 | PubMed

61. **Schneggenburger Ralf,** Meyer Alexander C, Neher Erwin (1999) Released Fraction and Total Size of a Pool of Immediately Available Transmitter Quanta at a Calyx Synapse. *Neuron* **23**:399-409 https://doi.org/10.1016/S0896-6273(00)80789-8 | PubMed

62. **Sheffield Mark EJ,** Adoff Michael D, Dombeck Daniel A (2017) Increased Prevalence of Calcium Transients across the Dendritic Arbor during Place Field Formation. *Neuron* **96**:2 https://doi.org/10.1016/j.neuron.2017.09.029 | PubMed

63. **Sheffield Mark Ej,** Dombeck Daniel A (2019) Dendritic Mechanisms of Hippocampal Place Field Formation. *Current Opinion in Neurobiology* **54**:1-11 https://doi.org/10.1016/j.conb.2018.07.004 | PubMed

64. **Somashekar Bhanu Priya,** Bhalla Upinder Singh (2024) Discriminating Neural Ensemble Patterns through Dendritic Computations in Randomly Connected Feedforward Networks. *eLife* **13**:RP100664 https://doi.org/10.7554/eLife.100664.1

65. **Sun Hua Yu,** Li Qin, Bartley Aundrea F, Dobrunz Lynn E (2018) Target-Cell-Specific Short-Term Plasticity Reduces the Excitatory Drive onto CA1 Interneurons Relative to Pyramidal Cells During Physiologically-Derived Spike Trains. *Neuroscience* **388**:430-47 https://doi.org/10.1016/j.neuroscience.2018.07.051 | PubMed

66. **Trapp Philip,** Echeveste Rodrigo, Gros Claudius (2018) E-I Balance Emerges Naturally from Continuous Hebbian Learning in Autonomous Neural Networks. *Scientific Reports* **8**:8939 https://doi.org/10.1038/s41598-018-27099-5 | PubMed

67. **Traub RD,** Wong RK, Miles R, Michelson H (1991) A Model of a CA3 Hippocampal Pyramidal Neuron Incorporating Voltage-Clamp Data on Intrinsic Conductances. *Journal of Neurophysiology* **66**:2 https://doi.org/10.1152/jn.1991.66.2.635

68. **Tsanov Marian,** Chah Ehsan, Reilly Richard, O'Mara Shane M (2014) Respiratory Cycle Entrainment of Septal Neurons Mediates the Fast Coupling of Sniffing Rate and Hippocampal Theta Rhythm. *European Journal of Neuroscience* **39**:957-74 https://doi.org/10.1111/ejn.12449 | PubMed

69. **Tsodyks Misha V,** Markram Henry (1997) The Neural Code between Neocortical Pyramidal Neurons Depends on Neurotransmitter Release Probability. *Proceedings of the National Academy of Sciences* **94**:719-23 https://doi.org/10.1073/pnas.94.2.719 | PubMed

70. **Van Vugt Marieke K,** Schulze-Bonhage Andreas, Litt Brian, Brandt Armin, Kahana Michael J (2010) Hippocampal Gamma Oscillations Increase with Memory Load. *The Journal of Neuroscience* **30**:2694-99 https://doi.org/10.1523/JNEUROSCI.0567-09.2010 | PubMed

71. **Viswan Nisha A,** HarshaRani Gubbi Vani, Stefan Melanie I, Bhalla Upinder S (2018) FindSim: A Framework for Integrating Neuronal Data and Signaling Models. *Frontiers in Neuroinformatics* **12**:38 https://doi.org/10.3389/fninf.2018.00038 | PubMed

72. **Viswan Nisha Ann,** Tribut Alexandre, Gasparyan Manvel, Radulescu Ovidiu, Bhalla Upinder S (2024) Mathematical Basis and Toolchain for Hierarchical Optimization of Biochemical Networks. *PLoS Computational Biology* **20**:e1012624 https://doi.org/10.1371/journal.pcbi.1012624 | PubMed

73. **Vogels TP,** Sprekeler H, Zenke F, Clopath C, Gerstner W (2011) Inhibitory Plasticity Balances Excitation and Inhibition in Sensory Pathways and Memory Networks. *Science* **334**:1569-73 https://doi.org/10.1126/science.1211095 | PubMed

74. **Vogels Tim P,** Abbott LF (2009) Gating Multiple Signals through Detailed Balance of Excitation and Inhibition in Spiking Networks. *Nature Neuroscience* **12**:483-91 https://doi.org/10.1038/nn.2276 | PubMed

75. **Vreeswijk C. van,** Sompolinsky H (1996) Chaos in Neuronal Networks with Balanced Excitatory and Inhibitory Activity. *Science* **274**:1724-26 https://doi.org/10.1126/science.274.5293.1724

76. **Wehr Michael,** Zador Anthony M (2003) Balanced Inhibition Underlies Tuning and Sharpens Spike Timing in Auditory Cortex. *Nature* **426**:442-46 https://doi.org/10.1038/nature02116 | PubMed

77. **Wen Wei,** Turrigiano Gina G (2024) Keeping Your Brain in Balance: Homeostatic Regulation of Network Function. *Annual Review of Neuroscience* **47**:41-61 https://doi.org/10.1146/annurev-neuro-092523-110001 | PubMed

78. **Wu Yue Kris,** Miehl Christoph, Gjorgjieva Julijana (2022) Regulation of Circuit Organization and Function through Inhibitory Synaptic Plasticity. *Trends in Neurosciences* **45**:884-98 https://doi.org/10.1016/j.tins.2022.10.006 | PubMed

79. **Wu Yue Kris,** Zenke Friedemann (2021) Nonlinear Transient Amplification in Recurrent Neural Networks with Short-Term Plasticity. *eLife* **10**:e71263 https://doi.org/10.7554/eLife.71263 | PubMed

80. **Yarden Tohar S,** Nelken Israel (2017) Stimulus-Specific Adaptation in a Recurrent Network Model of Primary Auditory Cortex. *PLOS Computational Biology* **13**:3 https://doi.org/10.1371/journal.pcbi.1005437 | PubMed

81. **Yuste Rafael,** Cossart Rosa, Yaksi Emre (2024) Neuronal Ensembles: Building Blocks of Neural Circuits. *Neuron* **112**:875-92 https://doi.org/10.1016/j.neuron.2023.12.008 | PubMed

82. **Zucker Robert S,** Regehr Wade G (2002) Short-Term Synaptic Plasticity. *Annual Review of Physiology* **64**:355-405 https://doi.org/10.1146/annurev.physiol.64.092501.114547 | PubMed

Asopa and Bhalla (2026) Asopa and Bhalla eLife 2026: Experiment data and Figure generation files. Zenodo. https://doi.org/10.5281/zenodo.20179470

Peer reviews

Reviewer #1 (Public review):

Summary:

This study uses optogenetics to activate CA3 while recordings from CA1 neurons and characterizing the excitation/inhibition (E/I) balance. They observe use-dependent alterations in the E/I balance as a result of STP and they develop a model to describe these observations. This is a very ambitious paper that deals with many issues using both experimental and modeling approaches.

Strengths:

This paper examines important principles regarding the manner in which synaptic circuitry and use-dependent synaptic plasticity can transform inputs and perform computations.

Weaknesses:

There are three issues that cause concern regarding the applicability of their slice recordings to physiological conditions and that make some aspects of their results difficult to interpret. First, they state that 2 mM added external calcium mimics calcium levels in CSF, but this is not the case. This will influence the plasticity they observe. Second, they indicate that there is a 2% decrease in activated fibers per stimulus and attribute this to ChR2 desensitization. Such use-dependent decreases in fiber activation are expected to build during their repetitive activation experiments and artifactually influence their results. Third, they do not know the responses of individual CA3 cells to stimulation. They do not know if each cell fires reliably during repetitive activation and whether each cell only fires once.

https://doi.org/10.7554/eLife.107708.2.sa2

Reviewer #3 (Public review):

Summary:

This work shows experimentally and computationally that single CA1 neurons can perform mismatch detection on patterned CA3 inputs and that STP and EI balance underlie this detection.

Strengths:

It has been known that STP can enhance the EPSP when the corresponding presynaptic input exhibits abrupt changes in firing rate. This work provides experimental evidence and further computational support for the hypothesis that the basic computation through STP is useful for detecting abrupt changes in the spatial pattern of synaptic inputs at the Schaffer collaterals. Further, their results indicate the novel view that mismatch detection is most

efficient when gamma-frequency bursting inputs exhibit mismatches between theta cycles. The authors included novel results in the revised manuscript to show that the effective frequency range of gamma oscillation is broad, including both slow and fast gamma bands.

In the initial submission, the dependence of mismatch detection performance on model parameters and experimental settings, such as pattern overlaps and other network parameters, was not sufficiently explored. In the revised manuscript, the authors extensively studied these points and summarized the novel results in Fig. 9. Furthermore, the authors clarified that jitters in input spikes can improve detection performance in some cases. These results show the robustness of their results against variations in external and internal conditions.

Weaknesses:

While this study shows an intriguing example of combined experimental and computational studies, some analytic results, for instance, regarding the complex contributions of jitters to detection performance, could have clarified the underlying mechanism deeper and further strengthened the manuscript.

https://doi.org/10.7554/eLife.107708.2.sa1

Author response:

The following is the authors' response to the original reviews.

We have made several major changes in response to the comments and we feel that the manuscript is considerably stronger. In brief: 1. We have added substantial content about homeostasis and EI balance to the introduction. 2. We have addressed concerns about physiological relevance by performing calculations to show that the free calcium in our solutions is well within the physiological range, by citing previous studies showing that short-term plasticity is consistent across 33-38 ℃, and by doing simulations scaled to physiological temperatures to show that the key computational effects are retained. 3. We have addressed concerns about readability by extensive text rewrites, reformatting most of the figures, and by splitting figures into smaller, more focussed ones. 4. We have organized over 20 statistical evaluations and comparisons between our model and experiments into a table. 5. We have carried out additional calculations to examine how the optimal frequency for mismatch detection depends on parameters, and to show that mismatch detection remains even in the presence of stimulus jitter. 6. We have stated more clearly how our proposed mechanism for mismatch detection is based on transient plasticity-mediated skewing of EI-balance, and have added a schematic for the last figure to show this.

> ***Public Reviews:***
>
> ***Reviewer #1 (Public review):***
>
> *Summary:*
>
> *This study uses optogenetics to activate CA3, while recording from CA1 neurons and characterizing the excitation/inhibition (E/I) balance. They observe use-dependent alterations in the E/I balance as a result of STP, and they develop a model to describe these observations. This is a very ambitious paper that deals with many issues using both experimental and modeling approaches.*
>
> *Strengths:*
>
> *This paper examines important principles regarding the manner in which synaptic circuitry and use-dependent synaptic plasticity can transform inputs and perform*

> *computations.*
>
> *Weaknesses:*
>
> *The use of selective ChR2 expression in CA3 cells is a good approach, but there are numerous issues that cause concern regarding the applicability of their slice recordings to physiological conditions and that make some aspects of their results difficult to interpret. Experiments are not performed under physiological conditions (high external calcium and low temperature), which makes the interpretation of their findings difficult.*

Calcium: We would like to reassure the reviewer that the free calcium levels in our solutions were at ~1.27 mM, well within the physiological range, since our aCSF solution used calcium buffers as well as CaCl2. We have added a section to the methods to show this calculation.

Temperature: Klyachko and Stevens (J. Neurosci 2006) show that the facilitation, augmentation and filtering properties of the CA3-CA1 network were consistent between 33 and 38 degrees C, thus spanning our conditions of ~33 degrees C. Additionally, we have performed simulations to show that the mismatch detection computations remain pronounced (or are even strengthened) when simulation rates for kinetics and channels are scaled to physiological temperatures. Using a Q10 of 2, the scaling term for kinetics is ~37% faster. The outcomes are presented in Figures 7 and 9. We now state these points at the start of the results section:

“Our bath solution had physiological levels of free ions including calcium (methods), and recordings were performed at 32-33 ℃ which has been shown in rats to yield similar short-term plasticity properties as at physiological temperatures (Klyachko and Stevens 2006b).”

We have added a new section to the discussion “Relevance to in-vivo computation” in which we enumerate the caveats but also the points of convergence between our study and physiological conditions, to strengthen the interpretability of our results.

> *In addition, the reliability of stimulating action potentials in CA3 pyramidal cells needs to be determined, particularly during high-frequency trains. If it is unreliable, there are alternative approaches that might prove to be superior, such as the use of somatically targeted ChR2.*

We acknowledge that somatically targeted ChR2 might have slightly improved the sparseness of stimuli, but even such localized expression could lead to unreliability if the position of the soma with respect to the illumination is such that the stimulus is near threshold. Instead, we have adopted a data-driven estimation of CA3 reliability. We reanalyzed our optically-triggered field potential readouts from CA3, to estimate their reliability individually and over trains (Figure 1).

“Notably, the distribution of field amplitudes was very tight (Figure 1E), more so than the corresponding EPSPs (Figure 1H). Together with previous work using a similar optical stimulus system [6] we interpret this to say that the spiking responses from CA3 neurons to optical stimuli were consistent from trial to trial. The field response showed a slight decrease over the course of the pulse train of approximately 2% per pulse (regression fit slope=0.02, r2=0.05). We attribute this to ChR2 desensitization.”

As a further bound to any functional outcomes of CA3 spiking (un)reliability, we point out that CA3-CA1 release probability is low (p~0.2). Any reduction in CA3 reliability is equivalent to reducing the probability of synaptic release, which is already treated as a stochastic process in our simulations. We were able to compare this to experiment as follows: We explicitly modeled the effect of different synaptic volumes as a surrogate for changing p_release in Figure 6-figure supplement 1, and mapped this to our data in Figure 6 D.

"Then we compared the probability that each optical stimulus would elicit an EPSP (Figure 6 D). As expected, 15-square patterns (yellow dots) frequently gave an EPSP (77.5±11.7%), while 5-square patterns failed about half the time (51.4±16%). The simulated runs matched this (Table 1). The probability of failure reduced with increasing volume of the simulated presynaptic boutons, because larger volumes experienced smaller chemical noise (stochasticity) in synaptic release (Figure 6-figure supplement 1). We note that for the purposes of eliciting a postsynaptic response, any unreliability in optical stimulus-triggered firing of the CA3 neuron folds into the probability term for stochastic synaptic release. By matching this metric to experiment, we fine-tuned the volume scaling term for the presynaptic boutons to 0.2"

> *In addition, a clearer, more detailed discussion of their model that distinguishes it from previous modeling studies would be helpful (and would make it seem less incremental).*

This is a good suggestion, as we regard our model as very substantially different from previous studies. We have incorporated this in the discussion as below:

"Our current model is distinct in that it is truly multiscale, closely constrained by experiment, yet runs on modest hardware. It incorporates the network, a conductance based model of a CA1 pyramidal neuron, and chemical kinetic models of a population of stochastic synapses on its dendrite.

Our network model is much reduced compared to models with exhaustive cellular and network-level detail44. Its simplicity enables extensive exploration of the network parameters and comparison with recorded activity under a series of well-controlled stimulus patterns (Figures 4-9)."

We also point out that our proposed mechanism for mismatch detection is an advance over previous ones:

"Leaving aside the obvious differences between auditory cortex and hippocampus, we frame our model as a transient differential tilt in EI balance (Figure 3, Figure 8A,B, Figure 10B), in distinction to the fresh-afferent model. This makes our model robust over a wide range of stimulus and network conditions (Figure 9), and has the functional implication that transient responses remain at about the same amplitude over a prolonged stimulus sequence (Figure 8B, Figure 10B), rather than declining."

> ***Reviewer #2 (Public review):***
>
> *Summary:*
>
> *The authors investigate EI balance in the CA3-CA1 projections, emphasizing synaptic depletion and the implied rebalancing of excitatory and inhibitory projections onto a single CA1 Pyramidal cell. They present physiological results with optical stimulation in CA3 and measuring various response features in CA1, showing signatures consistent with the adjustment of EI balance. In particular, the authors emphasize a transient effect where the neuron escapes from EI balance, which can be used for mismatch detection. They partially replicate these results in a computational model that looks at detailed properties of synaptic plasticity in CA1.*
>
> *Strengths:*

> *The authors provide compelling evidence that non-specific modulation of synaptic plasticity, combined with their differential effects on excitatory and inhibitory neurons, can be used by CA1 excitatory neurons to detect changes in the population activity of CA3 neurons. Indeed, they provide insight into the potential computational role of transient EI imbalance.*
>
> *Weaknesses:*
>
> *The authors observe that "little is known about how EI balance itself evolves dynamically due to activity-driven plasticity in sparsely active networks." This is an overstatement, or better an understatement, given the extensive literature on EI balance (e.g. Wen W, Turrigiano GG. Keeping Your Brain in Balance: Homeostatic Regulation of Network Function. Ann Rev Neurosci. 2024. https://doi.org/10.1146/annurev-neuro-092523-110001 PMID:38382543). This way of framing the question does a disservice to the field and fails to contextualize the current research properly.*

We agree that we could have presented this better. Our focus was on short-term (<1 second) EI balance changes, but our statement did not set this context clearly. We rewritten and expanded the introduction to place our work in context of the substantial previous work on plasticity and homeostasis in EI balance.

> *The evidence is incomplete because the authors do not show a specific relationship between synaptic change in CA1 and EI balance adjustment, i.e., the alternative could be that this is an unspecific effect unrelated to the specific regulation of EI balance and its functional role in the hippocampus and the cortex.*

We don't quite follow this point. We have devoted Figures 2 and 3 to showing a specific relationship between short-term plasticity on CA3->CA1 synapses, and EI balance. In Figure 2 we show how E and I responses evolve over a pulse train. In Figure 3 we explicitly show the plasticity in E and I synapses, and then map it onto EI balance. In Panel 3E to G all these points come together and we show how gamma (the measure of nonlinearity of summation) evolves over a series of pulses in parallel with plasticity in E and I. We have added some new data in Figure 7A, B to show how E and I contribute to mismatch detection.

> *Indeed, the paper drifts from addressing EI balance to elucidating the mismatch detection.*

We acknowledge that we did not sufficiently articulate the role of EI balance terms in our subsequent analysis of mismatch detection. We have added several figure panels (Figure 7A, B), added a summary schematic (Figure 10) and redone the text and discussion. With these changes we make the point that mismatch detection can be better framed as a transient shift in EI balance.

"we frame our model as a transient differential tilt in EI balance (Figure 3, Figure 8A,B, Figure 10B), in distinction to the fresh-afferent model. This makes our model robust over a wide range of stimulus and network conditions (Figure 9), and has the functional implication that transient responses remain at about the same amplitude over a prolonged stimulus sequence (Figure 8B, Figure 10B), rather than declining."

> *The second shortcoming is that they do not show that the stimulation of the CA3 neurons occurs in a physiologically realistic regime.*

We have responded to the concerns about calcium concentration and temperature above in the response to the first reviewer. From the text:

"Our bath solution had physiological levels of free ions including calcium (methods), and recordings were performed at 32-33 °C which has been shown in rats to yield similar

shortterm plasticity properties as at physiological temperatures (Klyachko and Stevens 2006b)."

In addition, there is a concern about the mapping between physiological activity and our stimuli. It is true that the patterned stimuli we delivered were artificial. We make the point that they are nevertheless a much closer map to sparse physiological patterns than conventionally obtained through Schaffer collateral volleys:

"We use optical patterned stimuli to stimulate a cross-section of CA3 neurons with a variety of distributed patterns, theta, and other frequency rhythms. These stimuli are sparser and more dispersed than Schaffer collateral electrical stimuli which tend to stimulate adjacent fibres and in most cases are very strong."

We have added a section to the discussion "Relevance to in-vivo computation" to more completely address these points.

> *Nor do they analyze what the impact will be of the excitatory transient in "mismatch detection", and CA1,*

We are unsure what the reviewer means by the excitatory transient. At the level of CA3, we observe a narrow optically triggered field response for each light pulse. At the level of CA1, we monitor the responses due to activation of E and I synapses, and are able to observe peaks for each of the light pulses. We have analyzed all these features in figures 1 through 3, and they are also explicitly included in the model. Based on the reviewer's comment we have further characterized the field responses in CA3:

"We observed a small amount of 'ringing' of the field response which we interpret as either CA3 spiking in a burst, or recurrent activation of the CA3 neurons (Figure 1 supplement 2). The ringing was down to ~5% within 8 ms, supporting our treatment of the optical input as a tightly time-delimited event, and setting a low bound to any contribution to patterns by recurrence."

> *When this would occur at the level of the whole population, i.e., the physiological impossibility of triggering uncontrolled chaotic excitatory responses.*

Again, we are unsure what population or chaotic responses the reviewer has in mind. As mentioned above we have further characterized the field readouts of population responses in CA3 and have established tight limits on recurrent activity (Figure 1-figure supplement 2). In case the reviewer is looking for the outcome at the entire CA1 network as a whole, our experiment figures 1GH,J,K,L show sharp, single peak CA1 neuronal responses.

> *In particular, when we consider CA3 as an attractor memory system, the range of deviations (mismatches) that a CA1 neuron can be exposed to and detect, given the model presented in this paper, might be below those generated due to CA3 pattern-completion dynamics.*

While this is an interesting question for further work, our study focuses on a tighter question, that of mismatch detection downstream of the CA3. As indicated above and in Figure 1figure supplement 2, our field and patch recordings show that under our stimulus conditions, the internal dynamics of the CA3 produce minimal delayed or recurrent signals. Thus, by design, the CA3 layer in our system acts as an almost pure input layer with minimal internal dynamics. In the discussion we address some of the possibilities that may arise from pattern computations in CA3 and other upstream areas:

"We speculate that upstream areas may encode higher order stimulus features such as gaps, duration, intensity, localization, and frequency steps into distinct input patterns. Our proposed EI-balance shift mechanism could be a common end-point for all of these. This

would transform quite complex mismatch detection tasks into a uniform computation of pattern change, generalizing the mechanism to stimuli which were previously considered to require a more complex network-level implementation"

> *In addition, the match between the model and the physiological results is not fully quantified, leaving it to the reader to make a leap of faith.*

While the original version had numerous points of comparison between physiology and model, we agree that the values were scattered. In this revision we have tabulated them and performed additional statistical comparisons between model and data for a total of over 20 comparisons for the cell electrophysiology and network readouts (Table 1). We have also organized the preceding chemical kinetic comparisons in the supplements to Figure 4. We regard our study as one of very few to undertake quantitative experimental comparisons over such a range of readouts, experiments, and scales.

> *In addition, the manuscript suffers from poor analysis and presentation. The work could be improved by putting more effort into translating results into insightful metrics.*

We acknowledge that the presentation needed improvement. We have performed a major rewrite and reorganized many of the figures. As mentioned above, we have tabulated numerous metrics (Table 1) and have characterized EI balance and its evolution due to plasticity in a pulse train (Figures 2 and 3). For higher-level metrics, the new figures now extensively explore how mismatch sensitivity depends on parameters, stimulus patterns, and repeat frequency (Figures 7, 8, 9). We have added a discussion section "Relevance to invivo computation"

> *Overall, the authors have not achieved their original aim to show that the observed phenomenon is relevant to computation in CA1 or the brain outside of a highly controlled in vitro setup and reductionist single cell model.*

We feel that with this revision we have more clearly shown that our measurements are relevant to in-vivo computation, both through improved clarity and additional analysis. We have added a section "Relevance to in-vivo computation" in the discussion which enumerates the steps we have taken to support the relevance of our study. In the revision we have also performed several modelling extrapolations which encompass in-vivo conditions, such as testing jitter and frequency range. In a broader sense, in vitro work by design, is meant to be highly controlled so as to be able to get at mechanisms, and in our study we have delivered a range of physiologically relevant stimulus combinations to bridge the gap.

> *The authors combine several techniques for in vitro whole-cell patch-clamp recordings with patterned optical stimulation of the CA3 network in the mouse hippocampus, which is consistent with the state-of-the-art.*
>
> *They introduce a metric of similarity between expected and observed response patterns, called gamma. The name is confusing given the wide use of the label gamma for oscillation frequencies above 20 Hz. Gamma is calculated as (E*O)/(E-O). This means that gamma approximates infinity as the difference goes to 0, to mention one of the problems. This metric is not interpretable, and it is not clear why the authors did not follow a standard approach, e.g., likelihood, correlation, or percent error.*

We acknowledge the potential for confusion, however we felt it would be more confusing to change nomenclature. The metric gamma is derived from previous published work (Bhatia et al, eLife 2019) describing nonlinearities in summation, which is cited. In that study and the current one, there was no instance in which gamma became unreasonably large. It is true that the term gamma is used for many concepts, but we feel that the contexts are so different between summation nonlinearity and oscillation frequencies that confusion is unlikely. We have taken care with the wording in the text to further disambiguate the usage.

> *The authors aim to replicate the physiological results with an "abstract model of the hippocampal FFEI network. In practice, this is a conductance-based model of a single CA1 neuron, including chemical kinetics-based multi-step neurotransmitter vesicle release. This is an abstraction from the FFEI network that the paper starts with.*

We stress that the full model was used for all simulations except synaptic chemistry parameter fitting. We have clarified this point in the text and discussion section. From the text following Figure 4:

“We used this full model, with optical stimulus, CA3, Interneurons, CA1 neuron, probabilistic connectivity, and presynaptic signaling chemistry, for all subsequent calculations in this study.”

The model has 256 integrate-and-fire CA3 neurons, 256 interneurons, plus 200 inhibitory and 100 excitatory synapses onto the CA1 neuron, in each of which we have distinct multistep transmitter release kinetics.

> *It raises the question whether this is the right level at which to model the computational impacts of EI imbalance on CA1 neurons. Given the highly reduced model they have elaborated, the generalization to the complete CA3-CA1 network that the authors suggest can be achieved in the discussion is overoptimistic. Network models of CA3 and C1 must be considered, together with afferents from the entorhinal cortex to accomplish this generalization.*

We hope we have clarified that we do indeed base all our calculations on the full FFEI model converging onto the CA1 neuron whose connectivity influences circuit function, and we feel that this is necessary and sufficient for our goals in this study.

While the role of the recurrent CA3 network and EC would be interesting topics for future work, the scope of our study is to model the computational impact of EI imbalance in the FFEI network of CA3-> CA1 on CA1 neurons.

> *The authors reveal a potentially interesting physiological feature of CA1 excitatory neurons under very specific stimulus conditions.*

We thank the reviewer for considering the work as interesting. We would like to clarify, however, that our stimulus conditions are actually multidimensional. Specifically, we have varied frequency, pattern, and number of inputs for burst stimuli, and we have also examined Poisson train inputs. In the model we have examined spiking responses, and theta modulated stimuli. In the revision we have also included jittered synaptic input, and obtained frequency dependence of the mismatch detection. To our knowledge this is among the more multidimensional stimulus-response and modeling studies on this system.

> *It could warrant follow-up studies to place EI imbalance in a physiologically realistic context.*
>
> ***Reviewer #3 (Public review):***
>
> *Summary:*
>
> *This work shows experimentally and computationally that single CA1 neurons can perform mismatch detection on patterned CA3 inputs and that STP and EI balance underlie this detection.*
>
> *Strengths:*
>
> *It has been known that STP can enhance the EPSP when the corresponding presynaptic input exhibits abrupt changes in firing rate. This work provides experimental evidence*

> *and further computational support for the hypothesis that the basic computation through STP is useful for detecting abrupt changes in the spatial pattern of synaptic inputs at the Schaffer collaterals. Further, their results indicate the novel view that mismatch detection is most efficient when gamma-frequency bursting inputs exhibit mismatches between theta cycles.*
>
> *Weaknesses:*
>
> *Their model assumes that patterned activities in CA3 do not have overlaps. However, overlaps between memory engrams have been shown. Therefore, this assumption may not hold, and whether the proposed mechanism is valid for overlapping CA3 inputs needs further clarification.*

We see that our account of the methods needs clarification, since we explicitly incorporate overlap in our model. First, from the experiments themselves, we say that we expect overlap:

"This was also consistent with the observation of a wide field of excitability around individual CA3 neurons [6] (Figure 1-figure supplement 1). From this we expect that there is some overlap in the sets of CA3 neurons activated by different patterns, and this overlap increases with more stimulus squares."

In the model, we systematically examine the effect of overlap and have added several figures to make the point (Figure 9 Bi, Figure 9Ci, Figure 4-figure supplement 6, Figure 7figure supplement 1, Figure 9-figure supplement 1).

> ***Recommendations for the authors:***
>
> ***Reviewer #1 (Recommendations for the authors):***
>
> *The use of selective ChR2 expression in CA3 cells is a good approach, but there are numerous issues that cause concern regarding the applicability of the slice recordings to physiological conditions and that make some aspects of the results difficult to interpret.*
>
> *Weaknesses:*
>
> *(1) Some aspects of this study seem somewhat incremental. There is a rich literature on the study of excitation and inhibitory synapses and the issue of EI balance. There are a great many related studies that are not cited (off the top of my head: Pouille and Scanziani 2001, Mittmann, Chadderton and Hausser 2004, Atallah and Scanziani 2009, but there are many, many more). A great many of the ideas presented in this study have already been published previously (Klyachko and Stevens, 2006, and numerous other related manuscripts).*

We agree that the topic of EI balance has a very substantial literature. We have incorporated many of the mentioned articles and others in our introduction and discussion. Our study explicitly links several strands of work on EI balance with short-term plasticity and spatial patterning:

"The current study integrates several research themes of EI balance, short-term plasticity, and network computation to systematically characterize and model the properties of a network with feedforward inhibition. We complete the experiment-model-prediction-testing loop and show that differential changes on E and I synapses may provide a mechanism for single neurons to extract interesting features of spatiotemporal inputs through STP (Asopa and Bhalla 2023), while keeping mean activity steady."

We find that our sparse optical stimulation protocol gives qualitatively distinct results, and is amenable to investigation of more complex spatial pattern dependent effects. We have

explicitly discussed the mentioned paper by Klyachko and Stevens, and numerous others, to point out where our study differs. From the discussion:

"For example, studies using field electrode stimulation of the Shaffer collaterals report a sustained shift to excitation during burst input (Klyachko and Stevens 2006a). In contrast, our sparse optical patterned stimuli results in a small window of escape from EI balance around pulse 2 or 3 in a burst (Figure 3), following which both E and I undergo depression to restore balance (Figure 3, 8). Thus, spatial patterning intersects with short-term plasticity to add another layer of timing control through gating of E-I balance."

> *(2) There are multiple technical issues that call into question the relevance of this study for physiological conditions and the study of STP.*
>
> *(a) Their experiments were performed in elevated external calcium (2 mM) compared to physiological calcium (1.1-1.5 mM). This will have a major influence on the probability of release and short-term plasticity.*

This concern does not take into account the composition of our solution, which incorporated calcium buffers to give free calcium levels of ~1.27 mM. We have provided detailed calculations in the methods section.

"Our bath solution had physiological levels of free ions including calcium (methods), and recordings were performed at 32-33 °C which has been shown in rats to yield similar short-term plasticity properties as at physiological temperatures (Klyachko and Stevens 2006b)."

> *(b) Their experiments were performed at reduced temperatures (32-33 {degree sign}C). This is alright for many studies, but this is an important deficiency for the particular issue of EI balance and STP, and the relevance of conclusions based on these conditions.*

Klyachko and Stevens (J. Neurosci 2006) show that the facilitation, augmentation and filtering properties of the CA3-CA1 network were consistent between 33 and 38 degrees C, thus spanning our conditions of ~33 degrees C. Additionally, we have performed simulations to show that the mismatch detection computations remain pronounced (or are even strengthened) when simulation rates for kinetics and channels are scaled to physiological temperatures. Using a Q10 of 2, the scaling term for kinetics is ~37% faster. The outcomes are presented in Figures 7 and 9.

> *(c) I like the selective expression of ChR2 in CA3 pyramidal cells, but they have not provided any information on the effect of stimulation on the firing of CA3 cells (Extended Data Figure 1 is not enough). Is it reliable for single stimuli or stochastic?*

We have used field recordings in the CA3 to put tight bounds on the properties of CA3 firing (Figure 1, Figure 1-figure supplementar 2.) The field recordings show that on average the firing is highly reliable. We explicitly characterize the probability of eliciting EPSPs through Poisson patterned stimuli in Figure 6 D. As discussed in the text (excerpted below) any stochasticity in firing folds into the parameters for p_release, and synaptic firing is itself stochastic.

We note that for the purposes of eliciting a postsynaptic response, any unreliability in optical stimulus-triggered firing of the CA3 neuron folds into the probability term for stochastic synaptic release.

> *Do CA3 cells fire once or multiple times?*

This was a useful point, and we examined our field potential data more closely based on this.

"We observed a small amount of 'ringing' of the field response which we interpret as either CA3 spiking in a burst, or recurrent activation of the CA3 neurons (Figure 1-figure

supplement 2). The ringing was down to ~5% by the third peak which occurred within 8 ms, supporting our treatment of the optical input as a single brief event, and setting a low bound to any contribution to patterns by recurrence."

> *Are the spikes precisely timed, or do they vary?*

Based on the field potentials, the spikes are precisely timed (Figure 1-figure supplement 2D, E).

"fEPSP Peak Width distribution centred around 1.2 ms, but no peak was wider than 1.6 ms, suggesting tight synchrony in case multiple CA3 neurons were spiking."

> *Are there use-dependent changes in the ability of optogenetic stimulation to evoke spiking?*

Yes, and this is characterized in figure 1 panel I. The decrement is about 2% per pulse.

> *The CA3 regions are highly interconnected with recurrent collaterals. Does stimulation during trains alter the activity in the CA3 region as a result of these collaterals?*

Based on the CA3 field recordings, almost all CA3 activity is optically triggered (Figure 1figure supplement 2). Figure 1C shows narrow fEPSPs in a burst.

This would be a particularly important issue during trains. Would they have gotten more readily interpretable results if they had used a somatically targeted ChR2 variant?

We feel it is unlikely that a somatically targeted ChR2 would change outcomes. All our analysis assumes overlap of excitation of CA3 pyramidal neurons, that is, a given spot illuminates multiple cells to different degrees, and that there will be neurons which are activated by more than one spot. Somatic targeting does not eliminate activation due to scattering and out-of-focal-plane illumination.

> *In extended Figure 5, they show stimulus patterns used to stimulate. I need some more explanation. Are they stimulating in the cell body region only, or are they stimulating in the vicinity of dendrites?*

Extended Figure 5 (now Figure 4-figure supplement 6) indicates the stimulus patterns in the model. The experimental illumination pattern was 336μm x 187.2μm oriented so that the long axis of the pattern lay along the CA3 cell body layer (methods). Sample stimulus patterns are illustrated in Figure 1 panels D, G and J. Given scatter and out-of-plane illumination we expect that dendrites will also be stimulated. This is corroborated in Figure 1figure supplement 1 where we find that in addition to a strong 'receptive field' at the soma, there is a dispersed region of weaker activation. We cannot say definitively whether this dispersed region is due to light scatter, out-of-plane illumination, or dendritic activation. However, even somatically targeted ChR2 would elicit multi-neuron activity due to scatter and out-of-plane soma activation.

> *If that is the case, there are a great many complications that arise, and it seems to be an approach that could unreliably activate a great many CA3 cells.*

We have now put in a paragraph to discuss this, and to set bounds to the unreliability.

"To monitor the strength and consistency of the total resultant optogenetic activation of the CA3 layer, we used an extracellular field electrode in the CA3 stratum radiatum (Figure 1A, methods). The field response correlated well with optically-driven CA1 PC depolarization (Figure 1E-G), and scaled with the size of the pattern (Figure 1F). This was also consistent with the observation of a wide field of excitability around individual CA3 neurons (Bhatia et al. 2019) (Figure 1-figure supplement 1). From this we expect that there is some overlap in the

sets of CA3 neurons activated by different patterns, and this overlap increases with more stimulus squares. Notably, the distribution of field amplitudes was very tight (Figure 1E), more so than the corresponding EPSPs (Figure 1H). Together with previous work using a similar optical stimulus system (Bhatia et al. 2019) we interpret this to say that the spiking responses from CA3 neurons to optical stimuli were consistent from trial to trial."

We also note that any CA3 firing unreliability folds into the stochastic release terms, as discussed in an earlier point.

> *(d) As far as I can tell, they did not examine the effects of blocking NMDA receptors in their slice experiments. This seems like a very important experiment to perform if they really want to understand EI balance.*

The reviewer is correct that we did not block NMDA receptors. While this would have teased apart contributions of NMDAR and AMPAR to the overall response, our analysis of EI balance required the intact synapse and hence this decomposition (which has been done in previous studies) was not needed for our analysis.

> *Based on a-d it is not clear that their conclusions regarding EI balance and STP are relevant under physiological conditions, and their findings are difficult to interpret.*

We have addressed the concerns about physiological conditions when it comes to the Ca2+ levels and temperature. We do not feel that points c and d alter the interpretation of our findings.

> *Minor:*
>
> *(3) Their model has only 1 type of interneuron, whereas there are many. CA3-interneuron synapse has very different plasticity for different types of interneurons, and different types of interneuron synapses onto different parts of the CA3 cell. They need to justify lumping all of these types of interneurons.*

We agree that our model had a coarse-grained representation of interneurons as a single class. We feel this is an appropriate level of detail because it fits well for our experiments, and keeps the model tractable.

"We have, of course, simplified the network, most notably in the use of only one inhibitory interneuron class which maps to parvalbumin-positive fast-spiking interneurons with perisomatic connectivity. This level of detail was chosen as it was able to quantitatively fit a large number of observations with minimal circuit complexity."

> *(4) How many parameters can they adjust in their model? It seems that with so many parameters, their model is not very good at times (extended Figure 3B and E, for example).*

Our model has 6 free parameters for the network (Table 1), and another 7 parameters each for the E and I presynaptic plasticity models (Figure 4A and Supplementary Data). The presynapse plasticity parameters are directly assigned from the burst response recordings using the parameter fitting as described in the Methods. Normalized RMS differences between model and experiment for presynapse parameters are presented in Figure 4-figure supplements 1-3, panel F. Most traces lie below 0.3, which is a good fit. We have now tabulated numerous comparisons between model and experiment (Table 1). In all but 1 of 20 tests, the model value lies within the experimental range.

"Overall, we were able to quantitatively replicate almost all features of the experimental dataset in our multiscale model incorporating presynaptic signalling, postsynaptic electrophysiology, and abstracted network connectivity and responses. Between the datasets

in Figure 4-figure supplements 1 to 3, Figure 5, and Figure 6, we were able to substantially constrain the parameters in our model, from chemical to cellular physiology to network."

Additionally, we have included a new Figure 9 to systematically do parameter sweeps. From this we conclude:

"...mismatch detection in our model is robustly present and can be tuned over a wide range of network parameters and model assumptions, with the notable exception that it is absolutely dependent on the presence of STP."

> *(5) They use the term short-term potentiation (STP), but plasticity is not just enhancement; there is also depression. That is why many others opt for the more inclusive "short-term plasticity".*

We agree that this was unclear. We meant to use "Short Term Plasticity" and have now clarified this in the text.

> ***Reviewer #2 (Recommendations for the authors):***
>
> *The paper is poorly written and would benefit from a more careful preparation of the manuscript. In the opinion of this reviewer, it does not meet the expected quality for a paper of this type. Reviewing the paper was somewhat frustrating, requiring puzzling through details that were not well described. Also, failing to put clear labels on figures and their low quality did not help.*

We have worked substantially on the readability in the revision. We have made numerous changes to the text and figure legends, and have reworked several figures, with the goal of addressing concerns about readability.

> *The introduction lacks proper context for EI balance and the hippocampus.*

We have substantially rewritten the introduction to more clearly place our work in the context of the relevant literature. We touch upon short-term plasticity and computation, on homeostasis, on EI balance and on network correlates of plasticity such as mismatch detection.

> *The data analysis is superficial, and insufficient effort is put into compressing complex data into insightful metrics.*

We have done substantial rewrites to address this concern. There are two kinds of metrics we have developed for this study: those that measure the goodness of fit between simulations and data (consolidated into Figure 4-figure supplements 1 to 3 and in Table 1), and those which capture high-level features such as sublinearity of summation due to EI balance (Figure 3), selectivity for mismatch detection (Figures 7 to 9), and peak frequency for mismatch selectivity (Figure 9). We have also performed additional simulations as per reviewer suggestions, which give metrics for dependence of transition detection on network parameters, and for sensitivity of mismatch detection to input spike jitter.

> *The only attempt to do this was the gamma measure, which left one wanting (see above).*

We have responded to the points about the gamma measure above.

> *Figures are low-quality, labels are missing,*

We have substantially reworked figures, their labels, and legends. The automated mapping from our high-resolution figures to PDF seems to have blurred many of the figures, however, links to the originals should be there in the revision.

> *And the analysis stays too close to the data without presenting a clear quantitative synthesis and insight.*

Please see response above. We have tried to balance the process of characterizing numerous readouts and making a model that closely matches experiment, with the high-level insights by way of computational outcomes such as mismatch detection in a variety of more physiological contexts (pulse trains and theta patterned inputs, Figures 7 to 9).

> *Key results and mapping between physiology and the model are kept subjective and not quantified.*

Please see response above. We have consolidated our comparisons between physiology and experiments into Figure 4-figure supplements 1 to 3 and Table 1.

> *In addition, the similarity measure gamma, which is introduced to express the relationship or the modulation of the response, is mathematically naïve and not well-motivated. It will approach infinity when expected and actual values become more and more similar. While this might be the range where sensitivity is required.*

Please see response above. The metric gamma is derived from previous published work (Bhatia et al, eLife 2019) describing nonlinearities in summation, which is cited. In that study and the current one, there was no instance in which gamma became unreasonably large. It is true that the term gamma is used for many concepts, but we feel that the contexts are so different between summation nonlinearity and oscillation frequencies that confusion is unlikely. We have taken care with the wording in the text to further disambiguate the usage.

> *Some detailed observations:*
>
> *P2: What is an "interesting" feature?*

We have replaced the word “interesting” with “salient”:

“We complete the experiment-model-prediction-testing loop and show that differential changes on E and I synapses may provide a mechanism for single neurons to extract salient features of spatiotemporal inputs through STP (Asopa and Bhalla 2023), while keeping mean activity steady.”

> *P6 L110: However, over the pulse train, E and I underwent distinct STP profiles (Figure 1 M).*
>
> *What makes them distinct?*

This panel is now removed. A clearer account is presented in Figure 2D,E and F:

“The EPSC showed a trend of early potentiation followed by depression (Figure 2D, 2E), while the inhibition underwent depression from the start (Figure 2 D, Fi)”

> *P6 L115: Why can recurrent excitation in the CA3 segment be excluded?*

We thank the reviewer for pointing us to a more detailed analysis, which is now presented in Figure 1-figure supplement 2. We have added the following text:

“We observed a small amount of ‘ringing’ of the field response which we interpret as either CA3 spiking in a burst, or recurrent activation of the CA3 neurons (Figure 1-figure supplement 2). The ringing was down to ~5% by the third peak which occurred within 8 ms, supporting our treatment of the optical input as a single brief event, and setting a low bound to any contribution to patterns by recurrence.”

> *P8 F2A: How are the responses normalized?*

In the text we state:

"All the PSPs of an 8-pulse train were normalised to the probe pulse."

We have added this line into the legend.

"Traces were normalised to a reference pulse 0, delivered 300ms before the burst."

> *Explain why, given this normalization, the 15 square stimulation is less effective than the 5 square one.*

We acknowledge this was unclear. In the revised text we explain:

"For the EPSCs, the 15-square trials had a higher reference pulse and higher stimulus overlap (discussed below), hence their normalised peak values were smaller (Figure 2E)."

> *F2D: Where do you show that the biphasic response is a statistically significant deviation?*

Thank you for pointing out this missing analysis. We have added it in Figure 3A.

> *P9 149: E should be E&F.*

Corrected.

> *P9 L150: Explain the "ii" indexing.*

Corrected.

> *P10: It is a bit clumsy to call the measure gamma. For general observation on the equation, see the general remark above.*

Please see discussion on this. We are reusing a published term.

> *P10 L175: How do your results and F3G show divisive inhibition?*

In the current study we're not setting out to show divisive inhibition, as that work has been published (Bhatia et al, eLife, 2019). We've corrected the text accordingly.

"Using responses from the reference pulse, we replicated earlier observations (Bhatia et al. 2019; Wehr and Zador 2003) showing divisive normalisation, and obtained a median gamma of 7.16 (95% CI = 4.76 - 10.2)(Figure 3G)."

Becomes

"By comparing observed vs. expected responses, we replicated earlier observations (Bhatia et al. 2019; Wehr and Zador 2003) showing sublinear summation, and obtained a median gamma of 7.16 (95% CI = 4.76 - 10.2) (Figure 3G)."

> *P16: How does F5 demonstrate a good match between model and physiology?*

We acknowledge we left this out. In F5E we show the model and experiment distributions over different frequencies. Our previous analysis only reported frequency dependence, and now we have added the comparison of response amplitudes. We have inserted the analysis and consolidated the results into Table 1.

> *P18 l281: 15-square patterns (yellow dots) almost always gave an EPSP, while 5-square patterns frequently failed.*

> *Where can I see this? It is mentioned in the caption, but legends are absent.*

In the original source file and in the original confirmation pdf from eLife, the figure legend is present, and has an entry for panel C and D.

“C,D:probability of trigger to generate a peak in the EPSP trace”

In the revised version we have quantified these values and put the comparisons into Table 1:

“Then we compared the probability that each optical stimulus would elicit an EPSP (Figure 6 D). As expected, 15-square patterns (yellow dots) frequently gave an EPSP (77.5±11.7%), while 5-square patterns failed about half the time (51.4±16%). The simulated runs matched this (Table 1).”

> *P19 l307: Overall, we were able to replicate numerous features...*

Please be specific. What exactly did you replicate? How is it statistically demonstrated?

This is a good point, we have updated the text to more systematically work through comparisons and metrics. We have also added some further metrics for features of the responses in Figures 5 and 6. As a way to organize all our comparisons we have added Table 1.

> *P22 l341: The transient responses must be proportional to the overlap. Please quantify this effect more precisely.*

In Fig 7 panels L and O we had previously quantified the amplitude of transient responses with respect to two parameters closely related to overlap: pattern sparseness and probability of connections from CA3 to CA1. In Figure 9Bi we show that there is a complex and frequency-dependent relationship between overlap and mismatch responses. In the revision in figures 8 and 9 we have recast the “pattern sparseness” term as the more intuitive “overlap”. These are related almost linearly with a negative slope (Figure 9-figure supplement 1).

> *P22 l342: What does "in E" mean?*

Should be Figure 7E for the original version. In the revised paper we have removed this panel.

> *l347: I cannot follow. How do these single traces (7C-E) show these effects?*

We acknowledge that the figure and legend did not clearly indicate the timings of the transitions. We have completely redone and reduced figure 7 to simplify the presentation. The timing of transitions between patterns is now indicated using red triangles.

> *What does denser connectivity refer to?*

Denser connectivity refers to a higher value for probability of connection between CA3 and CA1. In the revised version we have changed the figure to refer to stimulus overlap:

“None of the transitions in Figure 8D (dense stimuli, 34% overlap) were significant, but two transitions in Figure 8E were significant (sparse stimuli with 2.5% overlap, p = 1.53e-5 and 6.1e-5).”

> *P26: It is unreasonable to expect a reader to put this puzzle together.*

We acknowledge that this is a large and complex figure. In response to the reviewer's input we have split the figure between Figures 7 and 9, and removed some panels, so as to make it easier to navigate.

> ***Reviewer #3 (Recommendations for the authors):***
>
> *(1) Which parameters are crucial for determining the preferred frequency (i.e., gamma frequency) for mismatch detection? This point should be addressed further.*

This is an interesting suggestion and we have performed additional simulations to address it. It turns out that the frequency tuning is very broad, over almost the entire gamma range from 40 to 200 Hz, and is indeed tuned by simulation parameters. We have placed these findings in Figure 9 in the new version of the paper.

> *(2) The meanings of horizontal and vertical color bars should be explained in the legend of Figure 2A. Do they show the average values over columns and rows? A similar question applies to Figure 3G.*

We have removed the marginal heatmaps from Figures 2 and 3 as they were not contributing to the interpretation.

> *(3) I wonder whether the proposed mismatch detection is tolerant against timing jitters in repeated presynaptic spike patterns. This information allows us to infer the accuracy required for neural code using population spike patterns.*

This is a good suggestion. We have run additional simulations to quantify this. It turns out that jitter has a clear effect on mismatch detection, and affects 5-square (low-overlap) patterns differently from high overlap (15 square) patterns. The latter see a boost in selectivity with 6 ms jitter. This comparison is now in Figure 7E ii and 7 Eiii

https://doi.org/10.7554/eLife.107708.2.sa0